UNIVERSITY OF CALIFORNIA
SANTA CRUZ

BINARY NEUTRON STAR MERGERS

A dissertation submitted in partial satisfaction of the
requirements for the degree of

Doctor of Philosophy

in

ASTRONOMY AND ASTROPHYSICS

by

Ariadna Murguia Berthier

June 2021

The Dissertation of Ariadna Murguia Berthier
is approved:

Enrico Ramirez-Ruiz, Chair

Scott C. Noble

Ryan Foley

Quentin Williams
Interim Vice Provost and Dean of Graduate Studies

Table of Contents

List of Figures

List of Tables

Abstract

Binary neutron star mergers

by

Ariadna Murguia Berthier

This thesis focuses on describing what happens when a binary neutron star merges. It uses numerical simulations to study the different dominant physics before and after the merger. In August 17, 2017, the first binary neutron star merger was observed by LIGO/Virgo, the gravitational wave observatory. Great efforts by astronomers all around the globe allowed for the electromagnetic follow-up of the event. The discovery, named GW170817, showed evidence that binary neutron stars can produce $\gamma-$ray bursts, and also synthesize heavy elements, such as gold and platinum.

This thesis studies the intriguing question of how binary neutron stars have been able to assemble and merge within the timespan the Universe has existed. One of the preferred channels is called common envelope evolution. This happens when, in a binary of massive stars, the more massive star (the primary) evolves, expands and engulfs its companion. Drag forces from the envelope slow down the companion and tighten the orbit. The energy from the orbit will be transferred to the envelope and will potentially have enough energy to unbind the envelope. The result is the very rapid creation of a tighter binary. This thesis studies the accretion flows around the companion, given that the envelope has a gradient. Material will be focused on the companion (the secondary), but due to the density gradient, there will be an angular

momentum barrier that inhibits accretion onto the secondary. We study how different microphysical parameters of the envelope affect the angular momentum redistribution.

It is widely believed that the merger of GW170817 was a hyper-massive neutron star that after a certain delay time collapsed into a black hole surrounded by an accretion disk. Material in the disk will lose angular momentum due to magnetic stresses, eventually falling into the black hole and driving a relativistic, beamed jet. The jet will interact with winds launched during the hyper-massive neutron star phase. This thesis studies jet-wind interactions, since they lead to non-thermal emission. We used numerical simulations in order to constrain certain parameters of the binary itself, such as the delay time between the merger and the collapse to a black hole.

Several other outflows are expected to occur after the merger, including an outflow driven from magnetic stresses in the accretion disk. The outflow will cool, expand and create heavy elements via the $r-$process. This elements will then radioactively decay and be observed. In the inner regions of the disk, the high temperatures and densities will ignite the creation of neutrinos and anti-neutrinos via weak reactions. In the outer region of the disk, free nucleons will recombine into $\alpha-$particles, which will release nuclear binding energy. Both the neutrinos and the recombination energy will greatly affect the outflow, especially the electron fraction. The electron fraction is key in determining the final abundance of elements. This thesis studies the impact that neutrinos and a finite-temperature equation of state have on the outflow.

Acknowledgments

I want to thank my amazing husband, the love of my life, for all the support, great talks, movie nights, and companionship. You have made me really happy.

When I was very small, it was very clear that I wanted to be a scientist. My father, being the amazing person he was, saw that in me and fostered my passion for science. He bought me books and took me to conferences and NASA, even though he was not a scientist. My mother, also being the amazing person she was, always believed in me and was my being my biggest fan, supporter and role model. I know they are looking at me proudly from heaven. I want to thank them, and also my little bro and my sis, for being there for me in good and tough times, laughing, watching Friends, getting bubble waffles, and all the sushi. My family taught me so many things that I'm grateful for: strength, perseverance, honesty, wisdom, just having fun.

I'm also incredibly thankful to my family away from home, the Ramirez-Truses. Eva, my super cool prank accomplice. Carlo, the best fútbol player in the US. Kris, a great friend. And finally, the greatest, most thoughtful, supportive advisor in the world, Enrico. I cannot write enough good things about you. You were there for me in my hardest time, you have greatly encouraged me, supported me. I'm incredibly indebted to you, I'm where I am in part because of you. We are a great team. All the lessons you have taught me over the years, all the mentoring will be always with me. Thank you deeply for everything, and I promise to pay it forward.

To my committee members, I am indebted for all the support, cheerleading, advice and encouragement. Scott Noble, my amazing co-advisor, who has nurtured

my passion for GR, my passion for coding. I thank you for all your enthusiasm and for receiving me with open arms into the TCAN collaboration. Agnieszka Janiuk, my gym/hip hop dancing/salsa dancing partner. You have been an incredible mentor who introduced me to GRMHD and have been there for me for a long time. I deeply thank you for your mentorship and dancing. Ryan Foley, my observational astronomy teacher. You have supported me during my time at UCSC and welcomed me to your group. I thank you for everything.

I thank all my friends at UCSC for all the fun adventures, the support and all the help. I really want to thank all the people at Calvin Place, my roomies. You were incredible and I had a blast: Tiff, Eric, Alexa, Mickey, Elizabeth, and appointment cat. I also want to thank my awesome cohort for all the study groups and conversations: Asher, Diana, Jamie. All the people at Alta, you are really cool and I'll always remember the fun halloween carving parties! ¡Muchas gracias a mis amigos latinos, en particular Aldo Beto, Gaby, Bruno, César, Nico y Ricky! ¡Muchas gracias por todo el apoyo, las risas, los consejos, las idas a 99 bottles! Son lo máximo, y los voy a extrañar mucho. I also want to thank everyone in Enrico's group and collaborators (in no particular order): Aldo, Gaby, Morgan, Phil, Anna, Alejandro, Jamie, Brenna, Rosa, Sophie, Ricardo, Tenley, Sierra, Naela, Lena, Jess, Alejandra, Vale, Nick, Andrea, Sam, Jill, Fabio, Jane, Katie, Andrew, Stephan, William, Luciano, Ilya, Luke, Josiah, Nicole, Melinda, Camille, Rewa. Thank you Deana, Linsday, Jenna and David for all the support at UCSC. I thank the TCAN collaboration, in particular the PI, Manuela Campanelli, an amazing mentor to me, always supporting other women in science, and my super cool co-advisor Scott

Noble. Thank you also for my loyal writing buddy: Luna.

I want to thank my amazing collaborators, and thank you for the permission to reproduce our work in this thesis. Including: Morgan MacLeod, Enrico Ramirez-Ruiz, Andrea Antoni, and Phil Macias, Chapter 2, published as (Murguia-Berthier et al. 2017a); Enrico Ramirez-Ruiz, Gaby Montes, Fabio De Colle, Luciano Rezzolla, Stephan Rosswog, Kentaro Takami, Albino Perego, and William H. Lee, Chapter 3, published as (Murguia-Berthier et al. 2017b); Enrico Ramirez-Ruiz, Charlie Kilpatrick, Ryan Foley, and the entire 1M2H collaboration represented by the PI: Ryan Foley, Chapter 4 published as (Murguia-Berthier et al. 2017c), Enrico Ramirez-Ruiz, Fabio De Colle, Agnieszka Janiuk, Stephan Rosswog and William Lee, Chapter 5 as published in (Murguia-Berthier et al. 2021), Manuela Campanelli on behalf of the co-authors and TCAN collaboration, Chapter 6, as submitted to ApJ, Aldo Batta, Agnieszka Janiuk, Enrico Ramirez-Ruiz, Ilya Mandel, Scott Noble, Rosa Wallace Everson, Chapter 7 as published in (Murguia-Berthier et al. 2020). These works are reproduced with the permission of IOP Publishing. During my PhD, I have been supported by a Conacyt-UC-Mexus doctoral scholarship, the Heising-Simons Foundation, the Danish National Research Foundation (DNRF132), NSF (AST-1911206 and AST-1852393) and the NASA TCAN award TCAN-80NSSC18K1488. Computational resources were provided by the NCSA's Blue Waters sustained-petascale computing NSF projects OAC-1811228 and OAC-1516125, by the TACC's Frontera NSF projects PHY20010 and AST20021, and the lux supercomputer at UC Santa Cruz, funded by NSF MRI grant AST 1828315. Portions of the work were written at the DARK Cosmology Centre at Copenhagen,

Instituto de Física at Universidad Nacional Autónoma de México, campus Morelos with Gloria Koenigsberger.

For my parents

Chapter 1

Introduction

In August 17, 2017, the LIGO/Virgo collaboration detected the first gravitational wave associated with the violent merger of binary neutron stars (Abbott et al. 2017c) and called it GW170817. This groundbreaking discovery, which was appropriately named the 2017 Science Breakthrough of the year, allowed us to gather more information about what happens to matter in the most extreme densities and temperatures known. This discovery was accompanied by electromagnetic light from all over the spectrum, which was discovered by efforts led by astronomers at UCSC, including myself (Abbott et al. 2017d; Coulter et al. 2017a; Murguia-Berthier et al. 2017b; Shappee et al. 2017; Drout et al. 2017; Kilpatrick et al. 2017). GW170817 opened a new window into the cosmos and the study of transients.

Ever since gravitational waves-which are distortions of space and time- were predicted by Einstein's theory of general relativity, scientists have been trying to detect them. They were unsuccessful until 2015 when LIGO, the gravitational wave observa-

tory, finally observed the first gravitational wave, which came from a pair of black holes colliding with each other (Abbott et al. 2016a,b, 2017a,b). Two merging black holes are not expected to leave a visible trace in the sky, but two merging neutron stars are likely to produce light all over the electromagnetic spectrum.

This thesis focuses on the different mechanisms in binary neutron star mergers that govern the emissions, how the binary is formed, and how to black holes form where there is no observed transient.

1.1 Formation of binary neutron stars

As binary neutron stars get closer to each other, they radiate energy in the form of gravitational waves causing them to get closer together until they merge. One limiting factor in the merger is that both neutron stars need to be extremely close for gravitational waves to efficiently dissipate energy.

Given the cascade of factors involved in binary neutron star formation and mergers, it has been an ongoing challenge for scientists to understand how they have had time to the assemble and merge within the time of existence of the Universe. To form a binary of neutron stars, you first need a couple of massive stars to die. Massive stars are kept from collapsing under their own gravitational force thanks to the constant fusion occurring in their cores. However, when the fuel for fusion runs out, the gravitational force wins and the star collapses—that is, until neutron degeneracy pressure acts and stops the collapse, forming a neutron star. To end up with a neutron star binary, two massive stars need to collapse into neutron stars in close proximity to one another. The

challenge is getting them close together. One can naively assume that two massive stars could begin at the necessary separation. The problem with that assumption is that as the massive star evolves and expands, it would engulf its companion, leaving just one star rather than a binary. A creative way to get around this challenge is through common envelope evolution. During common envelope evolution, the binary starts at a larger separation, and then the orbit tightens to a very short separation in a very short timescale.

A common envelope phase occurs when, in a binary, the more massive star expands and engulfs its companion. Drag forces from the gaseous envelope slow down the companion and tighten the orbit. The loss of orbital energy is transferred onto the envelope. If the energy transfer is larger than the binding energy of the envelope, the envelope will be ejected, and the result will be a tighter binary (Webbink 1984; Iben & Livio 1993; Nelemans et al. 2000; Dewi & Tauris 2000; Taam & Sandquist 2000; Taam & Ricker 2010; Ivanova et al. 2013).

Understanding the common envelope phase is in itself a challenge due to all the physical processes involved, as well as the enormous difference in timescales and spatial scales needed to resolve the problem. Chapter 2 uses a simplified approach where we study the morphology of the flows around the embedded companion. This approach has proven advantageous in determining the drag forces acting on the companion (MacLeod & Ramirez-Ruiz 2015a; MacLeod et al. 2017a). In this chapter, we show that common envelope evolution is a viable channel for binary neutron star formation by addressing some known issues. One issue, for example, is that theory predicts that as the embedded

companion is orbiting the more massive star, the density gradient in the envelope might form an accretion disk around the companion. If matter from the disk is accreted, energy will be dissipated and added to the envelope. This energy is much larger than the binding energy of the envelope, and thus the envelope could be ejected too early, not allowing for the tightening of the orbit. However, our results show that the creation of the disk is highly dependent on the microphysical parameters of the gas (Murguia-Berthier et al. 2017a). Highly compressible environments foster the creation of disks, whereas no disk will be formed in less compressible environments. We apply this result to explain how black holes can form binaries capable of merging within the lifespan of the Universe, such as the ones that LIGO detected. Our conclusion is that the massive stars that form binary black holes will not form accretion disks, and therefore accretion will not occur, solving the problem.

1.2 Non-thermal emission from binary neutron star mergers: relativistic jets

After the binary neutron star merges, the result will be a hyper-massive neutron star that is hot and rapidly rotating. Depending on the total mass, the merger can promptly collapse to a black hole, collapse to a black hole after a delay time, or live stably as a massive neutron star. GW170817 is thought to be the result of a delayed collapse to a black hole (Murguia-Berthier et al. 2017c; Granot et al. 2017; Gottlieb et al. 2018b; Nakar et al. 2018; Metzger et al. 2018; Xie et al. 2018; Gill et al. 2019b; van Putten et al. 2019; Lazzati et al. 2020; Hamidani et al. 2020).

In the delayed collapse scenario, the binary neutron star merger results in a black hole surrounded by an accretion disk (Baiotti et al. 2008). Magnetic stresses transport angular momentum outward in the disk, driving material from the disk into the black hole. The energy dissipated results in a relativistic, beamed jet (Rezzolla et al. 2011; McKinney et al. 2012, 2014; Sądowski et al. 2015; Ruiz et al. 2016; van Eerten et al. 2018; Qian et al. 2018; Kathirgamaraju et al. 2019; Ruiz et al. 2019) which will emit in $\gamma-$rays. This is called a short $\gamma-$ray burst (sGRB).

During the hyper-massive neutron star phase, neutrino-driven winds and magnetic fields transport angular momentum, driving an outflow. The relativistic jet will interact with the outflows, which will in turn shape the jet. In Chapter 3, we study how the jet propagates through several winds. We conclude that the winds can potentially be dense enough, or the power of the jet low enough so that the jet is choked by the wind (Murguia-Berthier et al. 2014, 2017b). We also study the parameter space where this is possible and compare it to observations of sGRB.

As the jet propagates through the medium, it will decelerate, and electrons will be emitted via synchrotron emission. The emission, known as an afterglow, will be all over the electromagnetic spectrum. In Chapter 4 we examine the non-thermal emission from the sGRB that resulted from GW170817. The emission from GW170817 was extremely peculiar, unlike any other sGRB, as the luminosity in the high-energy regime was uncharacteristically small. In this chapter, we study two different scenarios in which it is possible to reconcile the low energy of this event. One possibility is that the observations of the sGRB were not seen on-axis, like usual, but rather off-axis. The

other possibility we argued was that the uncharacteristic luminosity could be due to a mildly relativistic blastwave expanding. With new observations, it is now believed that GW170817 resulted in an sGRB seen off-axis (Murguia-Berthier et al. 2017c; Lazzati et al. 2017; Duffell et al. 2018; Bromberg et al. 2018; Granot et al. 2018; Lamb & Kobayashi 2018; Xie et al. 2018; Kathirgamaraju et al. 2018; van Eerten et al. 2018; Gill et al. 2019a; Lamb et al. 2019; Lazzati & Perna 2019; Beniamini et al. 2020; Lazzati et al. 2020; Ryan et al. 2020; Nakar & Piran 2020).

In Chapter 5 we explore how the jet propagates through different types of winds. We perform simulations varying both the duration of the wind and the jet. The duration of the wind is related to the time between the merger and the collapse to a black hole. The duration of the jet is related to the time the central engine remains active. We then compare the resulting shape of the jet with the expected shape of GW170817 and use that information in order to constrain the delay time (Murguia-Berthier et al. 2021).

1.3 Thermal emission from binary neutron star mergers: kilonovae and the creation of heavy elements

There are several outflows launched from the binary neutron star merger. Soon after the merger, long tidal tails are thrown out through the outer Lagrange points. There are also neutrino-driven winds generated by the rapidly-spinning merged system. Additionally, a wind driven by magnetic stresses in the accretion disk is expected to dominate the total mass inventory and has been invoked as the dominant mass ejection

mass mechanism in GW170817 (Kasen et al. 2017). All of these outflows expel metallic material that will expand, cool, and then radioactively decay into what is known as a kilonova. The observations of the kilonova in GW170817 provided the first solid evidence that much of the Universe's gold, platinum and other heavy elements are created in such environments through what is known as the $r-$process.

However, there is an ongoing debate about whether the $r-$process can be responsible for ejecting the bulk of the enriched material and how the final composition depends on neutrino interactions in the wind driven by magnetic stresses. Simulations of the accretion disks around binary neutron star mergers have ejecta masses that vary by nearly an order of magnitude (e.g., compare Siegel & Metzger 2018 to Miller et al. 2019a). The final composition of the ejecta is also under debate, as the range of heavy element abundances in simulations also varies. There is particular debate on whether third-peak $r-$process elements, such as lanthanides, are formed. The key element in determining the final abundance of heavy elements is the electron fraction of the ejecta, which in turn greatly depends on neutrinos and their impact.

Therefore, to realistically model the outflow of the merger, we require multi-physics, efficient computing codes. These codes need to include general relativity, magneto-hydrodynamics (GRMHD), neutrino transport, and detailed models for matter at nuclear densities. I have worked on improving the state-of-the-art code called HARM3D. Chapter 6 explores how we augmented HARM3D with a neutrino leakage scheme (an approximation of neutrino transport) and a tabulated equation of state (EOS) that considers the release of nuclear binding energy during free nucleon recom-

bination to $\alpha-$particles. HARM3D is a GRMHD code that uses arbitrary grids, better conserving angular momentum. The code has been well tested, used in many astrophysical scenarios, and has copious post-processing tools (Gammie et al. 2003a; Noble et al. 2006a, 2009). The chapter demonstrates tests performed to validate the new code. We also apply the new code to a magnetized torus that resembles the accretion disk resulting from a binary neutron star.

1.4 Formation a black holes: a case study on disappearing stars

We have tentative evidence of massive stars that disappear without a bright transient (Gerke et al. 2015; Adams et al. 2017; Allan et al. 2020). One proposed idea to explain this phenomenon is through a direct collapse to a black hole.

As the massive star runs out of fuel, the iron core collapses into a black hole. Material from the outer layers thus loses the pressure support needed to counteract gravity and falls into the black hole. If the infalling material happens to have no angular momentum, it will be directly accreted into the black hole. Since the black hole has no surface, all the material is accreted without feedback. Therefore, it is possible for a star to collapse without a bright transient. If, on the other hand, the material has high angular momentum, a disk will form around the black hole. Magnetic stresses on the accretion disk will transport angular momentum outwards, and as material from the disk falls into the black hole, energy will be dissipated. This feedback energy is much larger than the binding energy of the entire massive star's envelope. Therefore,

the envelope will be ejected, and there will be a bright transient.

Chapter 7 explores what happens in a low angular momentum regime. We use general relativistic simulations to identify the point at which accretion feedback becomes efficient. We then use the results in order to constrain the angular momentum of two disappearing stars found in the literature. We also use observational data of O-stars in order to conclude that the fraction of disappearing stars should be around 7%, which is consistent with the literature (Murguia-Berthier et al. 2020).

1.5 Outline of this thesis

This thesis focuses on all aspects of binary neutron star mergers. We begin with Chapter 2, which focuses on the assembly of binary neutron stars that can merge within the time the Universe has existed. It explores the formation of the binary through common envelope evolution.

Next, we focus on what happens once the binary merges, resulting in a black hole surrounded by an accretion disk. A relativistic jet will be launched and interact with different winds generated in the merger. Chapters 3 through 5 explore how the jet interacts with the winds. We make use of simulations in order to constrain several binary neutron star parameters, including the delay time between the merger itself and the collapse to a black hole. We then constrain some binary properties of GW170817. These chapters focus on the non-thermal emission from the merger.

Chapter 6 focuses on the thermal component of the merger, specifically how outflows form due to magnetic stresses and how neutrinos and the release of nuclear

binding energy through recombination impact the outflow. This chapter shows the addition of an approximate neutrino transport and a tabulated equation of state.

Finally, Chapter 7 studies a particular case of black hole formation: massive stars that disappear without leaving a trace. We use numerical simulations to constrain the angular momentum of massive stars that disappear without a bright transient.

Chapter 2

Assembly of binary neutron stars: understanding common envelope

2.1 Chapter Abstract

During a common envelope episode in a binary system, the engulfed companion spirals to tighter orbital separations under the influence of drag from the surrounding envelope material. As this object sweeps through material with a steep radial gradient of density, net angular momentum is introduced into the flow, potentially leading to the formation of an accretion disk. The presence of a disk would have dramatic consequences for the outcome of the interaction because accretion might be accompanied by strong, polar outflows with enough energy to unbind the entire envelope. Without a detailed understanding of the necessary conditions for disk formation during common envelope, therefore, it is difficult to accurately predict the population of merging compact binaries.

This paper examines the conditions for disk formation around objects embedded within common envelopes using the 'wind tunnel' formalism developed by MacLeod et al. (2017a). We find that the formation of disks is highly dependent on the compressibility of the envelope material. Disks form only in the most compressible of stellar envelope gas, found in envelopes' outer layers in zones of partial ionization. These zones are largest in low-mass stellar envelopes, but comprise small portions of the envelope mass and radius in all cases. We conclude that disk formation and associated accretion feedback in common envelope is rare, and if it occurs, transitory. The implication for LIGO black hole binary assembly is that by avoiding strong accretion feedback, common envelope interactions should still result in the substantial orbital tightening needed to produce merging binaries.

2.2 Introduction

A common envelope (CE) phase develops in a binary system when one of the stars evolves off the main sequence and engulfs its companion (Paczynski 1976). Inside the CE an embedded object's orbit decays due to gravitational interaction with the surrounding gas. As orbital energy and momentum are exchanged with the CE gas, the envelope may gain sufficient energy and angular momentum to become unbound (Webbink 1984; Iben & Livio 1993; Nelemans et al. 2000; Dewi & Tauris 2000; Taam & Sandquist 2000; Taam & Ricker 2010; Ivanova et al. 2013).

Depending on the efficacy of this envelope unbinding, the binary may either survive with a tightened orbit, or merge into a single object. The pathways through

which mass, angular momentum, and energy can flow through and around the CE thus play a crucial role in establishing the outcomes of CE interactions and, more broadly, they determine the imprint of CE on binary evolution (e.g. Iben & Livio 1993; Ivanova et al. 2013; Postnov & Yungelson 2014; De Marco & Izzard 2017). These considerations are of particular importance when considering the assembly of compact objects into tight orbits from which gravitational radiation can drive them to merger in less than a Hubble time (e.g. Belczynski et al. 2002, 2007; Kalogera et al. 2007; Belczynski et al. 2010, 2016).

While the decay of the orbit is a known source of energy to the CE gas, there has also been discussion of whether accretion onto the embedded object could "feedback" and assist in unbinding the envelope gas (see section 3.5 of Iben & Livio 1993, for a discussion of this and other potential energy sources and sinks). Even the accretion of a small fraction of the CE mass onto a compact object could be sufficient to unbind the CE gas (e.g. Soker 2004, 2015). For example, for an envelope of mass $M_{\rm env}$ with escape velocity $v_{\rm esc}$, an embedded black hole need only accrete a fraction $\Delta M/M_{\rm env} \gtrsim (v_{\rm esc}/c)^2$ to release sufficient energy to impinge upon or unbind the CE. As a consequence, if accretion and associated feedback are major sources of energy in the CE event, the degree of orbital tightening required to eject a given CE (and terminate the interaction) would be drastically reduced. A reduction in the orbital tightening experienced during the CE phase would, in turn, impact the population of compact binaries with merger times less than a Hubble time. If feedback from accretion were too efficient, we could imagine that CE-like interactions might produce no GW merger

sources – instead leaving behind only binaries too wide to merge today.

Answering these important questions has not been straightforward, in large part because they depend on the details of the complex flow around objects embedded in CE. Gradients in the CE structure introduce angular momentum into the flow about the embedded object, potentially leading to the formation of a rotationally-supported disk (Armitage & Livio 2000; Blondin 2013). Disk structures, ubiquitous in astrophysical systems, create a mechanism through which these accretion-and-feedback flows persist: mass flows in the plane of the disk while energy is carried away vertically. In this case, inflow of mass, transported from large scales to an embedded companion, could be accompanied by prodigious mass loss driven by the outflows released by the accreted gas (e.g., Balbus & Hawley 1991; Blandford & Begelman 1999). It's worth noting that the total outflow power need not be limited to the Eddington luminosity (e.g. Paczyński & Wiita 1980) as has, for example, been considered by Voss & Tauris (2003); Kruckow et al. (2016). If these outflows were launched in the polar directions, they would impinge upon, and help unbind, material away from the binary orbital plane (Armitage & Livio 2000; Voss & Tauris 2003; Papish et al. 2013; Soker 2015; Moreno Méndez et al. 2017; Shiber et al. 2017). Whether or not a disk forms may, therefore, have dramatic consequences on the accretion rate onto an embedded object and, also, on the accompanying feedback that could influence the CE gas at larger scales. As will become clear, disk formation is particularly dependent on the thermal properties of the envelope, in particular, the response of the gas to compression.

To study the conditions under which disks can form in CE flows, we per-

form numerical simulations using the wind tunnel formalism developed by MacLeod & Ramirez-Ruiz (2015a) and MacLeod et al. (2017a). We explore local gas compressibility as a key parameter in shaping whether or not a disk forms around an embedded object. Section 2.2.1 introduces the numerical motivation and the formalism used. Section 2.3 describes the results from our calculations. We will argue that disks form only in regions of high compressibility with an adiabatic index $\gamma < 4/3$. In Section 2.4, we extend our findings of the conditions under which disks are observed to form in order to study where these conditions are typically found in stellar envelopes. We show that appreciable regions of sufficiently high compressibility occur in zones of partial ionization, and are likely only present in the envelopes of low mass giants. We argue that this implies that accretion feedback plays little role in shaping the outcomes of CE episodes involving binary black holes. And that, as a result, CE interactions with black holes should lead to substantial orbital tightening.

2.2.1 Motivation and Numerical Formalism

Background We will consider flow around a secondary object of mass M_2 and radius R_2 that is engulfed by its evolving companion (denoted here as the primary star) with total mass M_1 and radius $R_1 \gg R_2$. The pair has a mass ratio, $q = M_2/M_1$. The embedded object, separated by a distance $a \lesssim R_1$, will move within the CE with a characteristic orbital velocity $v_{\rm k}^2(a) = G[M_2 + M_1(a)]/a$, where $M_1(a)$ is the enclosed mass inside the orbit of the secondary. The orbital motion of the embedded object is likely to be desynchronized from the envelope of M_1 and the relative velocity can be written as $v_\infty = f_{\rm k} v_{\rm k}$, where $f_{\rm k}$ is the fraction of Keplerian velocity representing the

relative motion between the gas in M_1's envelope and M_2.

Studies of CE often make use of Hoyle-Lyttleton accretion (HLA), a simple framework for understanding flow around an embedded secondary (e.g. Iben & Livio 1993; MacLeod & Ramirez-Ruiz 2015a,b; MacLeod et al. 2017a). In this case, the object moves supersonically through the envelope and gravitationally focuses the surrounding gas. Accretion is envisioned to take place if the impact parameter of the incoming gas is less than the accretion radius,

$$R_{\rm a} = \frac{2GM_2}{v_\infty^2}, \tag{2.1}$$

where v_∞ is assumed to be supersonic (Hoyle & Lyttleton 1939; Bondi & Hoyle 1944; Bondi 1952). The corresponding mass accretion rate onto the embedded companion can then be written as

$$\dot{M}_{\rm HLA} = \pi R_{\rm a}^2 \rho_\infty v_\infty, \tag{2.2}$$

where ρ_∞ is the density of the incoming gas (for a recent comprehensive review the reader is referred to Edgar 2004). The deflection of material will result in a reconfiguration of the flow, which in turn generates a net dynamical friction, drag on the secondary (Ostriker 1999).

HLA was first investigated numerically by Hunt (1971) in order to determine whether $\dot{M}_{\rm HLA}$ can provide an accurate estimate of the rate of mass accretion, concluding that it was indeed reasonable ($\dot{M} \approx 0.88\dot{M}_{\rm HLA}$). This pioneering work laid the ground for several hydrodynamical studies for HLA in two (Shima et al. 1985; Blondin & Pope

2009; Blondin 2013) and three (Ruffert 1994a; Ruffert & Arnett 1994; Ruffert 1994b, 1995, 1996; Blondin & Raymer 2012) dimensions. Of particular relevance to our work are the studies of Ruffert (1994a); Ruffert & Arnett (1994); Ruffert (1994b, 1995, 1996), as they explored in great detail the effects of varying the properties of the background gas, in particular, the role of the compressibility of the flow. If the flow is more compressible, the loss of pressure support will result in a standing shock that resides closer to the accretor. The higher post-shock densities in addition to the steep pressure gradients, were shown to produce higher mass accretion rates. Simulations in two dimensions showed that for highly compressible gas, the flow structure becomes significantly less stable, resulting in large variations in the mass accretion rate (Blondin & Pope 2009; Blondin 2013).

The HLA formalism has been widely used to describe the flow around objects embedded within a common-envelope, but it fails to provide an accurate description of the flow. The formalism assumes a homogeneous background, which does not reflect the steep density profiles of evolving stars. Studies of HLA with vertical density and velocity gradients have been tackled by several groups (Livio et al. 1986a; Soker et al. 1986; Livio et al. 1986b; Fryxell et al. 1987; Fryxell & Taam 1988; Taam & Fryxell 1989; Ruffert 1997, 1999; Armitage & Livio 2000; MacLeod & Ramirez-Ruiz 2015a,b), although in most cases the assumed density gradients are shallow and are thus not representative of those found in stellar envelopes (MacLeod & Ramirez-Ruiz 2015a). Symmetry breaking generated by the vertical gradient gives the flow net angular momentum relative to the accreting object. Even small gradients thus can have large-scale impacts on the flow,

leading to rotational support for material, instead of radial infall as envisioned in HLA.

The radial inflow approximation breaks down when the gas reaches a radius $R_{\rm circ} = {l_z}^2/GM_2$, where l_z is the specific angular momentum (see, e.g., section 4.2 of MacLeod & Ramirez-Ruiz 2015a). Armitage & Livio (2000) perform two-dimensional simulations with an exponentially decreasing density gradient for radiation pressure dominated ($\gamma = 4/3$) flows. They use a cylindrical geometry and assume a reflective inner boundary condition. Under these conditions, they found a stable centrifugally supported structure forming in their simulations. However, in recent three-dimensional calculations using similar density gradients, MacLeod & Ramirez-Ruiz (2015a) and MacLeod et al. (2017a) failed to produce rotationally-supported structures for radiation pressure dominated flows and only saw disks when considering a softer equation of state.

Generally, envelope gas may have a different response to compression under varying density and temperature conditions as determined by its equation of state. The thermodynamic description of the flow can be characterized by adiabatic exponents,

$$\gamma_1 = \left(\frac{d\ln P}{d\ln \rho}\right)_{\rm ad}, \tag{2.3}$$

and,

$$\gamma_3 = 1 + \left(\frac{d\ln T}{d\ln \rho}\right)_{\rm ad}, \tag{2.4}$$

where the subscript signals partial derivatives along a particular adiabat. γ_1 is relevant for calculating the sound speed of the gas, $c_{\rm s}^2 = \gamma_1 P/\rho$ while γ_3 is related to the equation

of state,

$$P = (\gamma_3 - 1)\rho e, \tag{2.5}$$

where e is the internal energy. In general γ_1 will be greater than γ_3 when radiation plays a prominent role because in that case pressure increases faster than temperature in response to compression.

Material in a disk dissipates its motion perpendicular to the orbital plane, forming a differentially rotating structure. A net flow of material inward results when a viscosity-like stress transports angular momentum content outwards in the shear flow. A dynamo process of some kind is commonly believed to work and simple physical considerations suggest that fields generated in this way would have a length-scale of the order of the disk thickness and could drive a strong hydromagnetic wind (Balbus & Hawley 1991). As discussed in the introduction, if the embedded object is a compact object, this outflow could have enough kinetic energy to substantially alter the structure of the envelope.

In the remainder of this work, we discuss how the properties of the stellar envelope have a decisive effect on whether or not a rotationally-supported structure can form around an object embedded within a CE.

2.2.2 Model and Numerical Setup

We perform idealized simulations of the flow around an embedded object using the CE Wind Tunnel (CEWT) formalism presented by MacLeod et al. (2017a). The inviscid hydrodynamic equations are solved using FLASH (Fryxell et al. 2000), an

Eulerian, adaptive mesh refinement code. This setup models the embedded secondary companion as a sink point particle of radius $R_{\rm s}$ at the origin. A wind, representing the gaseous envelope with a vertical profile of density and pressure, is fed in the $+x$-direction from the $-x$ boundary. This profile is in hydrostatic equilibrium with a vertical ($\hat{y}$), external y^{-2} gravitational acceleration representing the gravity of the enclosed mass of the primary star. The code and methodology are described in detail in MacLeod et al. (2017a), but we include a few key points here for context.

2.2.3 Local Description of the CE

The vertical profile of density and pressure within the envelope are locally approximated with a polytropic profile of a massless envelope (which assumes that the enclosed mass is small compared to the total mass of the primary across the region simulated $\sim R_{\rm a}$). In this case, the pressure and density profiles of the surrounding envelope are described by

$$\frac{d\rho}{dr} = -g\frac{\rho^2}{\Gamma_{\rm s} P}, \tag{2.6}$$

and,

$$\frac{dP}{dr} = -g\rho, \tag{2.7}$$

where $g = GM_1/r^2$. The structural polytropic index of the stellar profile is $\Gamma_{\rm s} = \left(\frac{d\ln P}{d\ln \rho}\right)_{\rm env}$.

The gas envelope might have a different response to compression (as characterized by γ_1 and γ_3) than the one implied by the polytropic index of the stellar

profile. This is because rearrangements induced by the embedded object will happen on a timescale much shorter than the thermal timescale of the evolving primary. For example, a fully convective envelope might have $\Gamma_s \approx \gamma_1$ whereas a radiative envelope might have $\Gamma_s < \gamma_1$. In the case of an ideal gas, as considered in our FLASH calculations, we have the simplification $\gamma = \gamma_1 = \gamma_3$. Regions where gas pressure dominates can be described by a $\gamma = 5/3$ while regions where radiation pressure dominates are well characterized by a $\gamma = 4/3$.

Locally, within this polytropic stellar envelope, the flow is described by dimensionless parameters such as the Mach number,

$$\mathcal{M} = v_\infty / c_{s,\infty}, \tag{2.8}$$

and the density gradient,

$$\epsilon_\rho = R_a / H_\rho. \tag{2.9}$$

Here $H_\rho = -\rho dr/d\rho$, and ϵ_ρ represents the number of scale heights across the accretion radius within the primary star's envelope, with $\epsilon_\rho \to 0$ describing an homogeneous density structure and $\epsilon_\rho \to \infty$ describing a very steep density gradient. MacLeod et al. (2017a) show that the expression

$$\mathcal{M}^2 = \epsilon_\rho \frac{(1+q)^2}{2q} f_k^4 \left(\frac{\Gamma_s}{\gamma_1} \right), \tag{2.10}$$

relates these flow parameters and describes pairings of $\mathcal{M}$ and ϵ_ρ for a given binary mass ratio and envelope structure.

2.2.4 Wind Tunnel Domain, Conditions, and Diagnostics

The units of the simulations are such that $R_{\rm a} = v_\infty = \rho_\infty = 1$, where ρ_∞ is the density of the envelope at a distance $r = a$ from the primary's center. In this case, the characteristic time is $t = R_{\rm a}/v_\infty = 1$ and the mass of the embedded object is $M_2 = (2G)^{-1}$. We employ $8 \times 5 \times 5$ initial blocks of 8^3 cells in each direction, in a box of size $(-5, 3)R_{\rm a} \times (-2.5, 2.5)R_{\rm a} \times (-2.5, 2.5)R_{\rm a}$. The maximum refinement level is set to 8, and the minimum is set to 2. Therefore, the maximum cell size is $R_{\rm a}/16$ and the minimum is $R_{\rm a}/1024$. The secondary is fixed at the origin and is surrounded by a sink boundary of radius $R_{\rm s}$.

As in the simulations of (MacLeod et al. 2017a), the $-x$ boundary feeds a wind across the box in the $+x$ direction. The corresponding gradient of pressure and density is constructed in the y direction and is uniform in the z direction. The conditions of the flow are parametrized by a density gradient, ϵ_ρ, an upstream Mach number, $\mathcal{M}$, and the pressure and density at $y = 0$ given q, $f_{\rm k}$, $\Gamma_{\rm s}$ and γ. Once the values at $y = 0$ are determined, the vertical structure of the flow ($\pm y$) is constructed using the equations of hydrostatic equilibrium. The structure of the flow is thus in hydrostatic equilibrium with M_1's gravitational force, which acts in the $-y$ direction.

To study the flow structure we employ 50^3 passive particles as gas Lagrangian tracers, randomly distributed within a rectangle of dimensions $(-3, -1) \times (-1, 3) \times (-1, 1)$ and evolved using a Runge Kutta scheme using the Particle module in FLASH (Fryxell et al. 2000). This technique allows us to study the capture and residence of fluid into rotational structures near the embedded object. This approach is valuable be-

cause the flow is highly time-variable, and, in these circumstances, single time snapshot streamlines can be misleading.

2.2.5 Simulation Parameters

The key parameter that we vary across our simulations is the gas adiabatic index, γ. In so doing, we represent portions of the CE material with different compressibility, and, as we will show, different susceptibility to the formation of dense, rotationally-supported disk structures.

The simulations adopt a sink boundary of $R_{\rm s} = 0.02R_{\rm a}$, a central density gradient of $\epsilon_\rho = 2$, a velocity fraction $f_{\rm k} = 1$, and a mass ratio of $q = 0.1$. These parameters may be compared to stellar envelope structures shown in MacLeod & Ramirez-Ruiz (2015a) and MacLeod et al. (2017a). We will discuss the properties of typical stellar envelopes in Section 2.4, but for context, these conditions could represent those found in a $M_1 = 1M_\odot$ giant branch star with $R_1 = 140R_\odot$ engulfing a $M_2 = 0.1M_\odot$ star at a separation of $a = 0.9R_1$, or alternatively a $M_1 = 80M_\odot$ red giant with $R_1 = 740R_\odot$ engulfing a $M_2 = 8M_\odot$ star at a separation of $a = 0.85R_1$.

We vary the adiabatic index across 4 simulations using (a) $\gamma = \Gamma_{\rm s} = 5/3$, (b) $\gamma = \Gamma_{\rm s} = 4/3$, (c) $\gamma = 1.2$ with $\Gamma_{\rm s} = 4/3$, and (d) $\gamma = 1.1$ with $\Gamma_{\rm s} = 4/3$. We adopt $\Gamma_{\rm s} \geq 4/3$ in order to have a polytropic index that is stable to perturbations in pressure (Bonnor 1958).

The circularization radius depends on the density profile, and can be integrated numerically. We make use of $R_{\rm circ} = l_{z,\infty}^2/GM_2$, where $l_{z,\infty}$ is the initial specific angular

momentum

$$l_{z,\infty} = \dot{L}_z(< R_{\rm a})/\dot{M}(< R_{\rm a}). \tag{2.11}$$

Here $\dot{L}_z(< R_{\rm a})$ is the accreted momentum inside the accretion radius, and $\dot{M}(< R_{\rm a})$ is the accreted mass.

Numerical integration in the vertical direction from the initial density profile can then provide

$$\dot{M}(< R_{\rm a}) = v_\infty \int_{<R_{\rm a}} \rho(y)\ dA, \tag{2.12}$$

and

$$\dot{L}_z(< R_{\rm a}) = v_\infty^2 \int_{<R_{\rm a}} \rho(y) y\ dA. \tag{2.13}$$

The circularization radius therefore depends solely on the initial density profile, which in turn is set by $\Gamma_{\rm s}$ and ϵ_ρ. For the conditions of our numerical simulations, with $\epsilon_\rho = 2$, we find $R_{\rm circ} = 0.35 R_{\rm a}$ for $\Gamma_{\rm s} = 4/3$ and $R_{\rm circ} = 0.33 R_{\rm a}$ for $\Gamma_{\rm s} = 5/3$.

2.3 Numerical Results

In homogeneous HLA, where there is no density gradient, the gravity of the object focuses gas into a stagnation region that trails behind it. Gas then flows into the object primarily in the opposite direction of the incoming material. The introduction of an upstream density gradient breaks the symmetry of the problem, altering the flow structure by introducing net angular momentum. Without the cancelation of momentum in the trailing stagnation region, the rate of mass accretion is drastically reduced when a gradient is introduced (MacLeod & Ramirez-Ruiz 2015a,b; MacLeod

et al. 2017a).

Figure 2.1 shows the structure of the flow in the orbital plane for different adiabatic indexes. All simulation slices are plotted at $t = 25R_a/v_\infty$. Due to the vertical density gradient, the incoming flow is preferentially deflected towards the lower density material located at the outer edges of the envelope. The flow lines clearly show that most of the dense material, rather than being focused into the embedded object, is slingshotted into a counter-clockwise vortex. One or more angular momentum redistribution shocks form, which allow lower-density material to be accreted more favorably by the embedded object.

A key property of the flow in our simulations is that there is a constant flux of new material flowing toward the accreting object. Interaction with this steady flow defines the structures seen in Figure 2.1. As the compressibility of the gas increases, there is an increase in the density near the accretor in order to maintain ram pressure balance with the incoming material (with $P \propto \rho^\gamma$ along an adiabat, low γ implies a need for high ρ to match a pressure $P_{\rm ram} \approx \rho_\infty v_\infty^2$). The high densities near the accreting object imply that large quantities of material have pierced into the circularization region $r < R_{\rm circ}$. Visually in Figure 2.1, we can see that the mass of material in the circularization region increases dramatically as we go from $\gamma = 5/3$ to $\gamma = 1.1$. Additionally, the centrifugal support of gas near the accretor is most prominent (both in streamlines and in density slice) when the flow is highly compressible.

We find that the ability for the incoming flow to settle into a dense, rotationally-supported disk depends sensitively on the vertical structure of the flow, which is illus-

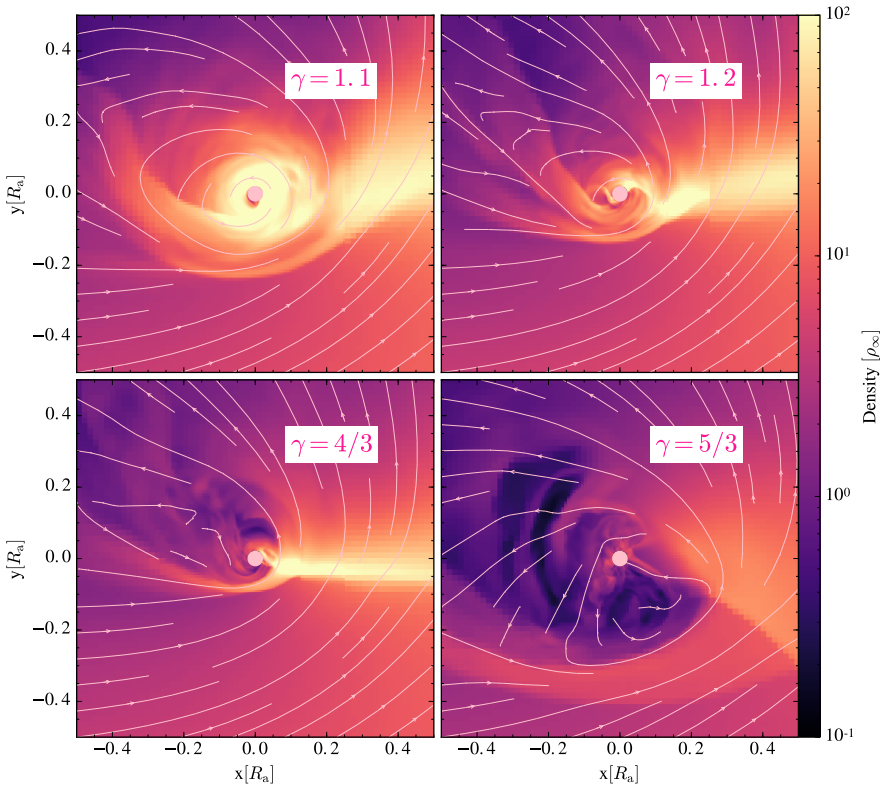

Figure 2.1: Comparison of the flow morphologies in the orbital plane ($z = 0$) with varying adiabatic indexes. All simulations are plotted at $t = 25R_a/v_\infty$. The simulation parameters are $\epsilon_\rho = 2$,$f_k = 1$, and $R_s = 0.02R_a$. The density has units of ρ_∞. The wind is coming from the -x direction. As can be seen, the density gradient tilts the shock, allowing for denser material to be deflected towards the outer edge, and the lower density material is more favorably accreted. The streamlines show that in the lower γ cases, a rotationally-supported structure can be formed.

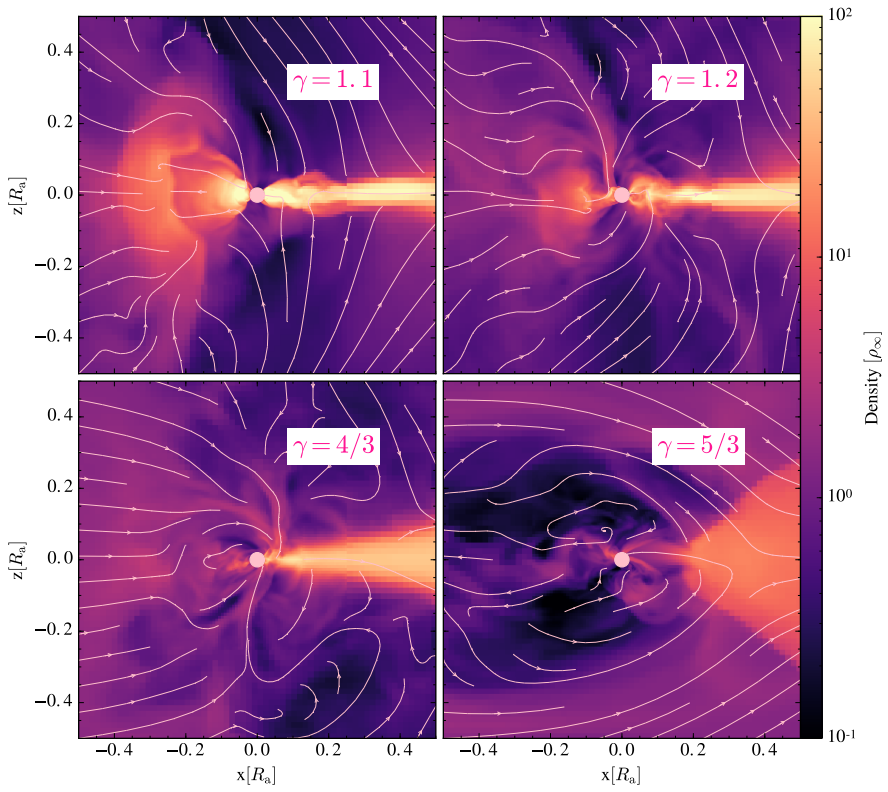

Figure 2.2: Density and flow structure for the same frames plotted in Figure 2.1 but in the plane perpendicular to the orbit ($y = 0$). The wake is more narrow and less dense in the more compressible media. In all cases the flow is deflected toward the wake. In the $\gamma = 5/3$ case, the streamlines are deflected away from the accretor, creating cavities.

trated in Figure 2.2. Because of the varying thermal properties of the gas, the convergence region becomes narrower and more concentrated along the plane as the flow increases its compressibility. This enhanced vertical compression implies decreasing pressure relative to rotational support.[1]

To aid in understanding whether fluid is able to approach the region of effective circularization, in Figure 2.3 we have plotted the ratio of the absolute value of accelerations on the gas for $\gamma = 1.1$ and $\gamma = 4/3$. In the highly compressible case, we see that the gravitational force from the embedded object dominates over the pressure gradient in most directions. This allows a sizable number of flow lines to pierce into the circularization region without being substantially deflected by the collisional properties of the gas. For $\gamma = 4/3$, on the other hand, the pressure gradient tends to dominate over the gravitational force and the flow is largely deflected away from the accretor. Perpendicular to the orbital plane, the motion of the adiabatic flow lines is influenced by the pressure gradient, thus leading to sizable defections of the flow away from the circularization region (with convergence happening primarily in the wake). These deflections, as argued above, are less prominent in the $\gamma = 1.1$ case, which allows the gas to settle into a rotationally-supported structure.

We explore the properties of this circularizing material further using our Lagrangian tracer particles of the simulation flow. Figure 2.4 selects particles that reside in the circularization region for more than 15% of the time for which the particles are injected ($5R_{\rm a}/v_\infty$). The trajectories plotted in Figure 2.4 are a randomly selected 10%

[1] We note that the convergence of flow lines into a dense structure near the accretor leads the mass accretion rate to increase with decreasing γ by an order of magnitude between $\gamma = 5/3$ and $\gamma = 1.1$.

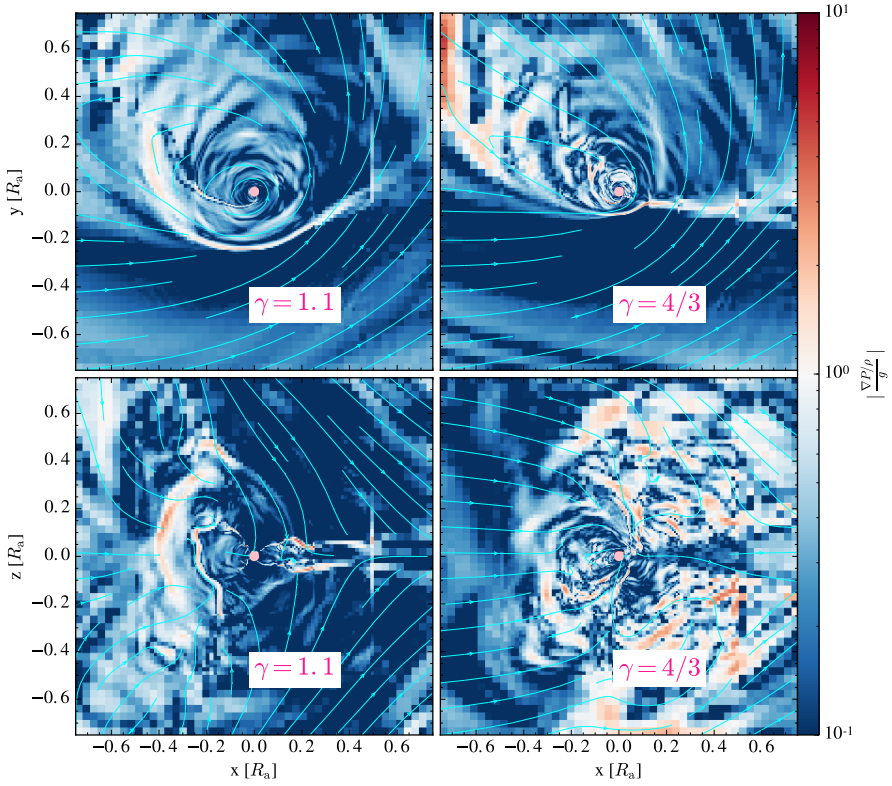

Figure 2.3: Shown are the absolute value of the radial components of the pressure gradient over the gravitational force per unit density due to the embedded object ($g = GM_2/r^2$). The snapshots are the same as in Figures 2.1 and 2.2. The ratio of the forces in the orbital (top panel) and perpendicular (bottom panel) planes are shown for $\gamma = 1.1$ and $\gamma = 4/3$. For the case of $\gamma = 1.1$, gravitational forces usually dominate over the pressure gradient near the embedded object, allowing the flow to reach the circularization region. In the $\gamma = 4/3$ case, the pressure gradient dominates at large distances, which leads to stronger deflections of the flow. As a result, the flow is unable to enter the circularization region.

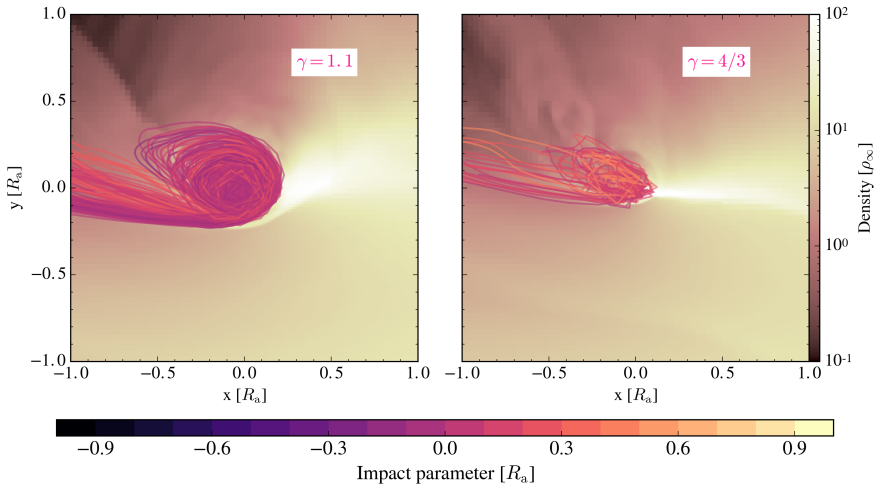

Figure 2.4: Trajectories of 10% of the injected tracer particles (randomly selected) belonging to the disk region for an adiabatic index of $\gamma = 1.1$ (left panel) and $\gamma = 4/3$ (right panel). We define particles that are part of the disk as particles that spend more than 15% of the total time inside the circularization radius. Also shown is the initial impact parameter of each tracer particle and the density structure of the flow in units of ρ_∞.

of those particles meeting the selection criteria. Color indicates the initial impact parameters of the particles as injected into the domain. For $\gamma = 4/3$, a very small fraction of particles settle into the circularization region since most of them are deflected by the pressure gradient at larger distances. A much larger number of tracer particles reside in the disk region when $\gamma = 1.1$.

Interestingly, Figure 2.4 also shows that fluid entering the circularization region in the $\gamma = 1.1$ case originates almost entirely from impact parameters at or above the y-coordinate of the embedded, accreting object. In the context of the CE this corresponds to material at or outside the separation of the inspiralling object. The angular momentum redistribution shocks, coupled with the steep density gradient, appear to be the root of this behavior. In these shock structures angular momentum (relative to the

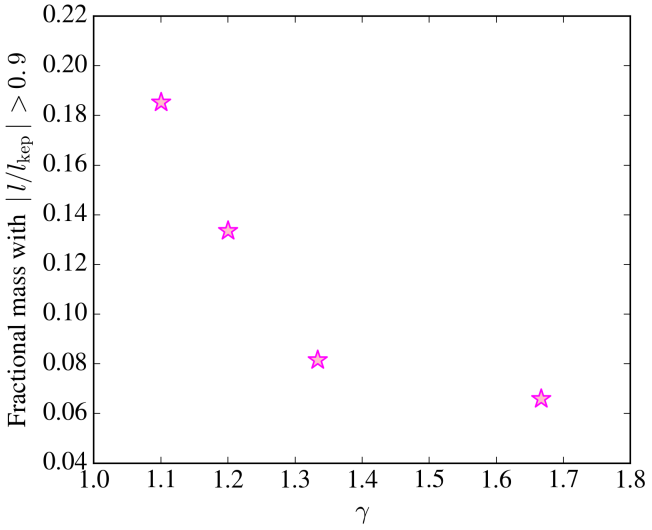

Figure 2.5: Fractional mass inside the circularization radius and a height $z = 0.1R_{\rm a}$ with specific angular momentum $\mid l/l_{\rm kep} \mid > 0.9$, where $l_{\rm kep} = \sqrt{r/2}$ in our code units as a function of adiabatic index. The mass is normalized by the total mass inside the circularization radius. The total amount of mass with nearly Keplerian angular momentum decreases with decreasing compressibility, as the flow is unable to drill beyond $R_{\rm circ}$.

embedded object) is transferred between fluid at positive and negative y impact parameters. The transfer is preferentially from the higher angular momentum material to lower angular momentum material. Post-shock, material that has specific angular momentum capable to rotate at $r \approx R_{\rm circ}$ already interacted with the denser material and gained significant angular momentum. The fact that material from $+y$ impact parameters has $+z$ angular momentum indicates that the direction of the angular momentum vector of these tracer particles was reversed as they passed through the redistribution shocks.

The above analysis suggests that there is a critical adiabatic index below which a dense, rotationally-supported structure can be formed with these wind-tunnel flows. Figure 2.5 shows the total mass within the circularization radius that is rotationally-

supported, defined here as having $| l/l_{\rm kep} | > 0.9$. This highlights a conclusion which is visually obvious in Figures 2.1 and 2.2: a highly compressible flow allows for a large amount of rotationally-supported material, a structure that we would typically consider a dense disk. Figure 2.4 also shows that a relatively sharp transition occurs below $\gamma \approx 4/3$. In what follows, we consider $\gamma \approx 1.2$ to be the representative critical value for disk assembly, because our simulations with $\gamma \lesssim 1.2$ show disks, while those with $\gamma \gtrsim 4/3$ do not.

2.4 Discussion

2.4.1 Interpretation and Comparison to Previous Studies

In this work, we have found centrifugally supported structures only for highly compressible flows $\gamma \lesssim 1.2$. This differs from Armitage & Livio (2000), who reported disk formation in radiation-dominated ($\gamma = 4/3$) flows. The main reason for this discrepancy is undoubtedly the fact that they carried out simulations in two dimensions. In three dimensions, the flow can be deflected in the z-direction and is not restricted to the orbital plane. This additional degree of freedom hinders disk formation (Ruffert 1997). MacLeod & Ramirez-Ruiz (2015a) argued that pressure support under compression in two dimensions with an adiabatic equation of state ($\gamma = 5/3$) is very similar to that in a three-dimensional simulation with a nearly isothermal equation of state ($\gamma = 1$). This is because $P \propto \rho^{\gamma} \propto V^{-\gamma}$, where V is the volume term. In two dimensions we then have $P_{\rm 2d} \propto r^{-2\gamma}$, while in three dimensions we can instead write $P_{\rm 3d} \propto r^{-3\gamma}$. As a result, $P_{\rm 2d} \propto r^{-10/3}$ ($P_{\rm 2d} \propto r^{-8/3}$) for $\gamma = 5/3$ ($\gamma = 4/3$) and $P_{\rm 3d} \propto r^{-5}$ ($P_{\rm 3d} \propto r^{-3}$)

for $\gamma = 5/3$ ($\gamma = 1$).

Our analysis in Section 2.3 indicates that the radial component of the pressure gradient is more important than the pressure itself, because this is the quantity that enters into the gas momentum equation, as $\nabla P/\rho$. If we consider the idealized case of spherical compression, the pressure gradient term, in three dimensions with a nearly isothermal equation of state or in two dimensions with an adiabatic one, $\frac{1}{\rho}\frac{dP}{dr} \propto r^{-1}$. By contrast, the pressure gradient in three dimensions is $\frac{1}{\rho}\frac{dP}{dr} \propto r^{-3}$ for an adiabatic flow. Thus, near the embedded object, the resistance to compression due to the pressure gradient is much stronger for the adiabatic case than for the isothermal one. Figure 2.6 compares simulations in three and two dimensions with $\gamma = 4/3$. The flow in two dimensions is rotationally-supported, as also seen by Armitage & Livio (2000), while the increase in pressure support in three dimensions does not allow the flow to circularize.

A sufficiently strong pressure gradient can act effectively against the gravitational force of the embedded object, which goes as $\propto r^{-2}$. Returning to our three-dimensional flow structures, this leads to larger deflections of the flow in the $\gamma = 5/3$ case, as observed in Figures 2.1 and 2.2, which prevent the formation of a dense disk. If the resistance of a pressure gradient against gravity is the controlling parameter, we find that these both scale as r^{-2} for $\gamma = 4/3$, implying that in initial ratio of pressure support to gravitational acceleration is preserved at all radii under spherical compression. To settle into a disk, we can imagine that fluid needs to have a pressure-gradient scaling shallower than r^{-2}, so that gravity can become dominant at some radii and a rotationally-supported flow can develop. This logic predicts a bifurcation in flow struc-

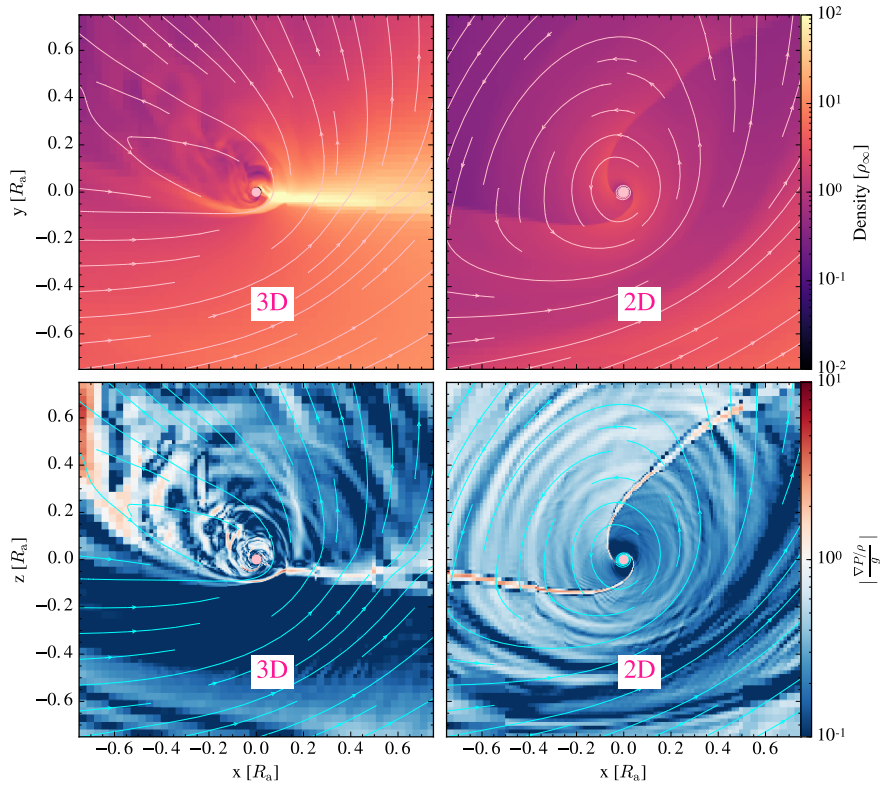

Figure 2.6: Differences between a two-dimensional simulation and a three-dimensional simulation. Both simulations share the same initial conditions, $\gamma = \Gamma_s = 4/3$, $q = 0.1$,$f_k = 1$, $\epsilon_\rho(y = 0) = 2$, $R_s = 0.02R_a$. The flow is depicted in both cases at a time $t = 25R_a/v_\infty$. The initial number of blocks is $8 \times 5 \times 5$ (three dimensions) and 8×5 (two dimensions). The minimum refinement level is 2, and the maximum refinement level is 8 for both cases. Shown are the density (top panels) and the absolute value of the radial component of the pressure gradient over the gravitational force per unit density (bottom panels), in the region near the accretor. The gravitational force dominates near the accretor in two dimensions, whereas the pressure support is significant in three dimensions. This results in a rotationally-supported structure for two dimensions that is not present in three dimensions.

ture above and below $\gamma \approx 4/3$. Our results of Section 2.3 support that prediction: only in calculations with $\gamma < 4/3$ ($\gamma \lesssim 1.2$) did we find dense disks on the scale of $R_{\rm circ}$.

2.4.2 Where in CE inspiral can disks form?

As discussed previously, during a CE event, a rotationally-supported structure could form around the embedded object in the presence of highly compressible gas. Natural questions then arise: where in a stellar envelope can this occur? And what is the scale of the associated disk?

The highest compressibility environment found in stars is within partial ionization zones. In these zones where the gas is partially ionized, a fraction of the energy released during a layer's compression can be used for further ionization, rather than raising the temperature of the gas (Harpaz 1984). The partial ionization produces an opacity bump and a considerable decrease in the adiabatic exponents. As a result, a steeper temperature gradient is required in order for radiative diffusion to transport energy through these regions.

Such partial ionization zones are located in the outer layers of evolving stars. To illustrate this, we calculate stellar models with MESA (version 7624; Paxton et al. 2011, 2013, 2015) for stars of different mass and evolutionary stages [2].

As the star evolves into the giant branch, the partial ionization regions occupy a

[2] We evolved the stars with masses $M_1 = 15, 20, 30, 40, 50, 60, 70, 80 M_\odot$ using the `150M_z1m4_pre_ms_to_collapse` test suite setup, but changing the initial mass and metallicity accordingly. The setup does not alter the `inlist_massive_defaults`, which includes a mixing length of 1.5 and a 'Dutch' wind scheme for both RGB and AGB winds. The stars with masses $M_1 = 1, 2, 5, 10 M_\odot$ were evolved using the setup from the test suite `7M_prems_to_AGB`, but, again, changing the masses accordingly. The setup uses a mixing length of 1.73, and a 'Reimers' and 'Blocker' RGB and AGB wind schemes respectively. The corresponding inlists are available upon request.

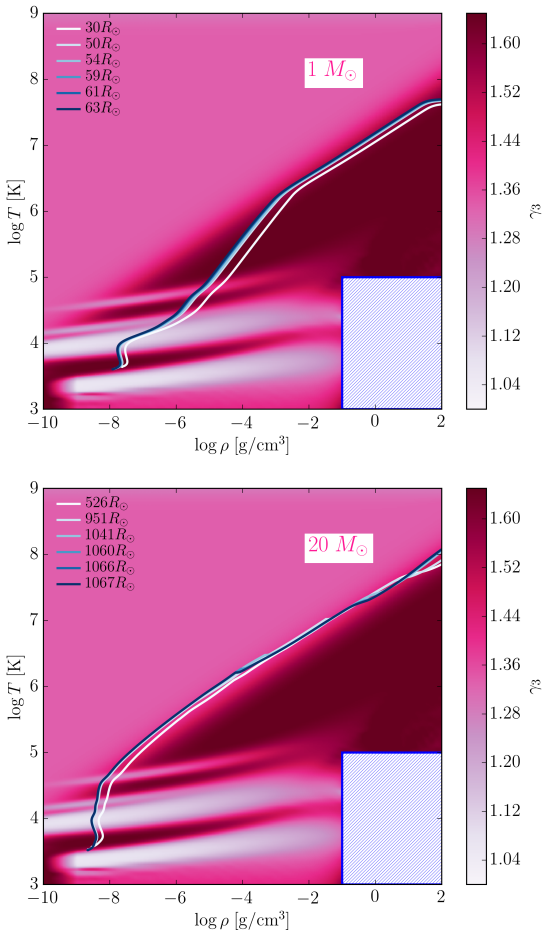

Figure 2.7: Mapping of γ_3 in stars with solar abundances. Over-plotted are the tracks of stars with $M_1 = 1M_\odot$ (top panel), and $M_1 = 20M_\odot$ (bottom panel) for different evolutionary stages. The dashed area represents a region in the $\rho - T$ plane where crystallization occurs and the equation of state is not well determined (Paxton et al. 2011). The regions with low adiabatic index correspond to partial ionization zones (Harpaz 1984). In most stars there are two main ionization zones. The hydrogen partial ionization zone where both the ionization of neutral hydrogen $\mathrm{H} \leftrightarrow \mathrm{H}^+ + \mathrm{e}^-$ and the first ionization of helium $\mathrm{He} \leftrightarrow \mathrm{He}^+ + \mathrm{e}^-$ occurs in layers with a characteristic temperature of 1.5×10^4 K. The second involves the second ionization of helium $\mathrm{He}^+ \leftrightarrow \mathrm{He}^{++} + \mathrm{e}^-$, which occurs in deeper layers with a characteristic temperature of 4×10^4 K. Upon compression, internal energy is partially deposited into increased ionization within these regions, lowering γ_3.

progressively larger fraction of the mass of the star. This can be seen in Figure 2.7, where we have mapped the compressibility that enters into the equation of state, γ_3 (equation 2.5), in the $\rho - T$ plane using the equation of state module in MESA (Paxton et al. 2011, 2013, 2015). Over-plotted are the evolutionary tracks for $1M_\odot$ stars and $20M_\odot$ stars at various evolutionary stages and solar abundance. The dashed area represents the region where crystallization occurs and the equation of state is not well determined.

The almost horizontal (constant T) white bands in Figure 2.7 represent regions in which partial ionization of various species takes place and, as a result, the gas is highly compressible. The regions of high compressibility are more prominent in low mass stars, whose envelopes cross through larger portions of these regions. High mass giants approach their Eddington limit and show profiles in the $\rho - T$ plane that straddle the gas-radiation pressure transition. These profiles touch the partial ionization regions in $\rho - T$ space only at their extreme limbs, occasionally in regions of density inversion.

Figure 2.8 shows the fractional radius of stars that have $\gamma_3 < 1.2$. As can be clearly seen in Figure 2.8, low mass stars have significantly more extended partial ionization zones in their outer layers. Higher mass stars, above $\approx 3M_\odot$ exhibit radially narrow partial ionization zones with $\lesssim 1\%$ of their radius occupied by these regions.

2.4.3 Implications for disk formation

Next we address the scale of a disk that might result from passage of a secondary object through one of these regions of high gas compressibility. Figure 2.9 illustrates how the gas circularization radius, $R_{\rm circ}$, changes as the embedded object, here characterized by $R_{\rm a}$, spirals deeper into the star. This figure adopts $q = 0.1$. As

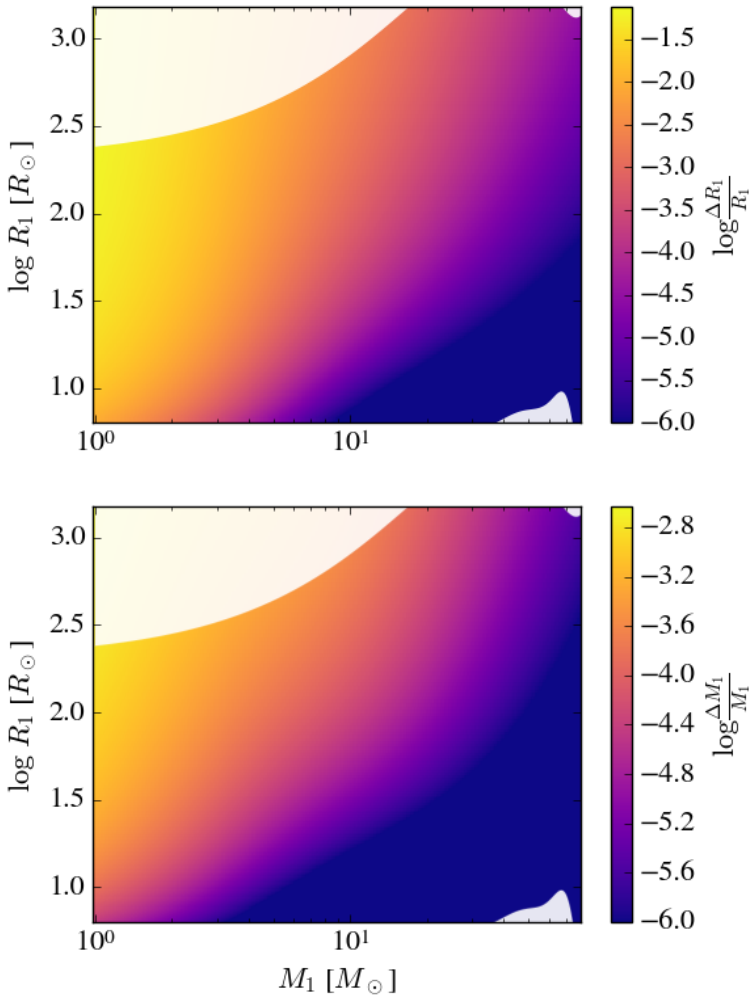

Figure 2.8: Mapping of regions with high compressibility in solar metallicity stars. Plotted is the fractional radius (top panel) and fractional mass (bottom panel) as a function of initial mass and stellar radius along the evolution of that star having a high compressibility zone ($\gamma_3 < 1.2$). The region of highly compressible media is significantly more extended in low mass stars compared to high mass stars.

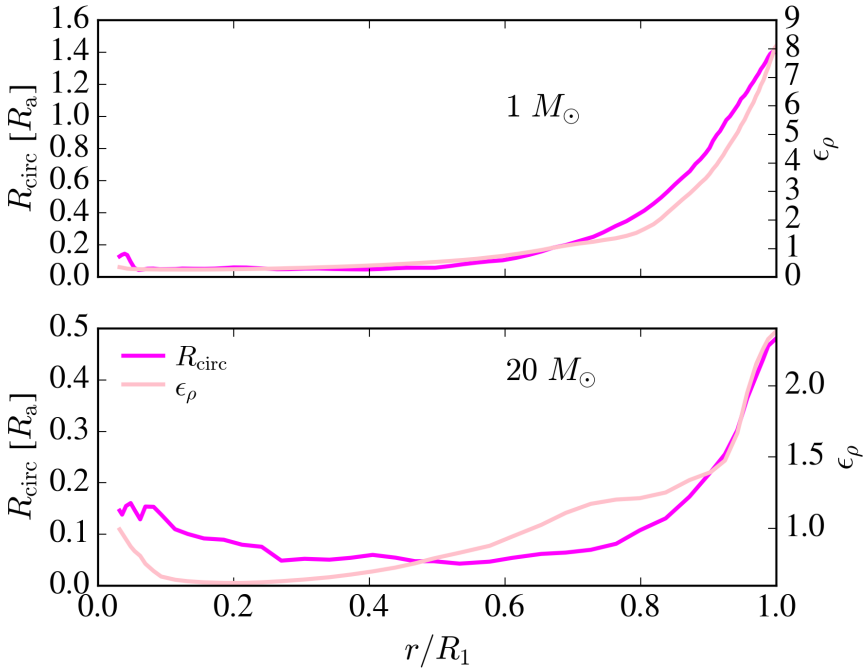

Figure 2.9: Circularization radius and density gradient as a function of stellar radius for a 1 $M_\odot$ primary star with $R_1 = 30$ $R_\odot$ at 6.3×10^9 years and a helium core of $0.35 M_\odot$ (top panel), and a 20 $M_\odot$ primary star with $R_1 = 1000$ $R_\odot$ at 8.1×10^6 years and a helium core of $4.9 M_\odot$ (bottom panel). Both stars have solar metallicity, and the binary mass ratio is assumed to be $q = 0.1$. This figure was made using MESA (version 7624; Paxton et al. 2011, 2013, 2015). The circularization radius, as a fraction of $R_{\rm a}$, is highly dependent on the local density gradient. It is similar to $R_{\rm a}$ in the outer portion of the stellar envelope, but then decreases to $R_{\rm circ} \sim 0.1 R_{\rm a}$ for much of r/R.

the embedded companion spirals deeper into the primary, density gradients, as parameterized by ϵ_ρ, become shallower, and the circularization radius decreases relative to $R_{\rm a}$. Rotationally supported structures will have scale similar to $R_{\rm a}$ only in the outer portions of stellar envelopes, in similar regions to where zones of partial ionization (and high compressibility) are found.

We expect that only in cases where the radial extent of highly compressible gas ($\gamma < 4/3$) is sufficiently large, $\Delta R_1 \gtrsim R_{\rm a}$, is it possible for a large scale disk structure

at the $R_{\rm circ}$ scale to be formed around the embedded object. This figure indicates that, given the unperturbed structures of stellar envelopes, disk assembly might be restricted to objects embedded in the outer envelopes of low-mass giant stars. Furthermore, by comparison to Figure 2.8, for $R_{\rm a} \lesssim \Delta R_1$, to occur, the encounter must be one with a low mass secondary object and correspondingly low mass ratio, q, such that $R_{\rm a} \ll a$. Taken together, these considerations suggest that disk formation in CE is rare, and is probably only a brief phase during the inspiral in cases in which it does occur.

Several caveats affect the firmness of this conclusion. CE structures are undoubtedly expanded by interaction with the secondary star, perhaps even prior to the phase when an object plunges through a given radial coordinate. This expansion, and associated adiabatic degradation of the temperature of the expanded envelope, could lead larger portions of the $\rho - T$ trajectories of massive stars to cross through partial ionization zones. A second concern relates to the extension of our wind-tunnel results to the realistic CE process. In particular, in a full equation of state, such as that shown in Figure 2.7, γ_3 is a strong function of density and, especially, temperature. This might lead to different structures (and degrees of pressure support) as the gas compresses through various phase transitions, perhaps differentiating the dynamics of the system under a realistic equation of state from that with a constant γ. For now, we can speculate that the important scale is the circularization radius scale, where the angular momentum budget is dominated, but performing more complex simulations is beyond the scope of the current work. An additional caveat is that, although this paper mainly considers the formation of accretion disks during the common envelope phase,

in principle, the secondary could enter the common envelope with a pre-existing disk (Chen et al. 2017; Staff et al. 2016) formed due to mass transfer before the CE phase.

A disk would transport mass, energy and angular momentum to small scales from which it might generate accretion-driven winds and collimated outflows that aid in ejecting the envelope (Armitage & Livio 2000; Voss & Tauris 2003; Soker 2004, 2015). There are some interesting results that accompany the collimated outflow formation. As the jet traverses through the star, the jet will deposit some of its energy into a cocoon that surrounds the jet (Moreno Méndez et al. 2017). The cocoon will expand laterally and in doing so quench the mass accretion onto the companion. Another interesting effect is that, since this energetic feedback occurs preferentially in the outer regions of the star, the close binary could eject a portion of the envelope early and enter a grazing envelope phase (Soker 2015; Shiber et al. 2017). If the feedback is strong enough, the common envelope phase might not fully occur.

2.4.4 Implications for binary black holes

The first detection of gravitational waves was catalyzed by the existence of moderately massive, stellar-mass black holes in binary systems (Abbott et al. 2016d). One of the preferred channels for the formation of this type of binary black holes necessitates a CE stage (Kruckow et al. 2016; Belczynski et al. 2016; Dominik et al. 2012; Belczynski et al. 2016). This channel involves a massive stellar binary ($40 - 100 M_{\odot}$), likely formed in a low-metallicity environment, in which the first-born black hole is engulfed by an evolving massive companion (Belczynski et al. 2016). For the merger to occur within the age of the universe, the black hole needs to tighten its orbit.This

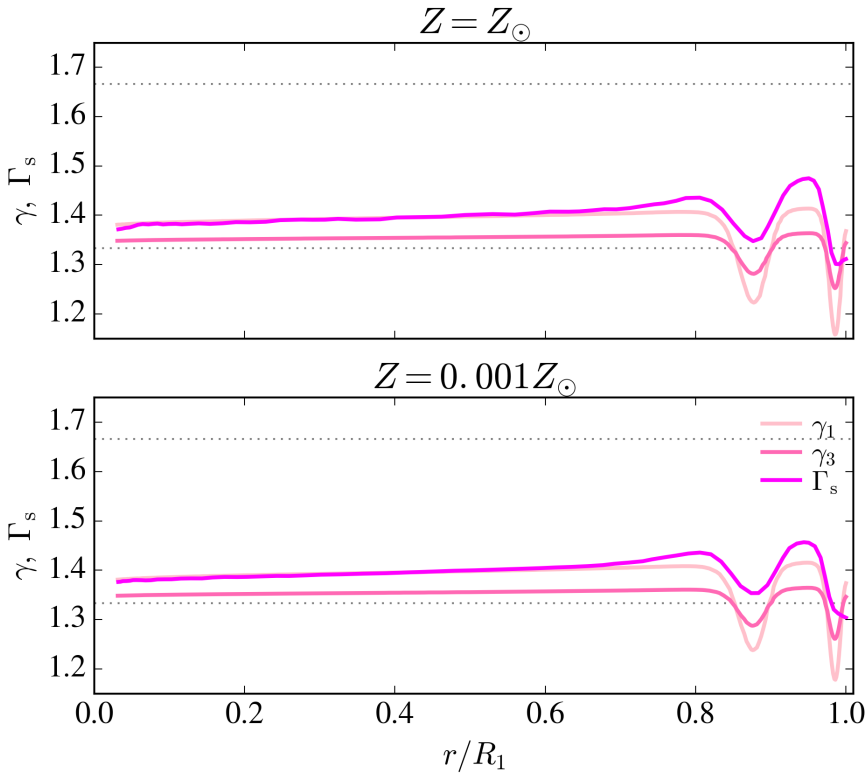

Figure 2.10: Adiabatic indexes γ_1, γ_3, and structural index Γ_s in a $M_1 = 80M_\odot$ star. The top and bottom panels shows the profiles of stars with $Z = Z_\odot$ with $R_1 = 667R_\odot$ and $Z = 0.001Z_\odot$ with $R_1 = 667R_\odot$, respectively. The stars are in an evolutionary stage where, for the solar metallicity star the helium core has a mass of $35M_\odot$ and age of 3.2×10^6 years, and the lower metallicity star has a helium core of mass of $40M_\odot$ and age of 3.5×10^6 years. Stars were evolved using MESA's inlist (Paxton et al. 2011, 2013, 2015) `150M_z1m4_pre_ms_to_collapse` test suite setup, but changing the mass, and metallicity accordingly. As can be seen, the partial ionization regions (where γ_1 and γ_3 dip) are narrow and independent of metallicity.

tightening could occur due to the CE phase, or through some mechanisms, such as tidal torques from circumbinary disks (Chen & Podsiadlowski 2017), after the envelope is ejected.

We argue here that accretion feedback is likely not to effectively operate during the CE phase when involving massive stars. As was shown in Figures 2.7 and 2.8, extended zones of sufficiently high gas compressibility for disk formation exist in the envelopes of low mass giants, and are found in zones of partial ionization. The extent of these zones is drastically reduced and they are only found in the outermost envelopes of the high mass stars that are relevant to the formation of binary black holes. In Figure 2.10 we additionally illustrate that this conclusion is not sensitive to varying metallicity.

Because no extended regions of sufficiently low γ exist to allow disks to form in CE events involving high mass giants, there is a lack of a mechanism (such as a disk outflow) to couple the accretion energy lost to an embedded black hole with the large scale flow. This implies that significant tightening of the orbit can take place without significant feedback energy injection from the embedded black hole. By avoiding strong feedback, CE events may serve as a mechanism to drive substantial orbital tightening, as originally envisioned (Webbink 1984), and are a natural channel to the formation of merging binary black holes (e.g. Belczynski et al. 2016; Kruckow et al. 2016).

2.4.5 Summary

In this paper, we study the conditions required to form a disk around the embedded companion during a CE phase. We studied the flows using the idealized

CEWT setup of MacLeod et al. (2017a). Some key conclusions of our study are:

1. The introduction of a density gradient in HLA allows for angular momentum to be introduced to the flow, which in turn opens the possibility for the formation of a disk around the embedded companion.

2. The formation of disk structures in the context of a CE phase is linked to the thermal properties of the envelope. In envelope gas with higher compressibility ($\gamma < 4/3$), the gravitational force dominates over the pressure support near the accretor, allowing for effective circularization of the material into a disk. On the other hand, in lower compressibility gas environments ($\gamma \gtrsim 4/3$), the pressure support dominates as the gas compresses toward the accretor. We find that a disk does not form and the flow will be advected away from the embedded object, typically completing less than one full rotation.

3. Within stellar envelopes extended regions of sufficiently compressible gas to allow disk formation around embedded objects are found only within zones of partial ionization, where the additional (ionization) degrees of freedom reduce γ significantly.

4. These partial ionization zones always comprise a small fraction of a stellar envelope radius or mass. They are more extended in the outer layers of low mass stars than in the exteriors of high mass stars. We therefore expect that disk formation around embedded objects in CE, is, at most, a transitory phase.

5. The lack of regions conducive to disk formation in high-mass stellar envelopes sug-

gests that CE episodes involving these stars, such as those in the assembly history of merging binary black holes, are not subject to strong disk-outflow powered accretion feedback. Without overwhelming feedback from accretion, we suggest that CE events in massive systems should proceed with significant orbital tightening as they draw on orbital energy as an CE ejection mechanism rather than accretion energy. The lack of feedback implies that CE events remain a natural channel for the formation of LIGO-source binaries that must be assembled into tight orbits from which they merge under the influence of gravitational radiation.

Chapter 3

Post merger phase: jets in short gamma-ray bursts

3.1 Chapter Abstract

The most popular model for short gamma-ray bursts (sGRBs) involves the coalescence of binary neutron stars. Because the progenitor is actually hidden from view, we must consider under which circumstances such merging systems are capable of producing a successful sGRB. Soon after coalescence, winds are launched from the merger remnant. In this paper, we use realistic wind profiles derived from global merger simulations in order to investigate the interaction of sGRB jets with these winds using numerical simulations. We analyze the conditions for which these axisymmetric winds permit relativistic jets to breakout and produce a sGRB. We find that jets with luminosities comparable to those observed in sGRBs are only successful when their

half-opening angles are below $\approx 20^{\circ}$. This jet collimation mechanism leads to a simple physical interpretation of the luminosities and opening angles inferred for sGRBs. If wide, low luminosity jets are observed, they might be indicative of a different progenitor avenue such as the merger of a neutron star with a black hole. We also use the observed durations of sGRB to place constraints on the lifetime of the wind phase, which is determined by the time it takes the jet to breakout. In all cases we find that the derived limits argue against completely stable remnants for binary neutron star mergers that produce sGRBs.

3.2 Introduction

Neutron star binary mergers (NSBMs) are sources of gravitational waves, and the most discussed model for short γ-ray bursts (sGRBs; Eichler et al. 1989; Paczynski 1991; Narayan et al. 1992). As the binary coalesces, the resulting object depends on the total merger's mass. If that mass is less than the maximum mass allowed by rigid rotation (constrained to be at least $\approx 2M_{\odot}$ by observations of PSR J0348+0432 and PSR J1614-2230; Demorest et al. 2010; Antoniadis et al. 2013), it can result in a supramassive neutron star. Furthermore, if it is greater than that threshold mass, the merger will become a hot, differentially rotating, hyper-massive neutron star (HMNS) surrounded by an accretion disk (e.g. Baiotti et al. 2008). The HMNS can either live stably for a long time, or undergo collapse to a black hole (BH) (Shibata & Taniguchi 2006; Baiotti et al. 2008; Ravi & Lasky 2014).

In the latter case, delayed collapse to a BH and significant mass loss can

occur after sufficient angular momentum transport from the inner to outer regions of the remnant. Several processes can act to transport angular momentum and drive collapse, including gravitational waves, neutrino-driven winds and magnetic fields (Lee & Ramirez-Ruiz 2007a). As the mass is accreted, jets can be launched from the compact object. Details about that process remain unsure as central engine models often invoke either prompt collapse to a BH (e.g. Murguia-Berthier et al. 2014) or formation of a rapidly spinning, highly magnetized HMNS (e.g. Zhang & Mészáros 2001; Metzger et al. 2008b; Rezzolla & Kumar 2015).

In order to discriminate between progenitor scenarios, we need to better understand how the emerging relativistic jet propagates through the surrounding medium (Mochkovitch et al. 1993; Rosswog & Ramirez-Ruiz 2003; Rosswog et al. 2003; Aloy et al. 2005; Aloy & Rezzolla 2006; Rezzolla et al. 2011; Palenzuela et al. 2013; Ruiz et al. 2016). There are many collimation mechanisms (and potential death traps) for relativistic jets (Lee & Ramirez-Ruiz 2007a) in a NSBM context, including dynamically ejected material from the tidal tails and various types of baryon-loaded winds produced during the HMNS phase (Siegel et al. 2014a; Perego et al. 2014a; Hotokezaka et al. 2013; Nagakura et al. 2014; Duffell et al. 2015; Sekiguchi et al. 2016). In this Letter we explore how the neutrino-driven and magnetically-driven winds produced during the HMNS phase shape the jet and determine under which conditions a jet can break out successfully. We use latitudinal density profiles taken from simulations of NSBMs in order to calculate a more realistic circumburst environment.

The Letter is structured as follows. Section 3.3 gives a description wind's prop-

erties derived from global NSBMs simulations and investigates how they can potentially alter the jet's properties. Section 3.4 describes the numerical methods used and presents a description of the jet's interaction, thought to be produced after the collapse to a BH, with the previously ejected wind material. Finally, in Section 3.5 we discuss the results obtained and compare them with observations of sGRBs.

3.3 Jet advancement and collimation

The properties environment's properties could hamper the jet's advancement. The jet should be able to break free from the baryon-loaded wind if the velocity of the jet's head is larger than that of the wind's material. By balancing momentum fluxes at the jet's working surface, we obtain (e.g., Begelman & Cioffi 1989; Bromberg et al. 2011)

$$\beta_h = \frac{\beta_j + \beta_w \tilde{L}^{-1/2}}{1 + \tilde{L}^{-1/2}} \tag{3.1}$$

for $\beta_{\rm h} > \beta_{\rm w}$, where $\beta_{\rm h}$ and $\beta_{\rm j}$ represent the velocities of the jet's head and the shocked material, respectively, and

$$\tilde{L} = \frac{\rho_{\rm j}}{\rho_{\rm w}\Gamma_{\rm w}^2} h_{\rm j}\Gamma_{\rm j}^2, \tag{3.2}$$

where $h_{\rm j}$ is the specific jet's enthalpy, $\Gamma_{\rm j}$ the initial jet's Lorentz factor, $\rho_{\rm j}$ and $\rho_{\rm w}$ the jet's and wind's density respectively. $\tilde{L}$ is the jet's critical parameter that determines the evolution (Bromberg et al. 2011), collimation can be attained if:

$$\tilde{L} < \theta_{\rm j}^{-4/3}, \tag{3.3}$$

where $\theta_{\rm j}$ is the jet's half-opening angle. For a jet with axial symmetry, its structure can be described by the angular distribution of its luminosity content per unit solid angle, $L_\Omega(\theta)$. For this discussion, we shall assume the jet is uniform, where L_Ω and $\Gamma_{\rm j}$ are constant within $\theta_{\rm j}$ and sharply decreasing at larger polar angles. Thus, L_Ω is the isotropic equivalent luminosity as, for example, derived from a fraction of the γ-ray luminosity. The complex nature of the HMNS close to critical rotation leaves open the possibility of the jet interacting with a non-spherical mass distribution: $\rho_{\rm w}(\theta)$. As we show in Section 3.3.1, the jet is likely to encounter a slower and denser wind confined to the equatorial plane. To compute the exact latitudinal dependence of the wind properties of HMNS we require global simulations that reproduce, as realistically as possible, the conditions expected in NSBMs.

3.3.1 Constraints derived from neutrino-driven and magnetically-driven winds

Considering the spectral frequencies of the gravitational wave signal of a NSBM (Rezzolla & Takami 2016), we can determine a dynamical timescale associated with the HMNS's rotation: $t_{\rm dyn} \approx 1$ms. Given the various stabilizing mechanisms, the HMNS is likely to survive for a timescale longer than $t_{\rm dyn}$. Thermal support in the HMNS is governed by neutrino diffusion where the cooling time is (Perego et al. 2014a)

$$t_\nu \approx 1.88 \left(\frac{R_{\rm ns}}{25\ {\rm km}}\right)^2 \left(\frac{\rho_{\rm ns}}{10^{14}\,{\rm g\,cm^{-3}}}\right) \left(\frac{k_{\rm B}T_{\rm ns}}{15\ {\rm MeV}}\right)^2 {\rm s}. \tag{3.4}$$

Stabilization of HMNS due to differential rotation is expected to last for many

$t_{\rm dyn}$ and is presumed to be halted by some dissipative mechanism, like viscosity, gravitational radiation, magnetic amplification and/or magnetic braking (Price & Rosswog 2006; Baiotti et al. 2008; Giacomazzo et al. 2011; Kiuchi et al. 2015a; Siegel et al. 2013; Kiuchi et al. 2015b). The characteristic timescale for magnetic braking of differential rotation by toroidal Alfvén waves is estimated to be of the order of $R/v_{\rm A}$ (Shapiro 2000):

$$t_{\rm A} \approx 0.17 \left(\frac{R_{\rm ns}}{25\ {\rm km}}\right)^{-1/2} \left(\frac{B}{10^{15}\ {\rm G}}\right)^{-1} \left(\frac{M_{\rm ns}}{3\ M_\odot}\right)^{1/2} {\rm s}, \tag{3.5}$$

where differential rotation has been assumed here to convert a fraction of the kinetic energy in differential motion in the (initially weakly magnetized) HMNS into magnetic field energy (e.g. Siegel et al. 2014a). These angular momentum transport processes push the HMNS to uniform rotation, which could lead to a collapse to a BH on a timescale $\ll t_\nu$ if the excess mass can not be supported (Fryer et al. 2015; Lawrence et al. 2015).

During the HMNS phase, these various dissipation and transport mechanisms give rise to significant mass loss. Because of the density and velocity structure in the HMNS, the mass loss is expected to be anisotropic (e.g. Rosswog & Ramirez-Ruiz 2003). The result is a remnant wind that originated in the presence of the HMNS. The numerical tools needed to study this problem have not been available until recently. Here we make use of the results of two global simulations of NSBMs aimed at, as realistically as possible, quantifying the properties of neutrino-driven (Perego et al. 2014a) and magnetically-driven (Siegel et al. 2014a) winds from HMNS, respectively.

The angular dependence of the winds are derived by fitting the latitudinal

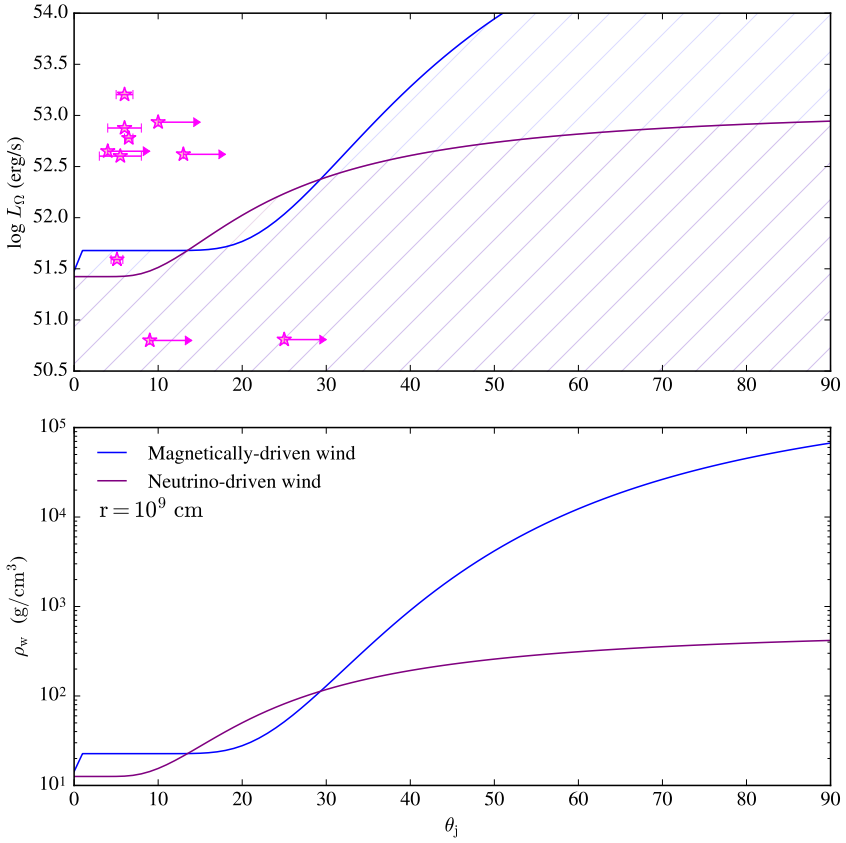

Figure 3.1: Top: L_Ω of a jet, uniform within θ_j, needed to have a successful sGRB assuming that the velocity of the jet's head is determined by $\rho_w = \rho_w(r, \theta_j)$. In the dashed region, the jet will be choked ($\beta_h < 2\beta_w$). Here, $\Gamma_j = 10$ and $\beta_w = 0.3$. The symbols represent the lower limit of $L_{\gamma,iso}$ calculated using *Swift* data and considering an efficiency factor of 30% in converting the kinetic luminosity of the jet into radiation. Angles are taken from Fong et al. (2015, 2016b); Troja et al. (2016). Bottom: The density profiles were derived based on the global simulations performed by Perego et al. (2014a) and Siegel et al. (2014a), respectively.

ram pressure profile at the end of the simulation in Perego et al. (2014a), and the `rand` configuration of Siegel et al. (2014a). The latitudinal ram pressure profile is evaluated close to the edge of the remnant, where the maximum ram pressure is attained. By assuming that the conditions at the end of the simulation are representative of the steady state of the wind, the corresponding density profile $\rho_w = \rho_w(r, \theta_j)$ can be calculated

taking the wind's velocity to be close to the escape velocity of the merger ($\beta_{\rm w} \approx 0.3$ in both cases). Then, we estimate the minimum L_Ω needed for a uniform sGRB jet to break free from the wind, which we assume needs $\beta_{\rm h} > 2\beta_{\rm w}$ at all angles. If we assume that the velocity of the jet's head is limited by its expansion along the highest density region within $\theta_{\rm j}$, we can use equation (3.1) with $\rho_{\rm w} = \rho_{\rm w}(r, \theta_{\rm j})$.

The resulting constraints are plotted in the Top panel Figure 3.1. For comparison, the distributions of isotropic equivalent γ-ray luminosities ($L_{\gamma,\rm iso} = E_{\gamma,\rm iso}/t_{90}$) and half-opening angles from Fong et al. (2015, 2016b); Troja et al. (2016) are also plotted. We note that the ensuing collimation will change $\beta_{\rm h}$ from the simple analytical estimate presented here. Our simulations show that $\beta_{\rm h}$ differs for this simple estimate by up to 30%. It is notable that the constraints derived from both sets of global simulations are rather similar and they are in agreement with observations, suggesting that the properties of sGRB jets are likely shaped by the wind's character.

We can also derive a limit on the wind injection's duration $t_{\rm w}$, which is determined by the time it takes the HMNS to collapse to a BH. The velocity of the jet's head is subrelativistic while traversing the wind. Thus, if the central engine stops the energy input in the jet's head before it breaks free, the head will stay subrelativistic and there will be no emission. The sGRB is successful if:

$$t_{\rm w} \leq t_{\rm sgrb} \frac{\beta_{\rm h} - \beta_{\rm w}}{\beta_{\rm w}}, \tag{3.6}$$

where $t_{\rm sgrb}$ is the event's duration. If equation (3.6) is satisfied, the jet will be able to produce a sGRB lasting $\approx t_{\rm sgrb}$. Figure 3.2 shows the limits on $t_{\rm w}$ for the sample same

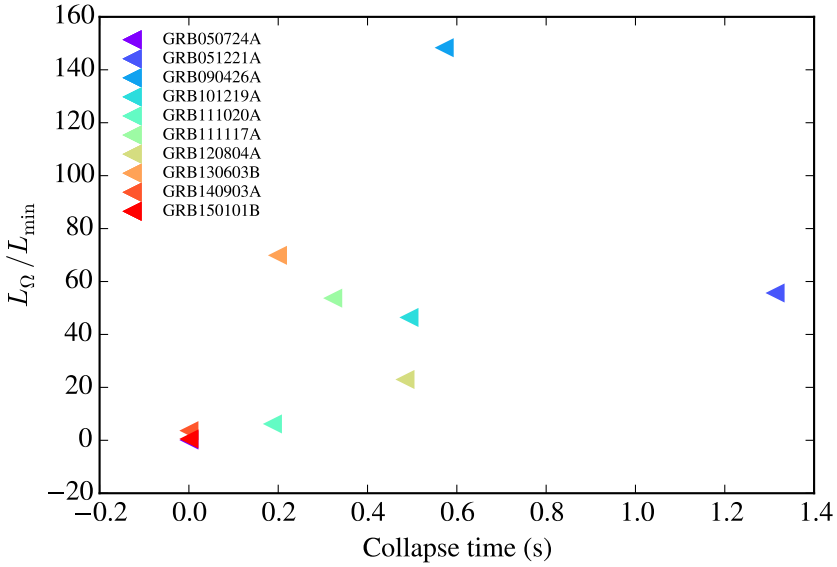

Figure 3.2: Predicted upper limit on the HMNS's lifetime, $t_{\rm w}$. The symbols represent the same data set as in Figure 3.1. $L_{\rm min}$ represents the minimum luminosity a jet with $\theta_{\rm j}$ needs to break free from the wind (below the line in Figure 3.1). One of the outliers is GRB050724A, whose luminosity is well below $L_{\rm min}$. In Section 3.5 we argue that GRB050724A could have been produced by the merger of a NS with a BH.

sample as Figure 3.1, derived by assuming that such jets need to successfully break free from the HMNS wind. In all cases, the required limits are $\lesssim t_\nu$ (equation (3.4)), which argues against the complete stabilization of the HMNS and suggests that the collapse to a BH occurs on a timescale $\approx t_{\rm A} \gg t_{\rm dyn}$ (see e.g. Murguia-Berthier et al. 2014).

3.4 Numerical Study

We performed 2D numerical simulations to quantify how the interaction of the wind, ejected during the HMNS phase, modifies the propagation of a relativistic jet, assumed to be produced after the collapse to a BH. The simulations were performed using the *Mezcal* special relativistic hydrodynamic code. It uses adaptive mesh refinement in

order to resolve the flows. A description can be found in De Colle et al. (2012a) along with tests.

The simulation setup follows that implemented by Murguia-Berthier et al. (2014). It begins with the injection of a slow ($\beta_{\rm w} = 0.3$), dense wind lasting for $t_{\rm w}$. After $t_{\rm w}$, the wind's density is decreased as $t^{-5/3}$ (e.g. Lee & Ramirez-Ruiz 2007b) and a jet is introduced. The jet should retain its structure before it decelerates, thus it is uniform and characterized by its luminosity (L_Ω), half-opening angle ($\theta_{\rm j}$), Lorentz factor ($\Gamma_{\rm j} = 10$) and duration ($t_{\rm j}$). We relax the assumption in Murguia-Berthier et al. (2014) of a uniform wind and explore the interaction with a non-spherical distribution: $\rho_{\rm w}(\theta)$, calculated using the same dependance as Figure 3.1. A denser wind will likely impede the jet's advancement.

Initially, the jet is unable to move the wind material at a speed comparable to its own and thus is decelerated to a Lorentz factor $\Gamma_{\rm h} \ll \Gamma_{\rm j}$. Most of the excess energy is accumulated within a cocoon that engulfs the jet (Ramirez-Ruiz et al. 2002). If the jet produced by the accretion onto the newly formed BH maintains its luminosity for longer than it takes the jet's head to reach the edge of the wind, a successful sGRB will be produced (as in the case depicted in the top panel of Figure 3.3). If the jet activity terminates beforehand, the jet will be choked (bottom panel of Figure 3.3).

The angular properties of the wind also have an important effect on the jet. Figure 3.4 shows the structure of jets varying $\theta_{\rm j}$. For narrow jets, the outer edge of the wind is reached in a crossing time that may matter little when compared to $t_{\rm j}$. Nonetheless, wider jets have to traverse higher density regions and they may be unable

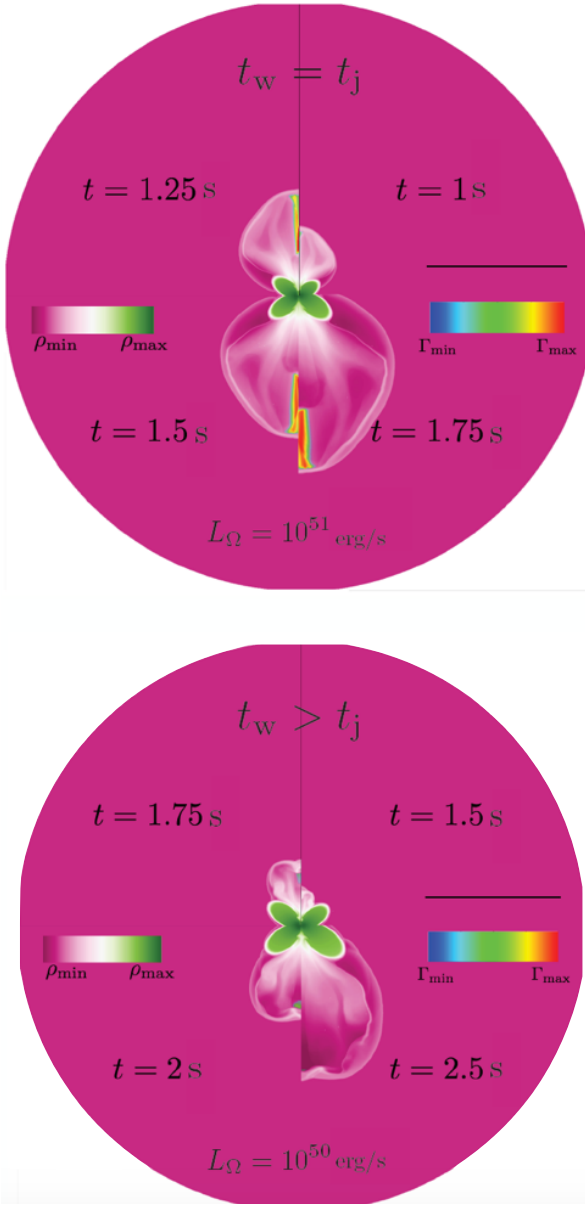

Figure 3.3: The temporal evolution of a jet propagating through a realistic wind. Top: The jet has $L_\Omega = 10^{51}$erg s^{-1}, $\Gamma_{\rm j} = 10$, $t_{\rm j} = 0.5$s, and $\theta_{\rm j} = 10°$. For the wind: $t_{\rm w} = 0.5$s. Bottom: The jet has $L_\Omega = 10^{50}$erg s^{-1}, $\Gamma_{\rm j} = 10$, $t_{\rm j} = 0.5$s, and $\theta_{\rm j} = 10°$, For the wind: $t_{\rm w} = 1$s. Shown are $\log\rho$ and Γ contours at different times. $[\rho_{\rm min}, \rho_{\rm max}] = [7.6 \times 10^{-7}, 1386.3]$g cm^{-3}, $[\Gamma_{\rm min}, \Gamma_{\rm max}] = [8.0, 10.0]$. A 3×10^{10}cm scale bar is shown. Calculations were done in 2D spherical coordinates using an adaptive grid of size $l_{\rm r} = 6 \times 10^{10}$cm, $l_\theta = \frac{\pi}{2}$, with 100×40 initial cells, and 5 levels of refinement (maximum resolution of 3.75×10^7cm).

to breakthrough despite having the same L_Ω. An initially wide jet could advance much faster along the rotation axis and may eventually escape along the direction of least resistance, getting further collimated before emerging. Figure 3.5 shows the relativistic energy per solid angle for configurations shown in Figure 3.4. Only narrow jets are able to successfully emerge from the wind region and, in some cases, experience significant collimation.

We can conclude that the properties surrounding a HMNS at the time the collapse to a BH occurs have a decisive effect on the propagation and jet's angular structure. Whether a sGRB will be observed depends not only on the power and jet's duration but also on its initial angular structure, and patchiness of the wind. Thus, the detection of a successful sGRB and its parameters provides a clear test of the neutron star merger model and the precise measurement of the duration, luminosity and jet's half-opening angle may help constrain the dimensions and mass distribution of the HMNS region.

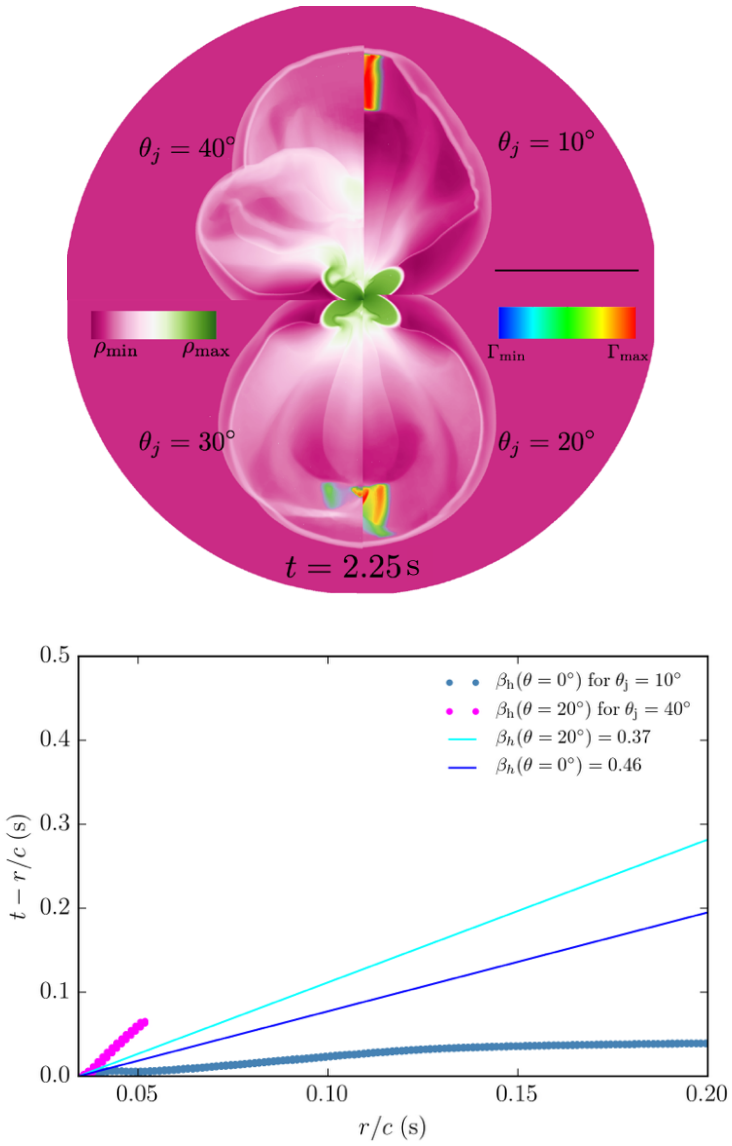

Figure 3.4: Top: The structure of jets interacting with a wind. The jet has $L_\Omega = 10^{51}$erg s^{-1}, $\Gamma_{\rm j} = 10$, $t_{\rm j} = 0.5$s and varying $\theta_{\rm j}$. For the wind: $t_{\rm w} = 0.5$s. Shown are $\log\rho$ and Γ contours at $t = 2.25$s. $[\rho_{\rm min}, \rho_{\rm max}] = [7.6 \times 10^{-7}, 1386.3]$g cm^{-3}, $[\Gamma_{\rm min}, \Gamma_{\rm max}] = [8.0, 10.0]$. The setup is the same as in Figure 3.3. Bottom: Space time diagram for the jet's head. Plotted with symbols are the position jet's head at different angles ($\theta = 0°$ and $\theta = 20°$) for the simulations with $\theta_{\rm j} = 10°$ and $\theta_{\rm j} = 40°$ shown above. $t = 0$s corresponds to $t_{\rm w}$. Analytical estimates for $\beta_{\rm h}$ at those specific angles are also plotted. The trajectory at 20° ends as the jet is choked.

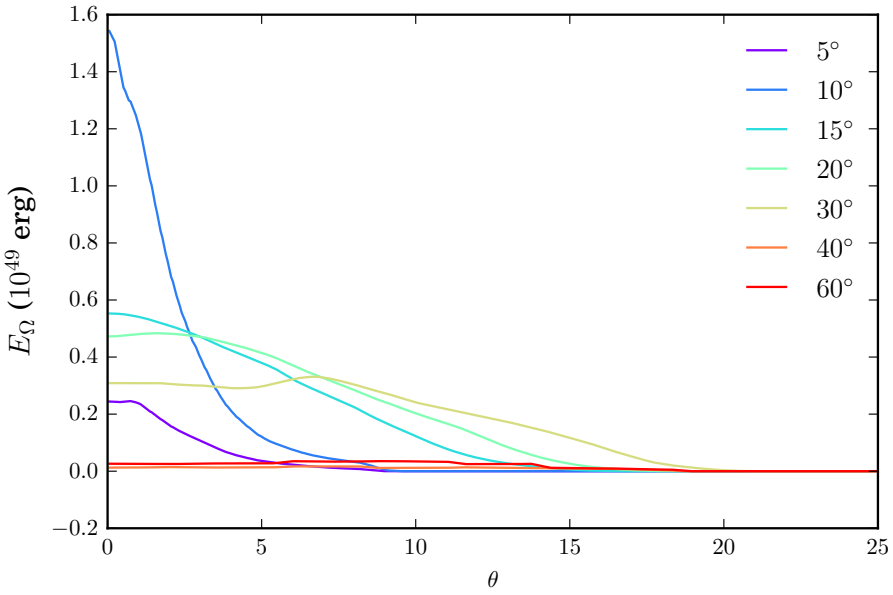

Figure 3.5: The distribution of relativistic energy ($\Gamma \gtrsim 8$) per solid angle averaged in radius for the jets in Figure 3.4, for varying initial jet half-opening angle $\theta_{\rm j}$.

3.5 Discussion

Soon after the coalescence of two neutron stars, dense mass outflows are generated within the HMNS. The resulting wind can hamper the advancement of a relativistic jet, potentially leading to a failed sGRB. To break free from the wind, we need two conditions.

First, the velocity of the jet's head has to be greater than that of the wind. For the realistic wind profiles analyzed here, we find that this constraint can be fulfilled if the jet's power exceeds some particular limit that increases with increasing opening angle. When compared to the observed distributions of isotropic equivalent γ-ray luminosities and half-opening angles (Fong et al. 2015, 2016b; Troja et al. 2016), the required constraints are in agreement with observations (Figure 3.1), giving credence to the idea

that the properties of sGRB jets are likely shaped by their interaction with the HMNS wind.

Second, the jet's head needs to emerge from the wind's outer boundary before the central engine ceases to operate. This requirement allows us to derive a limit on the duration of the wind injection phase, which is determined by the lifetime of the HMNS. Figure 3.2 shows the strict constraints on the time of collapse derived using the durations of sGRBs. In all instances, the required times of collapse are larger than the dynamical timescale of the HMNS but are significantly shorter than the cooling timescale of the remnant. This naturally argues against the complete stabilization of the HMNS and suggests that the collapse to a BH occurs promptly (Murguia-Berthier et al. 2014), which in turn can be used to constrain the equation of state of nuclear matter (Fryer et al. 2015; Lawrence et al. 2015). Because even a minuscule mass fraction of baryons polluting the sGRB jet severely limits the maximum attainable Lorentz factor, we argue that jet triggering has to be delayed until after BH collapse.

In this paper, we use realistic latitudinal wind profiles arising from global simulations reproducing the conditions of NSBMs (Siegel et al. 2014a; Perego et al. 2014a), that show that the HMNS experiences non-spherical mass loss and present a detailed numerical study of the propagation of relativistic jets in such environments. Many previous studies have addressed the role of external collimation (Rosswog et al. 2003; Siegel et al. 2014a; Perego et al. 2014a; Hotokezaka et al. 2013; Nagakura et al. 2014), using, for example, simple external medium solutions such as spherical (Bromberg et al. 2011) and oblate (Duffell et al. 2015) wind profiles. Here we find that jets with

$\theta_j = 40°$ are prone to be choked, whereas narrower jets of similar isotropic luminosity can emerge. We also find that in some limiting cases, wider jets might be able to break out of the wind region and emerge as more collimated outflows.

The resulting sGRB depends on the HMNS's properties, especially the wind's latitudinal structure. Thus, we cannot be too specific about the initial jet's structure when triggered. For example, neutrino pair annihilation is expected to produce jets with $\theta_j \approx 30°$ (Rosswog & Ramirez-Ruiz 2002), which also matches the half-opening angle of the magnetic-jet structure in NSBMs (Rezzolla et al. 2011), but these are likely to be further modified by the interaction with the surrounding environment. It also implies that low luminosity wider jets, can be constraining on the properties of their progenitor. The surrounding environment is expected to be less dense in the case of NS-BH progenitors. In such systems, the constraints on the properties needed for a successful event are not as stringent as in the case of NSBMs(Lee et al. 2004; Rosswog 2005; Just et al. 2016). The luminosity and opening angle of a sGRB would then provide a natural test to distinguish between different merger channels. We claim that this is the case for GRB050724 (Grupe et al. 2006), in which a low luminosity, wide jet event was observed. Fong et al. (2016a) rules a long lived for the sGRB. Given its properties, we speculate it was likely produced by a NS-BH merger that promptly collapsed to a BH. Rosswog (2005) and Just et al. (2016) argue that low luminosity events could be caused by neutrino pair annihilation or magnetized outflows in those types of mergers, respectively.

The task of finding useful progenitor diagnostics is simplified if the pre-burst

evolution leads to an enhanced wind medium in the jet's vicinity. The total luminosity and opening angles observed from sGRBs are diverse. One appealing aspect NSBM's progenitors is that the interaction with the winds of HMNS can probably explain this diversity.

Chapter 4

Lessons learnt from GW170817

4.1 Chapter Abstract

The merging neutron star gravitational wave event GW170817 has been observed throughout the entire electromagnetic spectrum from radio waves to γ-rays. The resulting energetics, variability, and light curves are shown to be consistent with GW170817 originating from the merger of two neutron stars, in all likelihood followed by the prompt gravitational collapse of the massive remnant. The available γ-ray, X-ray and radio data provide a clear probe for the nature of the relativistic ejecta and the non-thermal processes occurring within, while the ultraviolet, optical and infrared emission are shown to probe material torn during the merger and subsequently heated by the decay of freshly synthesized r-process material. The simplest hypothesis that the non-thermal emission is due to a low-luminosity short γ-ray burst (sGRB) seems to agree with the present data. While low luminosity sGRBs might be common, we show here that the collective prompt and multi-wavelength observations are also consistent

with a typical, powerful sGRB seen off-axis. Detailed follow-up observations are thus essential before we can place stringent constraints on the nature of the relativistic ejecta in GW170817.

4.2 Introduction

The discovery of galactic binary neutron stars (Hulse & Taylor 1975) firmly established the existence of a class of systems which would merge in less than a Hubble time via the emission of gravitational wave emission. Over the years, various studies showed that these binaries are in principle capable of powering cosmological γ-ray bursts of the short variety (Kouveliotou et al. 1993) when they merge (Paczynski 1986; Narayan et al. 1992; Eichler et al. 1989; Piran 2004; Lee & Ramirez-Ruiz 2007a; Gehrels et al. 2009; Kumar & Zhang 2015), while those of the long variety have been shown to be associated to the core collapse of massive stars (Woosley & Bloom 2006). After decades of instrumental, observational and theoretical progress, a watershed event occurred on 17 August 2017, when the Swope Supernova Survey discovered the first optical counterpart of a gravitational wave event, GW170817, attributed to the merger of two neutron stars (Abbott et al. 2017d), named SSS17a (Coulter et al. 2017a). This detection led to the measurement of a redshift distance and thus the firm identification of the candidate host galaxy, NGC 4993 (Coulter et al. 2017a; Pan et al. 2017).

One of the key electromagnetic discoveries concerned the detection of GRB 170817a by *Fermi* and INTEGRAL (Goldstein et al. 2017; Savchenko et al. 2017), a short γ-ray burst (sGRB) lasting only a few tenths of seconds. The short duration and

dim signal of the prompt γ-ray transient, however, precluded the determination of an accurate position until the Swope Supernova Survey succeeded in promptly localizing GRB 170817a/SSS17a (Goldstein et al. 2017; Savchenko et al. 2017; Coulter et al. 2017a). For the next few days, several multi wavelength observations were made (Savchenko et al. 2017; Haggard et al. 2017; Alexander et al. 2017; Abbott et al. 2017d). The detection of GW170817 and follow-up electromagnetic observations have revolutionized our view of merging neutron stars, confirming some previously held ideas and adding invaluable elements to our knowledge of them. The concept of a sudden release of energy almost exclusively concentrated in a brief pulse of γ-rays has been discarded. Indeed, even the term afterglow should be now recognized as misleading as the energy radiated during the first three weeks at longer wavelengths greatly exceeds that emitted during the prompt γ-ray phase (Goldstein et al. 2017).

The broad electromagnetic manifestations of GW170817 thus provide us with a unique opportunity, to which this Letter is dedicated, to constrain the ejecta properties following the merger of a binary neutron star. In Section 4.3 we address the energetics and timescales of the observed radiation and compare it with the data from sGRBs. In Sections 4.4 and 4.5 we constrain the properties of the ejecta by using all the information available to us from both the afterglow and prompt radiation. We summarize our findings in Section 4.6.

4.3 Metabolics of GW170817/SSS17a

Here we construct a basic inventory of the energy radiated at all wave bands from γ-rays to radio waves using all data collected for the GW170817 event by the One-Meter Two-Hemisphere (1M2H) collaboration (Coulter et al. 2017a; Drout et al. 2017; Kilpatrick et al. 2017; Shappee et al. 2017; Siebert et al. 2017) as well as from other publicly available sources (Alexander et al. 2017; Haggard et al. 2017; Savchenko et al. 2017). Such a basic inventory provides an assessment of the various modes of energy transfer and release involved within the ejecta. The compilation also offers a way to test our understanding of the physics of neutron star mergers. Some apparent points should be emphasized. We measure directly only the the energy radiated in the direction of the Earth per second per steradian per frequency interval by the source. The apparent bolometric luminosity $L_{\rm iso}$ may be quite different from the true bolometric luminosity if the source is not isotropic. To investigate the energy dissipation history we fitted a natural cubic spline function to the luminosity $L_{\rm iso}$ as a function of time at different frequency intervals. This allows us to estimate the cumulative emitted energy $E_{\rm iso}$ and also derive t_{90} values at all energies, which we define here as the time in the source frame during which 90% of the radiated energy is accumulated. Using this, we derive $E_{\rm iso}$ and t_{90} at γ-ray (75-2000 keV) from Abbott et al. 2017d, X-ray (0.3-10 keV), ultraviolet (2600-3465 Å), optical (3465-9665 Å), infrared (10200-21900 Å) and radio (5-10 GHz) energies:

- $E_{\gamma,\rm iso} \approx 5.3 \pm 1.1 \times 10^{46}$ erg and $t_{90,\gamma} \approx 2$ s
- $E_{\rm IR,iso} \approx 2.7 \pm 0.5 \times 10^{48}$ erg and $t_{90,\rm IR} \approx 10.5$ days

- $E_{\rm O,iso} \approx 4.1 \pm 0.4 \times 10^{47}$ erg and $t_{90,\rm O} \approx 3.8$ days
- $E_{\rm UV,iso} \approx 1.3 \pm 0.6 \times 10^{47}$ erg and $t_{90,\rm UV} \approx 1.1$ days
- $E_{\rm X,iso} \approx 1.9 \pm 0.5 \times 10^{44}$ erg and $t_{90,\rm X} \gtrsim 15.2$ days
- $E_{\rm R,iso} \lesssim 8 \times 10^{40}$ erg and $t_{90,\rm R} \gtrsim 17.7$ days

While unremarkable for its duration, GRB 170817a had a total energy that is some 4-6 orders of magnitude less than a typical *Swift* sGRB (Gehrels et al. 2009). The currently inferred isotropic X-ray emission $E_{\rm iso,X}$, which for most *Swift* sGRBs is comparable to that emitted during the prompt γ-ray phase, is at least 6-8 orders of magnitude smaller (Gehrels et al. 2009). The isotropic equivalent energy that is radiated at optical wavelengths in this case is 2 orders of magnitude larger than that in γ-rays. This is in stark contrast to *Swift* sGRBs, for which $E_{\rm O,iso}$ is at least 2 orders of magnitude smaller than $E_{\gamma,\rm iso}$. What is more, GW170817/SSS17a is radically different in its optical properties from any other known sGRBs (Siebert et al. 2017). The optical emission rises in less than half a day, then fades rapidly, exhibiting a swift color evolution to redder wavelengths (Drout et al. 2017). While optical sGRB afterglows can produce rapidly fading transients, they don't generate the quasi-blackbody spectrum that is observed in SSS17a (Shappee et al. 2017). These results are consistent with the emerging hypothesis that the ultraviolet, optical and infrared emission probe matter torn from the merger system, ejected at sub-relativistic velocities and subsequently heated by the decay of freshly synthesized r-process material (Kilpatrick et al. 2017; Kasen et al. 2017).

On its own, the low-luminosity γ-ray emission of the unusually faint GRB 170817a can thus support the idea of a common class of intrinsically sub-energetic sGRBs. The

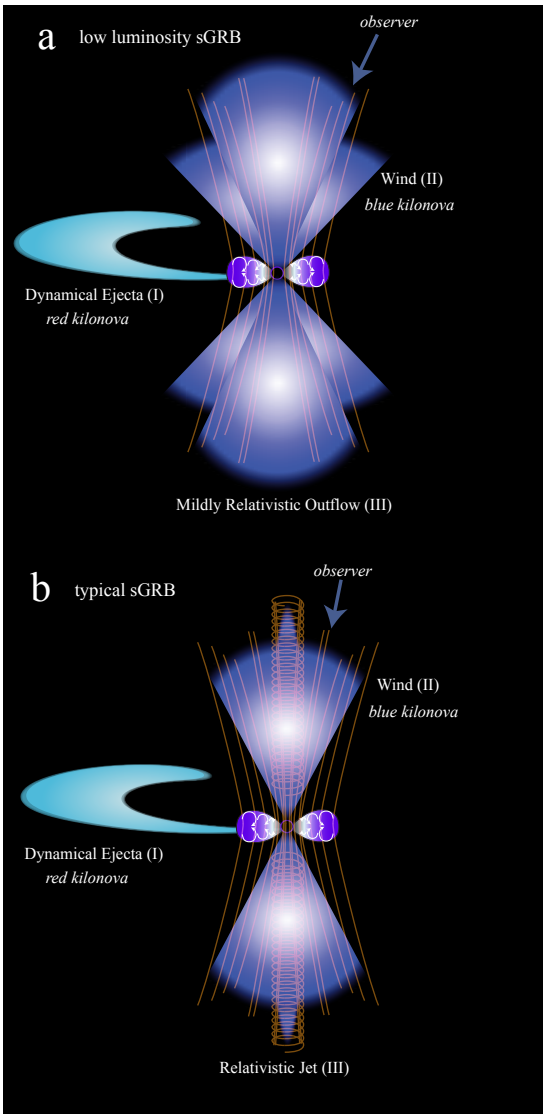

Figure 4.1: An overview of the main energy transfer processes thought to be involved in ejecting material in neutron star mergers. As they merge a few percent of the matter is ejected in the form of a tidal tail (I). The shocked merged remnant is expected to produce strong winds (II) and is likely to be top-heavy and unable to survive. The expected outcome is the collapse to a black hole. A spinning black hole constitutes an excellent gyroscope, and the ingredients of accretion and magnetic fields are probably sufficient to ensure the production of a sGRB jet (III in scenario *b*). A potential death-trap for such highly relativistic outflows is the amount of entrained baryonic mass, which can severely limit their power (III in scenario *a*).

key question is whether there is significant observational support for the existence of low amounts of relativistic energy released during this event or whether the afterglow light curves are instead more consistent with a model in which GRB 170817a was a classical jetted sGRB viewed off-axis. Figure 4.1 presents here our selections for the energy transfer channels during merging neutron star binaries that we believe are responsible for the various entries in the inventory. Material dynamically stripped during the merger (denoted I in Figure 4.1) is ejected by tidal torques through the outer Lagrange point, removing energy and angular momentum and forming a large tidal tail (Kluźniak & Lee 1998; Rosswog 2005; Faber & Rasio 2012). This material is expected to undergo r-process nucleosynthesis and give rise to a red (quasi-thermal) kilonova (Li & Paczyński 1998a; Freiburghaus et al. 1999; Metzger et al. 2010b; Roberts et al. 2011a). The configuration after merger consists of a hyper massive neutron star (HMNS, one with more mass than a cold, non-rotating configuration could support) surrounded by an extended shock-heated envelope (Baumgarte et al. 2000; Duez et al. 2006). During this stage, various dissipation and transport mechanisms can give rise (Perego et al. 2014a; Siegel et al. 2014a) to strong winds (denoted II in Figure 4.1). These are thought to produce low-opacity (first-peak) r-process material, giving rise to a blue (quasi-thermal) kilonova (Kasen et al. 2013a, 2015a; Metzger & Zivancev 2016). The properties of the HMNS have a decisive outcome on whether or not a standard sGRB will be observed (Murguia-Berthier et al. 2014, 2017b; Piro et al. 2017). This is because even a tiny mass of baryons polluting the jet will severely limit the maximum attainable Lorentz factor and effective jet triggering might have to wait until after black hole collapse. In

scenario *a*, the wind emanating from the HMNS hampers the advancement of a relativistic jet, leading to a low luminosity event (Rosswog & Ramirez-Ruiz 2002, 2003; Nagakura et al. 2014; Just et al. 2016). In scenario *b* in Figure 4.1, the collapse to a black hole occurs promptly and a classical jetted sGRB is produced which we happen to view off-axis (such as Ramirez-Ruiz et al. 2005). Not only would a sGRB be detectable in both scenarios, followed by an afterglow, but there could also be additional extended emission at early stages caused by the reprocessing of this energy and its subsequent dissipation (Murguia-Berthier et al. 2014; Rezzolla & Kumar 2015). This could resemble the so called extended emission in sGRBs (Norris & Bonnell 2006). In the following sections, we examine these two possible interpretations and critically asses whether the electromagnetic observations of GW170817/SSS17a support the idea that it was an intrinsically weak, nearly isotropic explosion or either a classical sGRB, such as GRB 130603b (Fong et al. 2015), observed off-axis. An accurate assessment of the kinetic energy content in relativistic material requires detailed afterglow modeling.

4.4 A Low Luminosity sGRB

GW170817/SSS17a/GRB 170817a, or at least the γ-ray emission along our line of sight, was certainly feeble. The simplest interpretation might be that the γ-ray emission was deficient in all directions (scenario *a* in Figure 4.1), as in the case of low luminosity long GRBs associated with type Ic supernovae (Kaneko et al. 2007).

Such a weak burst, thousands to millions of times fainter than the inferred isotropic energies of sGRB, could belong to a separate population of weakly jetted, low

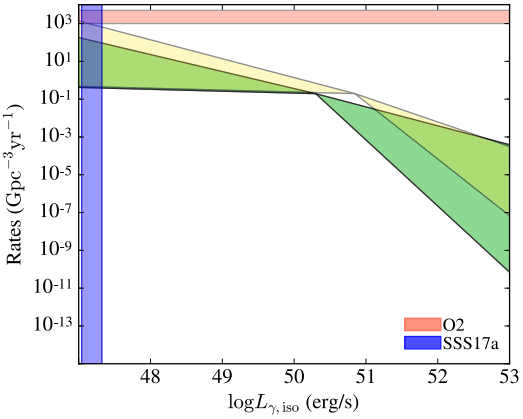

Figure 4.2: Shown are two luminosity functions taken from Guetta & Piran 2006. They are described by a broken power-law peak luminosity function with $L_* = 0.2{\times}10^{51}$ erg/s, $a = 0.6^{+0.3}_{-0.5}$, $b = 1.5^{+2}_{-0.5}$ (green) and $L_* = 0.7{\times}10^{51}$ erg/s, $a = 0.6^{+0.4}_{-0.5}$, $b = 2^{+1}_{-0.7}$ (yellow). If we assume a beaming correction factor of 27^{+158}_{-18} we find a merger rate that is broadly consistent with estimated O2 LIGO rates Abbott et al. 2016c and can accommodate the $L_{\gamma,\mathrm{iso}}$ measured by Goldstein et al. 2017 for GW170817/SSS17a/GRB 170817a.

luminosity events. We thus need to quantify the odds of detecting such an event as non-Euclidean number count statistics limit the fraction of bursts that can be observed from the local Universe (Bloom et al. 1998).

In Figure 4.2 we compare the properties of GRB 170817a (Goldstein et al. 2017) with the luminosity function of sGRBs as constrained from the peak flux distribution of BATSE events and the redshift and luminosity distributions of *Swift* events. The luminosity functions shown in Figure 4.2 have been derived (Guetta & Piran 2006) under the assumption that the sGRB rate follows a distribution of delay times that is consistent with those commonly used to describe the merging rate of double neutron star binaries (Champion et al. 2004; Behroozi et al. 2014; Shen et al. 2015).

If we assume a typical beaming correction of 27^{+158}_{-18} for sGRBs (Fong et al. 2015), we find an event rate that is broadly consistent with the O2 LIGO merger rate

estimated by Abbott et al. 2016c and can accommodate the $L_{\gamma,\rm iso}$ measured by Goldstein et al. 2017, under the assumption that GRB 170817a was similarly weak in all directions. BATSE was a benchmark experiment that produced a catalogue containing more than 2,000 GRBs (Paciesas et al. 1999). How many of these bursts could have been GW170817-like events? The observed number of sGRBs and the lack of excess events from the direction of the Virgo cluster suggests that only a tiny fraction ($\lesssim 0.05$) of these bursts can be like GW170817 within $\lesssim 40$ Mpc (Palmer et al. 2005).

4.4.1 Prompt Emission

The energy spectrum for GRB170817a is well described by a power law with an exponential cutoff at ≈ 185 keV (Goldstein et al. 2017). With no significant emission observed above 300 keV, GRB170817a is an example of the no high-energy bursts that compose 25% of the BATSE sample (Paciesas et al. 1999). Since GRB 170817a had a single-peaked light curve (Goldstein et al. 2017), the burst variability, $\delta t_{\rm var}$, is roughly given by $\delta t_{\rm var} \approx t_{90,\gamma} \approx 2 \pm 0.5$s (Abbott et al. 2017d).

A constraint on the size of the emitting region R_γ can be derived from the delay time $\delta t_{\rm gw} \approx t_{90,\gamma} \approx 2$s (Abbott et al. 2017d) observed between the arrival of the prompt γ-ray emission and the gravitational wave merger signal. If one assumes that the relativistic outflow, moving at $\Gamma = (1-\beta^2)^{-1/2}$, was triggered at merger, then

$$R_\gamma = c\delta t_{\rm gw}\beta(\beta-1)^{-1} \approx 2\Gamma^2 c\delta t_{\rm gw},$$

which is consistent with most studies aimed at understanding the nature of the γ-ray

dissipation in sGRBs (Nakar 2007; Kumar & Zhang 2015). Internal shocks dissipation, for example, is thought to occur at a radius $R_\iota \approx 2\Gamma^2 c\delta t_{\rm v}$ (Rees & Meszaros 1992). Since $\delta t_{\rm var} \approx \delta t_{\rm gw}$, it follows that $R_\iota \approx R_\gamma$.

4.4.2 The Afterglow Emission

If there was indeed this amount of relativistic energy we can then try to explain why we did not see the afterglow emission at early times by invoking a standard afterglow model. In such quasi-spherical case, the emission we expect should be below the ultraviolet, optical and infrared emission, which is dominated by heating from the decay of freshly synthesized r-process material (Coulter et al. 2017a; Drout et al. 2017; Kilpatrick et al. 2017; Shappee et al. 2017; Siebert et al. 2017).

The resulting light curves for a low energy spherical model are plotted against observations of SSS17a in Figure 4.3. As a point of comparison, we plot the light curves of GRB 130603b, whose afterglow properties are representative of classical sGRBs (Fong et al. 2015). The local emissivity is calculated using standard assumptions of synchrotron emission from relativistic electrons that are accelerated behind the shock (with a power-law distribution of energies wind index p) where the magnetic field and the accelerated electrons hold fractions ϵ_e and ϵ_B, respectively, of the internal energy. The model parameters are: $n = 0.08$ cm^{-3}; $E_{\rm K,iso} = 8 \times 10^{48}$ erg, $p = 2.1$, $\epsilon_B = 0.05$, $\epsilon_e = 0.05$ and the fraction of electrons that get accelerated is $\xi_N = 1$. We emphasize that the model parameters cannot be uniquely determined from the fit to the multi-wavelength observations, and other sets of parameters could provide an equally acceptable description. The X-ray emission is very sparsely sampled and thus provide

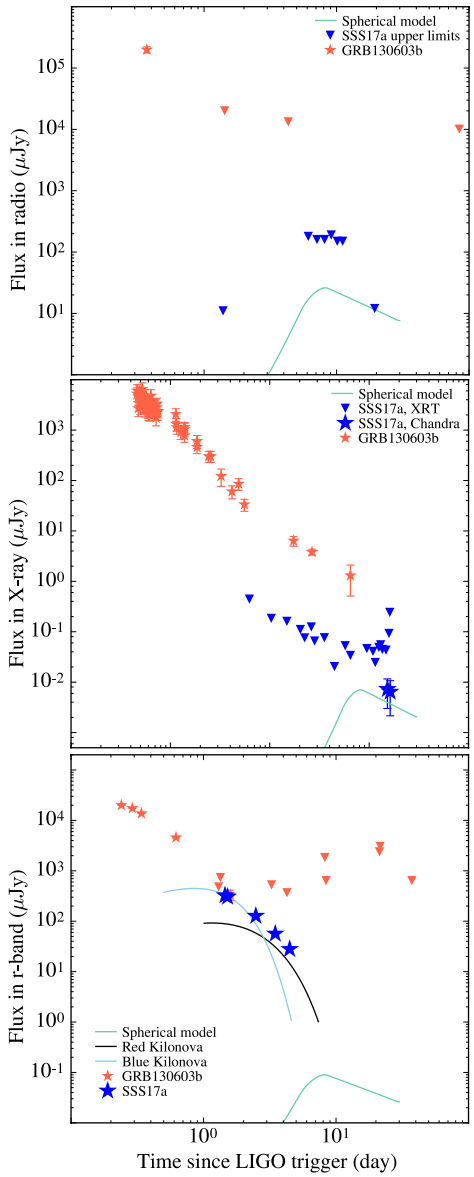

Figure 4.3: Afterglow emission from a spherical, low energy blast wave (scenario *a* in Figure 4.1) at optical (r-band), radio (6 GHz), and X-rays (7×10^{16} Hz). The afterglow light curves presented here are calculated using the blast wave models from Leventis et al. 2012. The microphysical parameters, the energetics and the properties of the external medium and burst energetics are given in the text. Also plotted is data from the One-Meter Two-Hemisphere collaboration: Coulter et al. 2017a; Drout et al. 2017; Kilpatrick et al. 2017; Shappee et al. 2017; Siebert et al. 2017 for the r-band, Haggard et al. 2017 for the X-rays, and Alexander et al. 2017, EuroVLBI team for the radio. The afterglow detections and upper-limits of the standard GRB 130603b are plotted for comparison (Fong et al. 2015).

only mild constraints on models on its own. However, when combined with the optical and radio limits, they provide a better handle on the model, thus significantly improving upon the constraints derived from the X-ray data alone. The reader is refer to Kumar & Zhang 2015 for a detailed description of our current understanding regarding afterglow physics and observational constraints.

The fact that X-ray emission was seen at $t = 15.2$ days, implies that $t_{\rm dec} \lesssim 15.2$ days, where $t_{\rm dec} = R_{\rm dec}/(2c\Gamma^2)$ and $R_{\rm dec} = (3E_{\rm k,iso}/4\pi n m_p c^2 \Gamma^2)^{1/3}$ are the observed time and radius at which the outflow decelerates appreciably (Piran 2004). In the model depicted in Figure 4.3, the initial Lorentz factor of the blast wave is chosen to be $\Gamma = 5.5$ in order for $t_{\rm dec} \lesssim 15.2$ days. In this case, $R_\gamma \approx 3.6 \times 10^{12} (\Gamma/5.5)^2 (\delta t_{\rm gw}/2{\rm s})$ cm.

Some points from should be emphasized here. The afterglow light curves provide a reasonable description of the sparsely sampled X-ray afterglow and are consistent with the lack of non-thermal radiation observed at radio and optical wavelengths. The optical emission is dominated by quasi-thermal emission, which also dominates the total radiated energy output (Drout et al. 2017). This is illustrated in Figure 4.3, where the best fit models for the kilonova emission at optical wavelengths are plotted. These models have been constructed using the simple formalism developed by Metzger 2017 and are tailored to match the values derived in Kilpatrick et al. 2017 using more sophisticated models. In this simple model, we contemplate ejecta of mass $m_{\rm ejecta}$ expanding at a velocity $v_{\rm ejecta}$, which is heated by the decay of freshly synthesized r-process material. Two different ingredients are assumed for the ejecta: a blue ($m_{\rm ejecta} = 0.025 M_\odot$ and $v_{\rm ejecta} = 0.3c$) and a red ($m_{\rm ejecta} = 0.035 M_\odot$ and $v_{\rm ejecta} = 0.15c$) component.

We use $\kappa_{\rm blue} = 0.08$ cm^{2}g^{-1} and $\kappa_{\rm red} = 5$ cm^{2}g^{-1} to describe the opacity of the blue (lanthanide free) and red (lanthanide rich) components, respectively (Barnes & Kasen 2013). This two component model, as argued in Kilpatrick et al. 2017, is in remarkable agreement with the wealth of observations our team has assembled at optical, ultraviolet and infrared wavelengths (Coulter et al. 2017a; Drout et al. 2017; Kilpatrick et al. 2017; Shappee et al. 2017; Siebert et al. 2017). What is more, observations at γ-rays, X-rays and radio wavelengths are consistent with GRB 170817a being an intrinsically weak, nearly isotropic explosion. Having said this, continuous monitoring of the source at X-ray and radio wavelengths could render this type of model unacceptable if the integrated energy is observed to increase.

4.5 An off-axis Model

Given that most sGRBs are collimated (Fong et al. 2015), their observed properties will unavoidably change depending on the angle $\theta_{\rm obs}$ (measured with respect to the jet axis) at which they are observed. If we make the standard assumption of a top-hat jet, the prompt and afterglow properties of the sGRB would be almost the same to all observers located within the initial jet aperture, denoted here as θ_0. At $\theta_{\rm obs} > \theta_0$, the jet emission is expected to decline precipitously (Granot et al. 2002).

4.5.1 Prompt Emission

In a typical sGRB (scenario *b* in Figure 4.1), the γ-rays we detect are concentrated into a cone of opening angle comparable to θ_0, provided that $\theta_0 > \Gamma^{-1}$. Thus, if

the jet is viewed at $\theta_{\rm obs} > \theta_0$ from the jet axis, the γ-ray luminosity will be drastically suppressed. For a jet with Γ, the typical peak photon energy $E_{\rm p}$ scales as (Ramirez-Ruiz et al. 2005)

$$E_{\rm p} \propto [\Gamma(\theta_{\rm obs} - \theta_0)]^{-2},$$

while

$$E_{\gamma,{\rm iso}} \propto [\Gamma(\theta_{\rm obs} - \theta_0)]^{-6}.$$

Figure 4.4 shows a sample of observed $E_{\rm p}$ and $E_{\gamma,{\rm iso}}$ for sGRBs together with the properties of GRB 170817a if it were viewed on-axis. In order to generate the on-axis conditions we have used $\theta_{\rm obs} = 1.5\theta_0$ and $\theta_0 = 0.2$, which we inferred from a fit to the afterglow emission (see Section 4.5.2 for details), and have assumed $\Gamma = 50$. These values are compatible with those observed in (and in some cases derived for) sGRBs (Gehrels et al. 2009; Berger 2014; Fong et al. 2015). We thus consider $\Gamma = 50$ and the inferred on-axis values of $E_{\rm p} \approx 4$ MeV and $E_{\gamma,{\rm iso}} \approx 7 \times 10^{50}$ erg to be reasonable for conditions expected at the edge of the jet (Ramirez-Ruiz et al. 2005).

For $\theta_{\rm obs} > \theta_0$, one expects some significant decrease in the variability of the prompt emission. This is because the duration of an individual pulse in the light curve scales as $\delta t_{\rm var} \propto [\Gamma(\theta_{\rm obs} - \theta_0)]^2$. Since the distance between neighboring pulses is typically comparable to the width of an individual pulse, then a sizable increase in $\delta t_{\rm v}$ could cause significant overlap between pulses and, as a result, the variability would be washed out.

The total duration of the event could also increase significantly for large view-

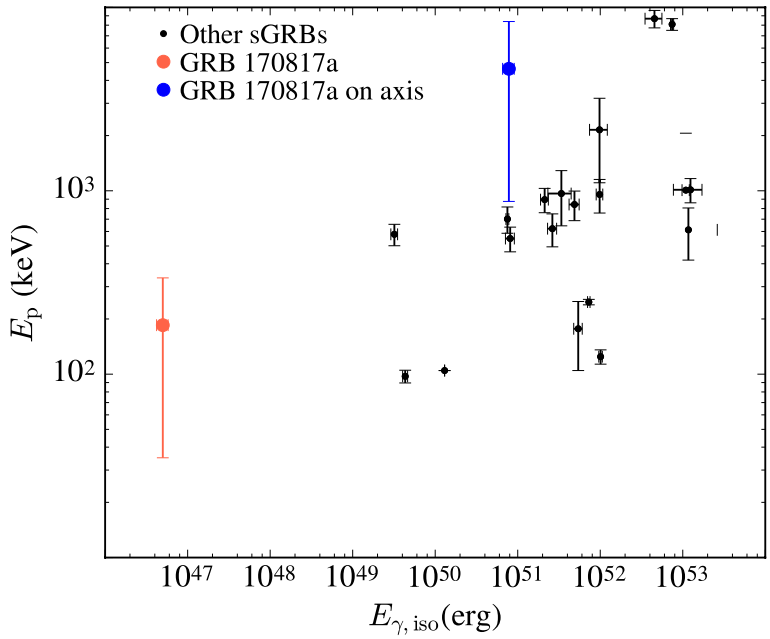

Figure 4.4: The location of GRB 170817a in the $E_{\rm p}$ and $E_{\gamma,\rm iso}$ plane, from Savchenko et al. 2017; Goldstein et al. 2017. Also shown is the location if GRB 170817a were on-axis under the assumption of a misaligned, sharp-edged jet. This assumes a Lorentz factor of $\Gamma \approx 50$ and $\Gamma(\theta_{\rm obs} - \theta_0) \approx 5$ (Section 4.5.2). The data for the other sGRBs are taken from Tsutsui et al. 2013 and D'Avanzo et al. 2014.

ing angles when $[\Gamma(\theta_{\rm obs} - \theta_0)]^2 \gtrsim (t_{90,\gamma}/\delta t_{\rm var})$, where the total observed duration of the burst ($t_{90,\gamma}$) and individual pulse variability ($\delta t_{\rm var}$) are measured here on-axis. For most sGRBs, $(t_{90,\gamma}/\delta t_{\rm var}) \approx 10 - 10^2$ (Gehrels et al. 2009), which implies that for $[\Gamma(\theta_{\rm obs} - \theta_0)]^2 < t_{90,\gamma}/\delta t_{\rm var} \sim 10 - 10^2$ the total duration of the burst when observed off-axis should not increase significantly. The variability of the burst, when observed off-axis on the other hand, is expected to be smeared out.

Based on the model parameters estimated here, we thus expect GRB170817a to have been significantly more luminous, have a shorter duration, be more variable and have a much harder spectrum for observers located within $\theta_{\rm obs} \lesssim \theta_0$. This might explain why GRB170817a was observed to be somewhat less variable than typical sGRBs. As argued in Section 4.4.1, the observed time delay between the arrival of the gravitational wave signal and the prompt γ-ray emission can be used to place constraints on the size of the emitting region although the degree of pulse and light curve smearing in this scenario complicates the calculation.

4.5.2 Afterglow Emission

An observer at $\theta_{\rm obs} > \theta_0$ observes a rising afterglow light curve at early times (Granot et al. 2002). The afterglow light curve will be observed to peak when Γ, which is decreasing with time, reaches a value $\approx (\theta_{\rm obs} - \theta_0)^{-1}$ and soon after will approach that seen by an on-axis observer. This can be discerned by comparing the curves for $\theta_{\rm obs} = \theta_0$ and $\theta_{\rm obs} = 2\theta_0$ in Figure 4.5. The observations of GRB 170817a/SSS17a can be accommodated if $\theta_{\rm obs} \approx 1.5\theta_0$ for $\theta_0 = 0.2$. That is, our line of sight happened to be a few degrees from a sharp-edged typical sGRB jet. The constraints inflicted by the

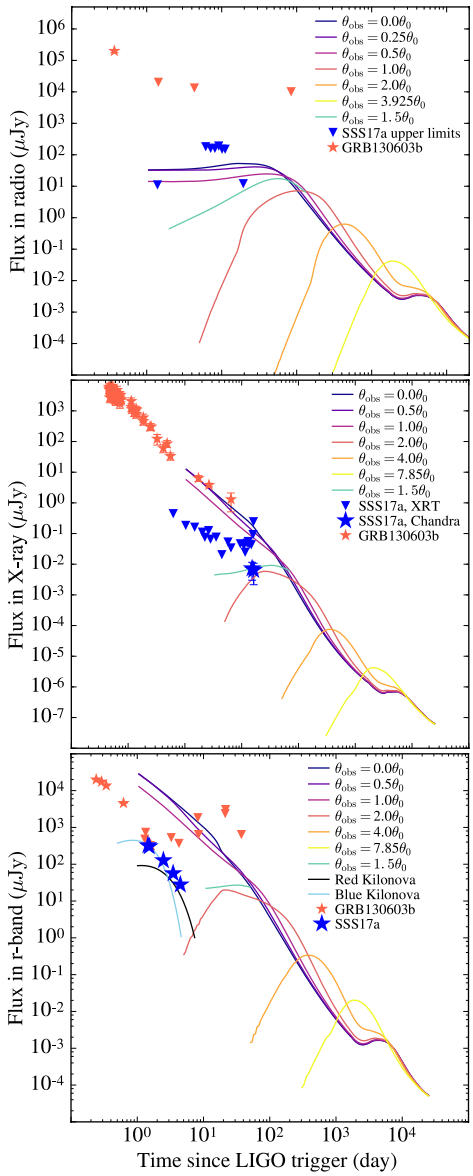

Figure 4.5: Afterglow emission from a standard off-axis jet (scenario *b* in Figure 4.1). Light curves are calculated for various viewing angles $\theta_{\rm obs}$ at optical (r-band), radio (6 GHz), and X-rays (7×10^{16} Hz) for a sGRB with standard parameters: $n = 0.3$ cm^{-3}, $E_{\rm K,iso} = 2.5 \times 10^{51}$ erg, $p = 2.8$, $\epsilon_B = 0.002$, $\epsilon_e = 0.02$ and $\xi_N = 1$. The curves presented here are calculated using the models from van Eerten & MacFadyen (2011). Also plotted is the same data and kilonova models shown in Figure 4.3. The data for GRB 170817a/SSS17a can be reasonably fit by a standard sGRB seen seen at $\theta_{\rm obs} = 1.5\theta_0$, where θ_0=0.2. The on axis model is broadly compatible with the properties of typical sGRBs as illustrated by the comparison with GRB 130603b (Fong et al. 2015).

properties of the afterglow emission thus support the idea that GRB 170817a/SSS17a was a standard sGRB jet seen off-axis. The on-axis model $\theta_{\rm obs} \lesssim \theta_0$ in this case provides a reasonable description of the broad afterglow properties of GRB 130603b (Fong et al. 2015), which by all accounts is representative of the sGRB population. The isotropic kinetic energy of the jet, when viewed on axis, would be $E_{\rm K,iso} = 2.5 \times 10^{51}$ erg, which can explain (for reasonable dissipation efficiencies) $E_{\gamma,\rm iso}(\theta_{\rm obs} \lesssim \theta_0)$ in Figure 4.4. The simple off-axis fit to the afterglow observations does not, however, uniquely determine the model parameters. Some model constraints are, however, rather robust. Most notably within the framework presented here, if the jet axis had been closer to the observer's direction, the intensity of the optical and infrared afterglow might have prevented us from uncovering the kilonova signal. This can be clearly seen by comparing the properties of SSS17a with those of GRB 130603b. This implies that the edge of the jet must be sufficiently sharp, so that the emission at early times would be dominated by the core of the jet, rather than by material along the line of sight that might produce bright radio, optical and X-ray emission.

4.6 Conclusions and Prospects

The recent discovery of GRB 170817a/SSS17a associated with GW170817 (Coulter et al. 2017a; Goldstein et al. 2017) has made it possible to strengthen the case for binary neutron star mergers as the main progenitors of sGRBs (Piran 2004; Lee & Ramirez-Ruiz 2007a; Nakar 2007; Gehrels et al. 2009; Rezzolla et al. 2011; Berger 2014). While the isotropic energy emitted in gravitational waves is of the order of a

fraction of a solar rest mass $\gtrsim 0.025 M_{\odot} c^2 \approx 4.5 \times 10^{52}$ erg , the total integrated electromagnetic emission is estimated here to be drastically lower $\approx 5 \times 10^{48}$ erg (Section 4.3) and was dominated by the quasi-thermal emission seen at infrared, optical and ultraviolet wavelengths. By modeling this emission in great detail, Kilpatrick et al. 2017 predicts the kinetic ejecta content at sub-relativistic velocities ($v_{\rm ejecta} \approx 0.1c$) to be of the order of a few times 10^{51} erg.

The faint nature of GRB 170817a can be used to argue for the existence of at least two different possibilities for the nature of the sGRB event associated with GW170817, on the basis of different amounts of relativistic energy released during the initial explosion. In this Letter, we have examined two concrete alternatives. The first one is based on the premise that GRB 170817a was an intrinsically weak, nearly isotropic explosion and we conclude that current observations are also consistent with this idea (Section 4.4). In this scenario, the kinetic energy content at mildly relativistic velocities $\Gamma \approx 5$ is estimated to be $\approx 10^{49}$ erg. The second alternative is based on the hypothesis that GRB 170817a was an ordinary GRB observed off-axis, and in this case we conclude that current available data is consistent with an off-axis model in which GRB 170817a was a much more powerful event seen at an angle of about 1.5 times the opening angle of the jet (Section 4.5). The kinetic energy content at relativistic velocities $\Gamma \approx 10^2$ is thus estimated to be $\approx 10^{50}$ erg after correcting for beaming. Detailed X-ray and radio follow-up observations and polarimetry of GRB 170817a/SSS17a should provide us with stringent constraints on the jet geometry and energetics, as both models make very different predictions. [3] The off-axis model, for example, will be preferred if the

[3]It should be noted that there is a disagreement about the possible detection of a radio afterglow at

X-ray and radio fluxes are observed to increase.

The progenitors of sGRBs have been until now essentially masked by afterglow emission, which is largely featureless synchrotron emission (Nakar 2007). The detection of kilonova emission has clearly established the potential of electromagnetic signatures to shed light on the properties of the ejecta and its composition after merger (Kilpatrick et al. 2017). As we have described, our rationalization of the principal post-merger physical considerations combines some generally accepted principles with some more speculative ingredients (Figure 4.1). When confronted with observations, it seems to accommodate the gross properties of the electromagnetic radiation (Figures 4.3 and 4.5), in addition to the incalculable value of the information that will be gathered from the concurrent gravitational event will provide us with the exciting opportunity to study and test new regimes of physics.

t =17-19 days (GROWTH 2017; Alexander et al. 2017). If confirmed both models presented here can be slightly modified to provide a reasonable description of the data at this specific epoch.

Chapter 5

GW170817: how the remnant affects the jet structure

5.1 Chapter Abstract

The first neutron star binary merger detected in gravitational waves, GW170817 and the subsequent detection of its emission across the electromagnetic spectrum showed that these systems are viable progenitors of short γ-ray bursts (sGRB). The afterglow signal of GW170817 has been found to be consistent with a structured GRB jet seen off-axis, requiring significant amounts of relativistic material at large angles. This trait can be attributed to the interaction of the relativistic jet with the external wind medium. Here we perform numerical simulations of relativistic jets interacting with realistic wind environments in order to explore how the properties of the wind and central engine affect the structure of successful jets. We find that the angular energy distribution of the

jet depends primarily on the ratio between the lifetime of the jet and the time it takes the merger remnant to collapse. We make use of these simulations to constrain the time it took for the merger remnant in GW170817 to collapse into a black hole based on the angular structure of the jet as inferred from afterglow observations. We conclude that the lifetime of the merger remnant in GW170817 was $\approx 1 - 1.7$s, which, after collapse, triggered the formation of the jet.

5.2 Introduction

The gravitational wave event GW170817 (Abbott et al. 2017c), that was accompanied by the detection of emission across the electromagnetic spectrum (Coulter et al. 2017a; Abbott et al. 2017d), demonstrated that neutron star binary mergers are the sources of short $\gamma-$ray bursts (sGRBs; Eichler et al. 1989; Narayan et al. 1992), or at least a subset of them.

From the unusually faint nature of GRB 170817A it was initially argued that this event belonged to a class of intrinsically sub-energetic sGRBs (Margutti et al. 2018), but as more is being learned about GRB 170817A, the more it appears like the afterglow emission is instead consistent with the neutron star merger having triggered a typical, powerful sGRB seen at an angle of about a few times the opening angle of the central jet (Lazzati et al. 2017; Murguia-Berthier et al. 2017c; Duffell et al. 2018; Lamb et al. 2018; Mooley et al. 2018a; Wu & MacFadyen 2018; Mooley et al. 2018b; Lamb et al. 2019).

A question that has remained largely unanswered so far is what determined

the atypical structure of the jet in GRB 170817A, which is required not to have sharp edges but wings of lower kinetic energy and Lorentz factors that extend to large angles (Lazzati et al. 2017; Duffell et al. 2018; Bromberg et al. 2018; Granot et al. 2018; Lamb & Kobayashi 2018; Xie et al. 2018; Kathirgamaraju et al. 2018; van Eerten et al. 2018; Gill et al. 2019a; Lamb et al. 2019; Lazzati & Perna 2019; Beniamini et al. 2020; Lazzati et al. 2020; Ryan et al. 2020; Nakar & Piran 2020). This in turn might be attributed to the interaction of the jet with a dense surrounding gas distribution, quite possibly the wind emanating from the merger remnant.

A trait of the jet-wind interaction is that there can be an exchange of linear momentum with the neighboring wind, even if there is minimal exchange of baryons (Lee & Ramirez-Ruiz 2007a). As a result, the jet itself is then likely to develop a velocity profile so that different portions move with different Lorentz factors (Aloy et al. 2005; Rosswog & Ramirez-Ruiz 2002). This implies that an observer could infer a value for the Lorentz factor that depends upon the inclination of the line of sight to the jet axis. In this case, the early afterglow emission of GRB 170817A would be naturally produced by the deceleration of the lower Lorentz factor material moving along our line of sight (Rosswog et al. 2003; Lamb & Kobayashi 2018).

We already know that winds are a prominent feature of neutron star merger remnants and are accompanied by prodigious mass loss (Rosswog & Ramirez-Ruiz 2002, 2003; Lee & Ramirez-Ruiz 2007a; Lee et al. 2009; Perego et al. 2014a; Nedora et al. 2020). This is not on the face of it the most advantageous environment to produce a baryon-starved jet. Studies of sGRB jets (Eichler et al. 1989; Narayan et al. 1992; Lee

& Ramirez-Ruiz 2007a) are thus increasingly invoking the collapse of the remnant to a black hole (e.g. Lee et al. 2005a), which neatly avoids the problem of catastrophic mass pollution close to the jet creation region, and allows the terminal jet Lorentz factors to be large. There are alternatives to the collapse of the remnant to a BH in which a long-lived remnant can form a jet (Mösta et al. 2020), although the aforementioned risks of baryon population could severely limit the jet's Lorentz factor. These issues motivate our study of the interaction between the jet and the pre-collapse wind through which the jet is expected to propagate. This jet-outflow interaction could turn out to be key for interpreting the observed properties of GRB 170817A.

The pre-burst gas distribution depends on how the binary neutron star merger loses mass. As the binary coalesces, various mechanisms can transport angular momentum and dissipate energy in the newly formed remnant (Baiotti et al. 2008), giving rise to significant mass-loss (Lee & Ramirez-Ruiz 2007a). One important transport mechanism is the neutrino-driven wind (NDW) (Rosswog & Ramirez-Ruiz 2003; Dessart et al. 2009; Perego et al. 2014a), as copious amounts of neutrinos are created in the merger remnant. The high flux of neutrinos will interact with matter in and around the merger remnant, driving a baryon loaded wind. Another important mechanism is energy and angular momentum transport mediated by magnetic fields. Even an initial weak field can destabilize the merger remnant via the so called magneto-rotational instability (e.g. Ruiz et al. 2019). Magnetic instabilities inside the merger remnant can thus drive a powerful baryon-loaded wind (Siegel et al. 2014a; Ciolfi et al. 2017; Ciolfi 2020).

This merger remnant is assumed to be unstable and its subsequent collapse to

a black hole is assumed to trigger a relativistic jet (Rezzolla et al. 2011; McKinney et al. 2012, 2014; Sądowski et al. 2015; Ruiz et al. 2016; van Eerten et al. 2018; Qian et al. 2018; Kathirgamaraju et al. 2019; Ruiz et al. 2019). This is thought to be the case for GRB 170817, since a long-lived remnant is difficult to reconcile with observations (e.g. Ciolfi 2020; Ciolfi et al. 2019). In this case, the jet will then unavoidably interact with the pre-collapse winds[4].

The interaction of the wind has a decisive effect in shaping the jet (Nagakura et al. 2014; Murguia-Berthier et al. 2014; Duffell et al. 2015; Murguia-Berthier et al. 2017b; Duffell et al. 2018; Lazzati et al. 2018; Geng et al. 2019; Hamidani & Ioka 2020; Gottlieb et al. 2020b,a; Hamidani et al. 2020). Additionally, there are instances in which the wind can be dense enough to become a death trap for the jet, choking the outflow and rendering sGRB production unsuccessful. Therefore it is important to understand how the properties of the wind and central engine affect the structure of the jet. The wind is driven by the merger remnant in this case while the jet is triggered by the newly formed BH and accretion disk. A key property of the binary neutron star merger is the time it takes for the remnant to collapse into a black hole, which is directly linked to the lifetime of the wind. Thus, by understanding how the interaction with the wind can alter the jet structure, one can constrain the lifetime of this remnant.

In this paper we perform special relativistic simulations to study how the jet structure is affected by the neutrino driven wind and the magnetized disk outflow. We also explore how the time delay between collapse and jet triggering affects the structure

[4] As the jet continues to plough ahead of the wind, it sweeps up an increasing amount of surrounding gas, made up of interstellar medium or material which was previously ejected by the progenitor system (such as, e.g., a pulsar-wind; Ramirez-Ruiz et al. 2019). This sets a characteristic deceleration length at which the the afterglow emission becomes relevant.

of the jet. We use these simulations to set a limit on the delay time of GW170817 based on the angular structure of the jet that is inferred from afterglow observations.

5.3 Jet and wind interaction

5.3.1 Numerical method and setup

Our simulations follow the setup described in Murguia-Berthier et al. (2014, 2017b). They are performed in 2D axisymmetric coordinates using *Mezcal*, an adaptive mesh refinement code that solves the equations of special relativistic hydrodynamics. A description of the code and a number of benchmark tests can be found in De Colle et al. (2012a,b).

The setup begins with the injection of a wind, lasting for a time $t_{\rm w}$. This $t_{\rm w}$ is directly related to the time it takes the merger remnant to collapse to a black hole. After that time, the density of the wind is assumed to decrease as $t^{-5/3}$, and a jet is introduced. Motivated by GRMHD simulations (McKinney et al. 2012; Sądowski et al. 2015; Ruiz et al. 2016, 2019), the jet is assumed to initially have a top-hat structure characterized by a half-opening angle θ_0, a luminosity L_j and a Lorentz factor of $\Gamma = 10$ that are constant with angle[5]. The central engine powers the jet for a time $t_{\rm j}$. Table 5.1 presents the simulation parameters of all the calculations we performed in this study.

[5]Numerical simulations of jets launched from the central engine with a luminosity and Lorentz factor varying with the polar angle θ are discussed in (Urrutia et al. 2020).

Type of wind	t_w (s)	$t_j(s)$	$L_{\rm j}/10^{50}$ (erg/s)	$\dot{M}_{\rm w}/10^{-3}$ ($M_\odot$/s)	θ_0 (°)	Successful sGRB?
SW	0.5	0.5	1	1	10	Yes
SW	1	0.5	1	1	10	Mild
SW	0.5	1	1	1	10	Yes
SW	1	1	1	1	10	Yes
SW	0.5	0.5	1	10	10	No
SW	0.5	1	1	10	10	No
SW	1	0.5	1	10	10	No
SW	0.5	0.5	10	10	10	Yes
SW	0.3	0.5	10	10	10	Yes
SW	1	0.5	10	10	10	Mild
SW	0.5	1	10	10	10	Yes
SW	0.3	1	1	5	14	Yes
SW	0.7	1	1	1	10	Yes
NDW	0.5	0.5	1	1	10	Yes
NDW	0.5	1	1	1	10	Yes
NDW	1	0.5	1	1	10	Mild
NDW	1	1	1	1	10	Yes
NDW	0.5	0.5	1	3	10	Yes
NDW	0.5	0.5	5	3	10	Yes
NDW	0.5	0.5	1	10	10	No
NDW	0.5	1	1	10	10	No
NDW	1	0.5	1	10	10	No
NDW	1	1	1	10	10	No
NDW	0.5	0.5	10	10	10	Yes
NDW	0.5	1	10	10	10	Yes
NDW	1	0.5	10	10	10	Mild
NDW	1	1	10	10	10	Yes
NDW	0.3	1	1	1	10	Yes
NDW	0.3	1	10	10	10	Yes
NDW	0.3	1	1	5	14	Yes
MW	0.5	0.5	1	1	10	Yes
MW	0.5	1	1	1	10	Yes
MW	1	0.5	1	1	10	No
MW	1	1	1	1	10	Yes

Table 5.1: List of models and the initial conditions of our 2d spherical simulations. Here $t_{\rm w}$ corresponds to the time the wind is active, which is related to the delay time between the merger and the collapse to a BH. $t_{\rm j}$ is the time the central engine is active. $L_{\rm j}$ corresponds to the isotropic jet luminosity. $\dot{M}_{\rm w}$ corresponds to the mass loss rate in the polar region of the wind. θ_0 is the initial half-opening angle of the jet. All of our simulations have an inner radius of 1×10^9cm and an outer radius of 6×10^{10}cm. We use an adaptive grid of size $l_{\rm r} = 6 \times 10^{10}$ cm and $l_\theta = \pi/2$ with 100×40 initial cells and five levels of refinement resulting in a maximum resolution of 3.75×10^7cm. We also use common values for the velocity of the wind $v_{\rm w} = 0.3$ and the jet Lorentz factor $\Gamma_{\rm j} = 10$. For the density profile of the wind we use a spherical wind (SW), a neutrino-driven wind (NDW) and a magnetized wind (MW).

5.3.2 The wind medium in the pre-collapse, merged remnant

Three different wind prescriptions are simulated, which have different angular structures. The first is a constant uniform spherical wind (Murguia-Berthier et al. 2014). The second is a non-spherical latitudinal distribution in density and velocity (Murguia-Berthier et al. 2017b), whose distribution is based on the global simulations of Perego et al. (2014a), accurately representing the neutrino-driven wind from the merger remnant. Additionally, we have included a density profile of a magnetized wind outflow based on the simulations by Janiuk (2019), where the author performs general relativistic magneto-hydrodynamical simulations[6]. The density profiles in both cases are similar, they are denser in the equator and progressively lighter in the polar region. The density as a function of angle is obtained by averaging the latitudinal profiles at the end of the simulations (Perego et al. 2014a; Janiuk 2019). The density of the wind is given by

$$\rho_{\rm w}(\theta) = \frac{\dot{M}(\theta)}{4\pi r^2 v_{\rm w}}, \tag{5.1}$$

where $\dot{M}_{\rm w}(\theta)$ is the mass loss rate, r is the radial coordinate, θ is the angular component, and $v_{\rm w}$ is the velocity of the wind, which is assumed to be constant. For comparison, we plot the angular distributions of density in the three different winds in Figure 5.1. The ratio of the density in the polar region ($\theta = 0°$) and the equator ($\theta = 90°$) is $\rho_{\rm eq}/\rho_{\rm pl} \approx 10^2$ for the NDW and $\rho_{\rm eq}/\rho_{\rm pl} \approx 1.5 \times 10^3$ for the magnetized outflow. We

[6]We note that although the calculations of Janiuk (2019) were performed for a 3 $M_\odot$ BH surrounded by 0.1 $M_\odot$ accretion disk, the resultant angular profiles are very similar to those by Siegel et al. (2014a) for a merger remnant. These wind profiles have the advantage that they have been calculated over many more dynamical times, due to the relative numerical simplicity, and thus better resemble a steady state wind solution.

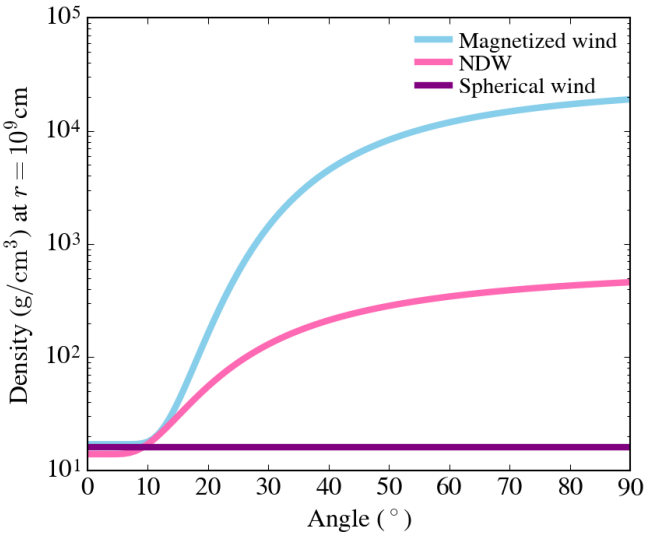

Figure 5.1: The angular structure of the density profiles used in our simulations. The density is plotted at $r = 10^9$cm, the inner boundary of the simulations. The three different wind prescriptions are plotted and have a mass loss rate (at the polar region) of $\dot{M}_{\rm w}(\theta = 0^\circ) = 10^{-3} M_\odot/{\rm s}$. The density profiles are derived from global simulations by Perego et al. (2014a) for the NDW, and by Janiuk (2019) for the magnetized wind. In this figure the angular radial profiles are derived by fitting smooth functional forms to the numerical profiles.

use two different global values for the mass loss rate, as prescribed in the polar region: $10^{-3} M_\odot/{\rm s}$ and $10^{-2} M_\odot/{\rm s}$. This range is motivated by the range of values seen in magnetically-driven and neutrino driven wind calculations (Perego et al. 2014a; Siegel et al. 2014a; Shibata et al. 2017; Fujibayashi et al. 2018; Nathanail et al. 2019; Geng et al. 2019).

5.3.3 Evolution of the jet

Initially, the jet is unable to move the wind material at a speed comparable to its own and thus is decelerated. As the jet propagates in the wind a bow shock runs ahead of it, which both heats material and causes it to expand sideways (Ramirez-Ruiz

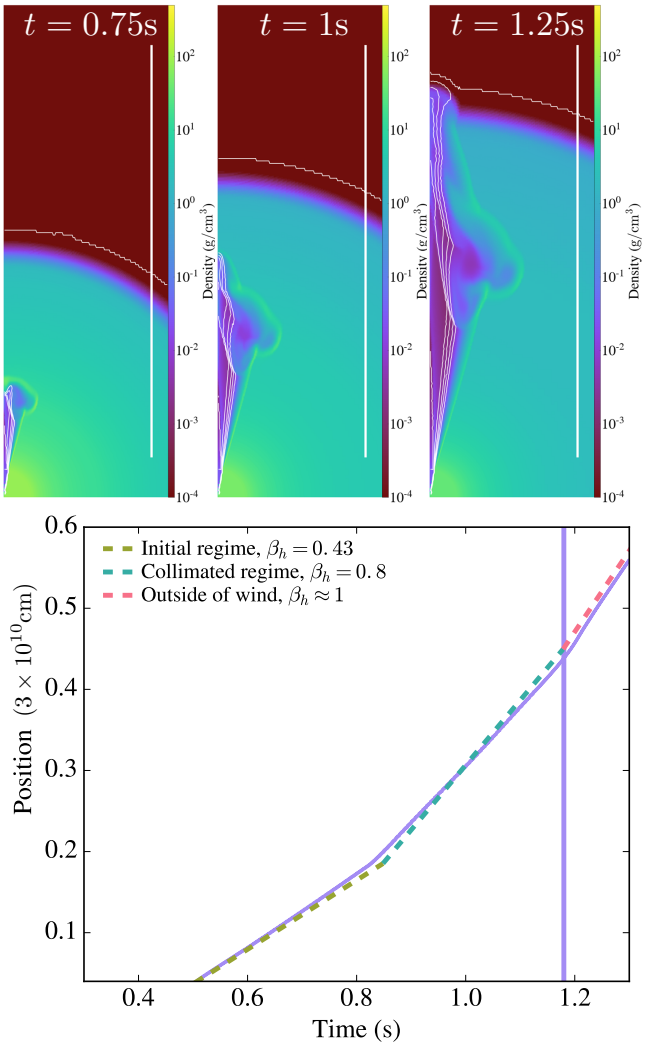

Figure 5.2: *Top* panels: Density snapshots of the jet interacting with a spherical wind with $\dot{M}_{\rm w} = 10^{-2} M_\odot$/s. The jet has a luminosity of $L_{\rm j} = 10^{51}$erg/s, $\theta_0 = 10^\circ$ and $t_{\rm j} = 1$s, while the wind is active for $t_{\rm w} = 0.5$s before collapse. In this and all other simulations the wind starts at $t = 0$ and is active for a time $t_{\rm w}$. After this, a jet is triggered, whose duration is $t_{\rm j}$. The panels show the evolution of the jet at three different times and the white contours are lines of constant Lorentz factor. Shown in all cases is a 1.5×10^{10} cm scale bar. *Bottom* panel: The temporal evolution of the position of the head of the jet (purple). Plotted in dashed lines are different constant velocity regimes as estimated by the analytical formalism: initial expansion at constant $\tilde{L}$, the recollimation region with varying $\tilde{L}$ and the free expansion phase. The vertical line gives the time at which the jet breaks free from the wind region.

et al. 2002; Bromberg et al. 2011; Salafia et al. 2020). The parameter that controls the evolution of the jet interacting with the wind is (Bromberg et al. 2011; Murguia-Berthier et al. 2017b):

$$\tilde{L} = \frac{\rho_{\rm j} h_{\rm j} \Gamma_{\rm j}^2}{\rho_{\rm w} \Gamma_{\rm w}^2}, \tag{5.2}$$

where ρ is the density, h is the enthalpy, Γ is the Lorentz factor and the subscripts j, w refer to the jet and the wind, respectively. At a given time, the jet will have evacuated a channel out to some location where it impinges on the pre-collapse wind, at a working surface advancing at velocity $\beta_{\rm h}$. We balance the momentum fluxes at the working surface to obtain (Begelman & Cioffi 1989; Bromberg et al. 2011; Murguia-Berthier et al. 2017b)

$$\beta_{\rm h} = \frac{\beta_{\rm j} + \beta_{\rm w} \tilde{L}^{-1/2}}{1 + \tilde{L}^{-1/2}}, \tag{5.3}$$

where $\beta_j = v_{\rm j}/c$ is the initial velocity of the jet, as determined by Γ. During propagation in the wind, the head of the jet will initially expand at a constant velocity. This is because $\rho_{\rm j}/\rho_{\rm w}$ is independent of r, so that $\tilde{L}$ remains unchanged (Equation 5.2). This can be seen in the expansion of the head of the jet during the first 0.75s (shown in the bottom panel of Figure 5.2), which expands at a constant velocity. The surplus energy during this time is deposited within a cocoon surrounding the jet. As the pressure of the cocoon cavity increases, a recollimation shock is formed which minimizes the cross-sectional area of the jet (Figure 5.2). In this region, $\tilde{L}$ depends on the pressure build

up within the cocoon region ($P_{\rm c}$; Bromberg et al. 2011)

$$\tilde{L} = \frac{4P_{\rm c}}{\theta_0^2 \rho_{\rm w} c^2}. \tag{5.4}$$

This transition is clearly seen after 0.75s in the evolution of the jet's head plotted in Figure 5.2.

In order for the jet to be successful, the central engine needs to remain active when the jet breaks out of the wind. By considering the time at which the head of the jet reaches the outer edge of the wind, the condition for a successful SGRB jet can be written as:

$$\beta_{\rm h} > \beta_{\rm h,c} = \beta_{\rm w} \left(1 + \frac{t_{\rm w}}{t_{\rm j}}\right) , \tag{5.5}$$

where $\beta_{\rm w} = v_{\rm w}/c$. This condition is clearly satisfied in the simulation shown in Figure 5.2. At the time the jet head breaks out from the wind ($t \approx 1.2$s), we required $\beta_{\rm h} > \beta_{\rm h,c} \approx 0.45$, which is clearly satisfied and the jet remains active. In Section 5.3.4 we investigate the applicability of condition 5.5 for both spherical and non-spherical winds.

5.3.4 Winds, jet dynamics and successful jets

The shocks responsible for producing a sGRB must arise after the relativistic jet has broken free from the pre-collapse wind. The majority of compact mergers, with the exception of those involving a black hole, will not collapse immediately and a dense wind will thus remain to impede the advance of the jet. As stated by the condition 5.5, a sGRB is likely to be produced if the jet triggered by the post-collapse accretion

maintains its power for longer than it takes the jet to reach the edge of the wind. If this is not the case, as shown in the top panel in Figure 5.3, the jet will be choked. On the other hand, if the jet continues to be active and emerges from the wind, the sudden and drastic density drop at the outer edges allows the jet head to accelerate to velocities close to the speed of light[7], as illustrated in the middle and bottom panels in Figure 5.3. In the middle panel $\beta_{\rm h} \approx \beta_{\rm h,c}$, while in the bottom panel $\beta_{\rm h} \gg \beta_{\rm h,c}$.

The condition $\beta_{\rm h} > \beta_{\rm h,c}$ can be used to derive the critical power needed for a jet to be successful, as argued by Murguia-Berthier et al. (2017b). This critical luminosity estimate is shown in Figure 5.4 in the context of our jet simulations with varying $t_{\rm w}/t_{\rm j}$ and expanding in a medium with $\dot{M}_{\rm w} = 10^{-2} M_{\odot}/{\rm s}$. The dots in Figure 5.4 correspond to successful jets and the crosses are choked jets. As expected, the ratio $t_{\rm j}/t_{\rm w}$ is critical in determining successful breakout of the expanding jet.

The critical condition for the minimum jet power in Figure 5.4 has been derived assuming that $\tilde{L}$ is constant. This is generally a valid assumption when the jet expands in a $1/r^2$ wind medium and experiences little recollimation. The applicability of this approximation can be seen by contrasting the evolution of the two jets depicted in the bottom panel in Figure 5.4. One of them (solid line) experiences significant recollimation before reaching the edge of the jet, while the other one (dashed line) escapes before the cocoon pressure is able to significantly alter the jet's initial structure. We note that although both jets are successful, the condition plotted in the top panel of Figure 5.4 places the simulation with $t_{\rm w}/t_{\rm j} = 1$ (solid line in the bottom panel) below the line. In

[7] In the case depicted in the bottom panel of Figure 5.2, the final Lorentz factor is approximately 9, which is 90% of the initial Lorentz factor.

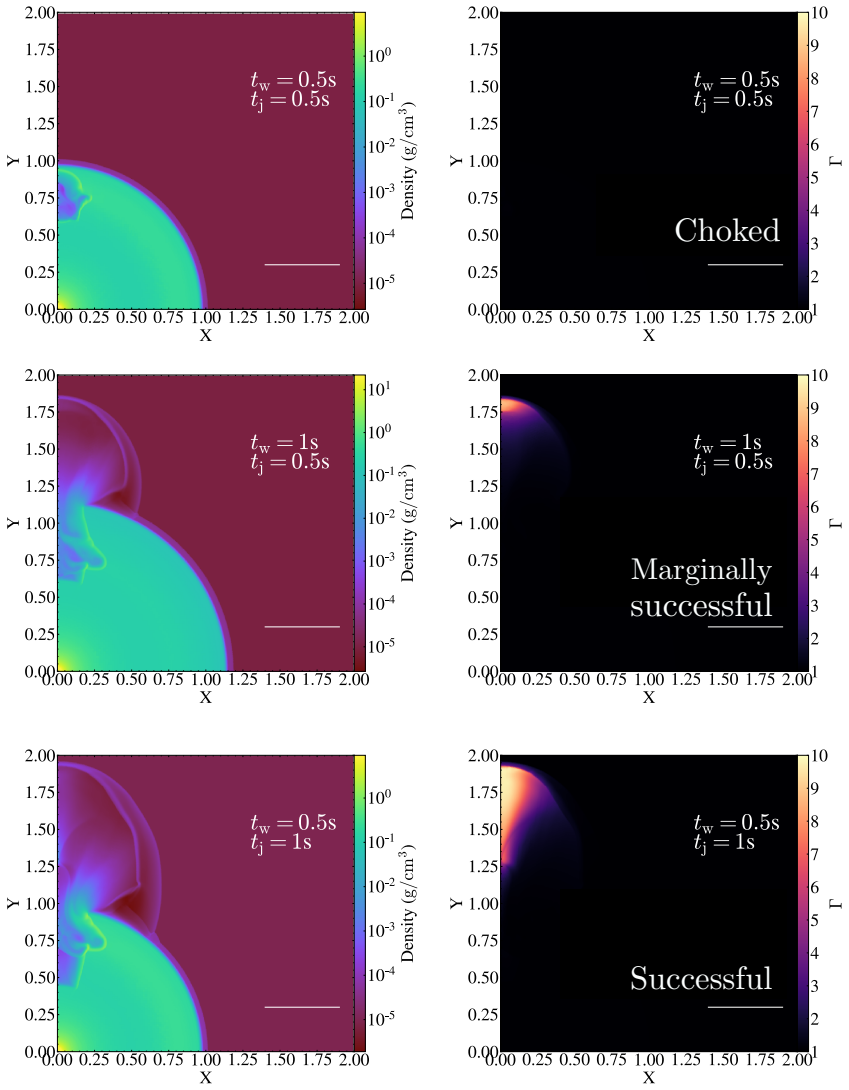

Figure 5.3: Simulations showing how the expansion of the jet is affected by the properties of the wind through which it propagates and in particular, its pre-collapse duration, $t_{\rm w}$. Three illustrative cases are depicted of simulations of jets propagating within a spherical wind with a mass loss rate of $\dot{M}_{\rm w} = 10^{-2} M_\odot$/s and $v_{\rm w} = 0.3c$. The left panels show the density while right panels show the Lorentz factor. The top and bottom panels correspond to the evolution of the jet at a time of 2.75s, while the middle panel is a snapshot at a time of 3.25s. Shown in all cases is a 1.5×10^{10} cm scale bar. Top Panel: A choked jet with $L_{\rm j} = 10^{50}$erg/s, $t_{\rm w} = 0.5$, $t_{\rm j} = 0.5$. Middle Panel: A marginally successful jet (i.e., $\beta_{\rm h} \approx \beta_{\rm h,c}$) with $L_{\rm j} = 10^{51}$erg/s, $t_{\rm w} = 1$ and $t_{\rm j} = 0.5$. Bottom Panel: A successful jet with $L_{\rm j} = 10^{51}$erg/s, $t_{\rm w} = 0.5$ and $t_{\rm j} = 1$.

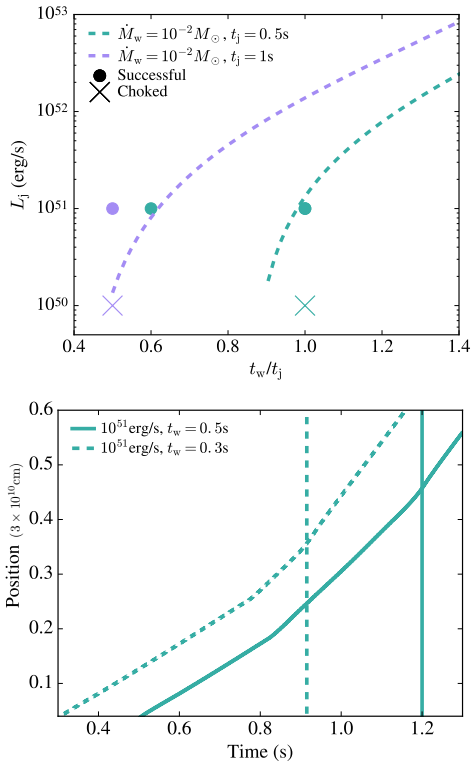

Figure 5.4: *Top* panel: The critical power needed in order to produce a successful sGRB for jets with varying $t_{\rm w}/t_{\rm j}$. This condition is derived from equation 5.5 assuming $\tilde{L}$ is constant. All cases are for a spherical, isotropic wind with a mass loss rate of $\dot{M}_{\rm w} = 10^{-2} M_\odot$/s. The unsuccessful jet simulations are marked with crosses and the dots represent successful cases. *Bottom* panel: The position of the head of the jet as a function of time for two of the teal cases plotted in the *top* panel. The corresponding vertical lines show when the jet breaks out of the wind. The dashed lines correspond to a simulation with $t_{\rm w} = 0.3$s, while the solid line is for a simulation with $t_{\rm w} = 0.5$s. The transition to the recollimation regime happens at 0.83s (0.78s) for the $t_{\rm w} = 0.5$s ($t_{\rm w} = 0.3$s) case.

this case, recollimation permits the jet to expand at a faster rate than the one predicted using the constant $\tilde{L}$ assumption. We thus caution the reader that such a constraint should be used as a conservative limit for the necessary jet power.

Additionally, the general formalism used to derive condition given by Eq. 5.5 makes use of spherical symmetry and as such its applicability is less rigorous when the jet expansion takes place within a non-spherical mass distribution. Figure 5.5 compares

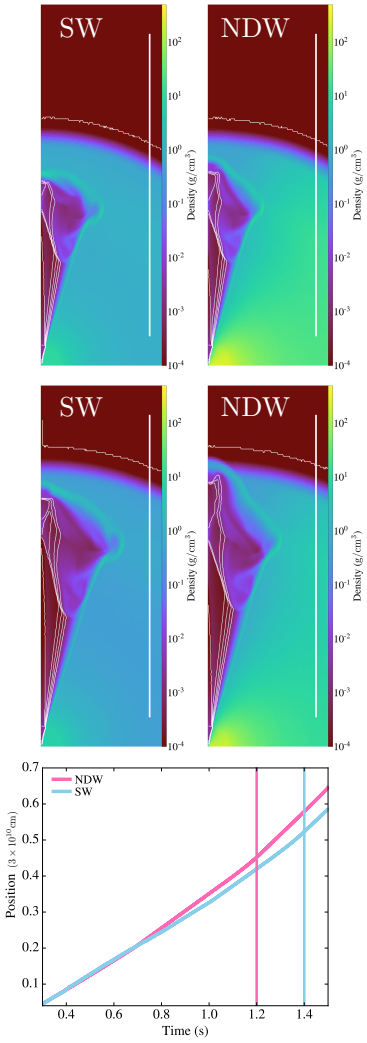

Figure 5.5: The evolution of two identical jets propagating in wind environments with different structure. The simulations are for $L_{\rm j} = 10^{50}$erg/s, the mass loss rate in the polar region is $\dot{M}_{\rm w} = 5 \times 10^{-3} M_{\odot}$/s, $t_{\rm w} = 0.3$s, and $t_{\rm j} = 1$s, and $\theta_0 = 14^{\circ}$. Here SW refers to a spherical wind while NDW refers to the neutrino-driven wind (NDW). Shown is a 1.5×10^{10} cm scale bar. *Top* panels: Comparison between the evolution of the jets at $t = 1$s. The contour lines represent lines with equal Lorentz factors. Shown in all cases is a 1.5×10^{10} cm scale bar. *Middle* panels: Same as the *top* panels but for $t = 1.25$s. *Bottom* panel: The position of the head of the jet for the two cases depicted above. The vertical lines gibe the time at which the jet breaks from the wind. The transition to the collimated regime occurs at 0.74s for the NDW and at 1s for the SW.

the evolution of two identical jets propagating in two different wind environments. The density profiles in both cases are similar in the polar region but NDW's profile is progressively denser as it approaches the equatorial region (Figure 5.1). When the jet propagates in the NDW, the cocoon region is significantly more confined due to the increase in the surrounding pressure. As a result, recollimation occurs earlier in the jet's propagation when compared to the spherical case and causes the jet to propagate at a faster speed. It is thus important to note that in the realistic wind cases considered in this paper, condition given by Eq. 5.5 provides a rather robust limit for the minimum luminosity require to produce a successful jet.

As demonstrated here, two dimensional simulations have uncovered some dynamical properties of relativistic flows unanticipated by analytical models, but we caution that there are still some key questions that they cannot tackle. A feature of the jet-wind interaction is that there will surely be some mass entertainment and maybe more importantly, there can be an exchange of linear momentum with the surrounding material. Because of this, we cautioned that higher resolution is needed because even a tiny mass fraction of baryons loading down the jet could severely limits the attainable Lorentz factor (here assumed to be only 10 for numerical convenience). Additionally, the symmetry-breaking involved in transitioning from two to three dimensions is crucial for understanding the nonlinear development of instabilities, leading to qualitatively new phenomena (Rossi et al. 2008; Meliani & Keppens 2010; López-Cámara et al. 2013; Gottlieb et al. 2018b,a; Matsumoto & Masada 2019; Gottlieb et al. 2020b). Another topic which seems ripe for a more sophisticated treatment concerns the possibility that

the initial jet is a magnetically confined configuration, whose collimation properties are not as drastically modified by the distribution of the external material (Mizuno et al. 2012; Bromberg & Tchekhovskoy 2016; Tchekhovskoy & Bromberg 2016; Geng et al. 2019; Nathanail et al. 2020a; Gottlieb et al. 2020a; Nathanail et al. 2020b; Mukherjee et al. 2020).

5.3.5 Jet structure

We perform different simulations, for a given wind profile, by altering the lifetime of the wind ($t_{\rm w}$), which is directly related to the time it takes the merger remnant to collapse to a black hole. We also changed the duration of the jet ($t_{\rm j}$), which is the characteristic time the central engine is active and is broadly related to the duration of the event. We show our results in Figures 5.6, 5.7 and 5.8, where we plot the density and Lorentz factor distributions of jets propagating through a spherical wind, a neutrino-driven wind and a magnetically ejected wind, respectively. The energy per unit solid angle at the end of the simulation is estimated as in Duffell et al. (2015).

The interaction of the jet with the wind will result in an angular redistribution of the jet's energy, which can naturally give rise to a different afterglow light curve than the one from the original top-hat structure (Lazzati et al. 2017; Duffell et al. 2018; Bromberg et al. 2018; Granot et al. 2018; Lamb & Kobayashi 2018; Kathirgamaraju et al. 2018; van Eerten et al. 2018; Lamb et al. 2019; Salafia et al. 2019; Lazzati et al. 2020; Gottlieb et al. 2020b). In what follows, we explore how the properties of the pre-collapse wind affect the structure of a jet propagating through it.

Common to all calculations is the altering of $t_{\rm w}$ and $t_{\rm j}$. Also shown is the final

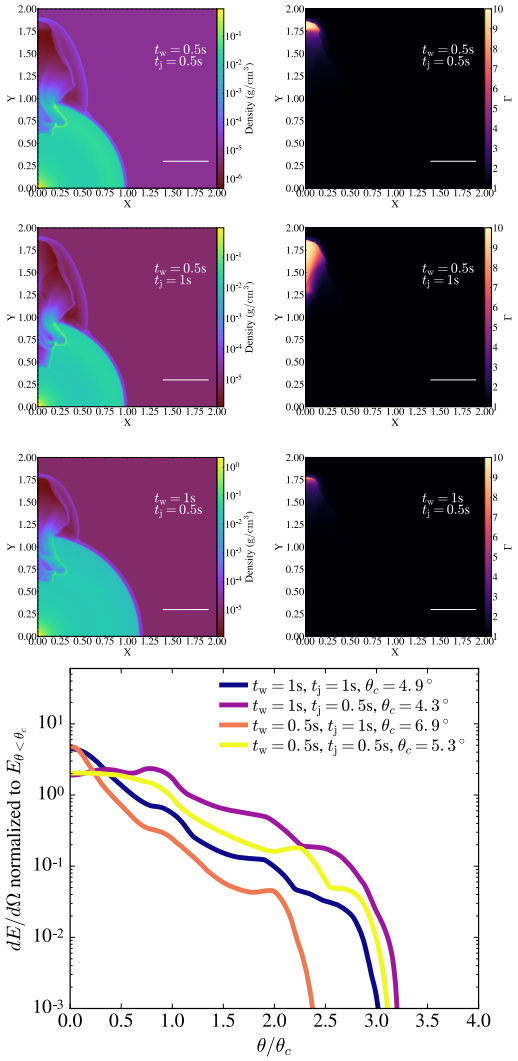

Figure 5.6: *Top* panels: Density (left) and Lorentz factor (right) profiles of simulations of the interaction of a relativistic jet with a spherical wind. The bar corresponds to 1.5×10^{10}cm. The luminosity is $L_{\rm j} = 1 \times 10^{50}$erg/s, the initial Lorentz factor $\Gamma = 10$, and the initial half-opening angle $\theta_0 = 10°$. The wind has an $\dot{M}_{\rm w} = 10^{-3} M_\odot$/s in the polar region and $v_{\rm w} = 0.3c$. Different simulations assume different collapse times and jet lifetimes. The simulations were run up to 4s. The *top* and *middle* snapshots were taken after 2.75s while the *bottom* one was taken after 3.25s. *Bottom* panel: Energy per unit angle of the resulting jet. The time is the same as the above panel. For $t_{\rm w} = 1$ and $t_{\rm j} = 1$, the time is 3.25s. The energy is normalized to the total energy in the core of the jet.

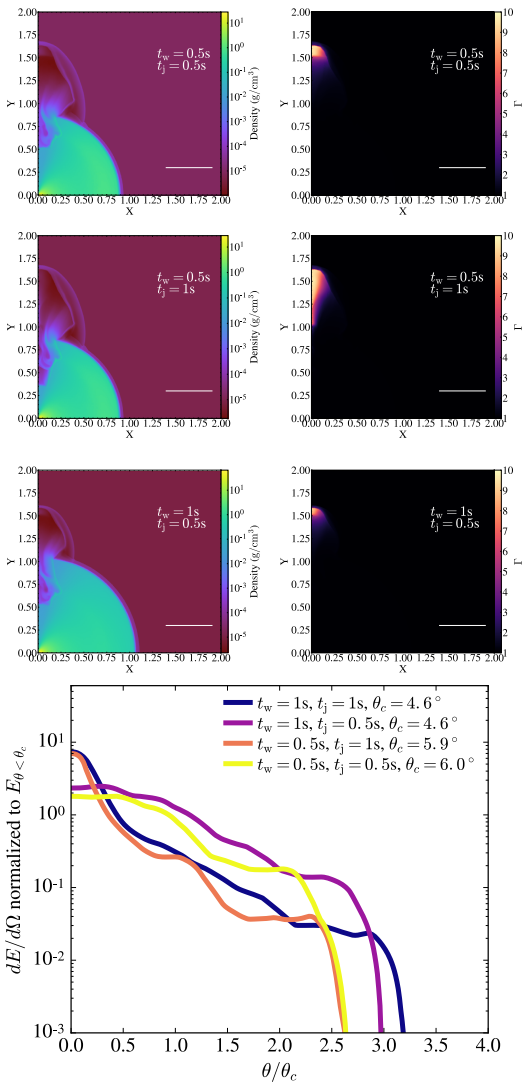

Figure 5.7: Top panels: Density (left) and Lorentz factor (right) profiles of simulations of the interaction of the relativistic jet with a neutrino-driven wind. Shown is a 1.5×10^{10} cm scale bar. The properties of the jet are the same as in Fig 5.6. The top and middle panels show snapshots after 2.5s while 3s for the bottom panel. The wind has a mass loss rate of $\dot{M}_{\rm w} = 10^{-3}M_\odot/{\rm s}$ in the polar region and a velocity of $v_{\rm w} = 0.3c$. Bottom panel: Energy per unit angle of the jet after its propagation. The time is the same as the above panel, for $t_{\rm w} = 1$ and $t_{\rm j} = 1$, the time is 3s, and for $t_{\rm w} = 0.3$ and $t_{\rm j} = 1$, the time is 2.25s. The energy is normalized to the energy in the core.

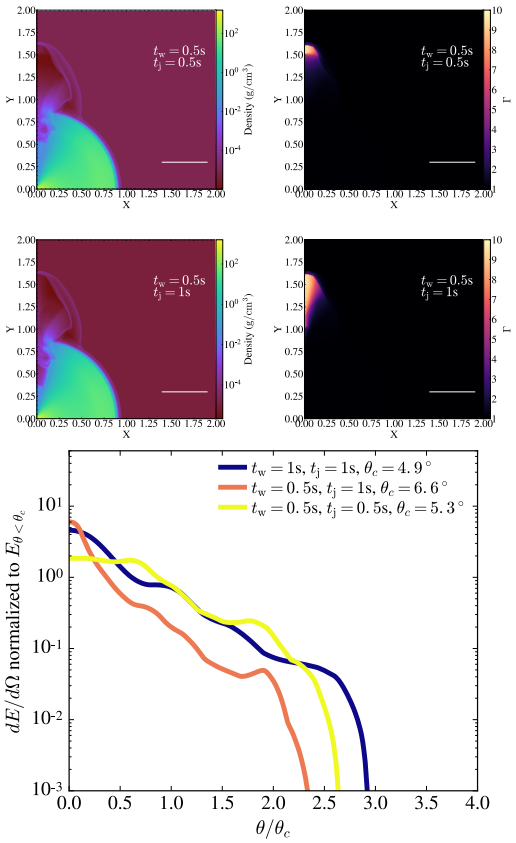

Figure 5.8: Top panels: Density (left) and Lorentz factor (right) profiles of simulations of the interaction of a relativistic jet with a magnetized wind based on Janiuk (2019). Shown is a 1.5×10^{10} cm scale bar. The properties of the jet are the same as in Fig 5.6. The wind has a mass loss rate of $\dot{M}_{\rm w} = 10^{-3} M_\odot$/s in the polar region and $v_{\rm w} = 0.3c$. The top and middle Panels correspond to a simulation time of 2.5s. The simulation corresponding to $t_{\rm w} = 1$s, $t_{\rm j} = 0.5$s is not shown as the wind in that case is dense enough to choke the jet, rendering the sGRB unsuccessful. Bottom panel: Energy per unit angle of the jet resulting from the simulations. The time is the same as the above panel. For $t_{\rm w} = 1$ and $t_{\rm j} = 1$, the time is 3.25s. The energy is normalized to the energy in the core.

angular distribution of the energy in the relativistic jet. In all simulations we define the core angle of the jet, after its propagation, as the angle where the Lorentz factor of the jet decreases by a factor of 2 from its initial value. The resulting core angles range from 4.5° to 7°, which are similar to the values quoted in the literature (Lyman et al. 2018; D'Avanzo et al. 2018; Troja et al. 2018; Salafia et al. 2019; Ghirlanda et al. 2019; Lazzati et al. 2020; Nathanail et al. 2020a). The final angular distribution of Lorentz factor is found to be well represented by a Gaussian distribution. In all cases, the jet, which is originally a top-hat, spreads laterally thus resulting in a structured jet.

In addition to the density of the wind, which depends primarily on the mass loss rate, the ratio $t_{\rm w}/t_{\rm j}$ has a decisive effect on the appearance of a jet propagating through it. This is because it determines the time the jet resides within the interaction region (as governed by $\tilde{L}$) which in turn regulates the amount of relativistic material that is shocked. The importance of this ratio can be clearly seen in the Bottom panels of Figures 5.6, 5.7 and Figure 5.8. If the delay time is larger or comparable to the duration of the jet, the time it takes for the jet to break free from the wind is augmented. In this case, the afterglow emission would be dominated by the emission of the laterally spreading relativistic material, which is located at larger angles relative to the rotation axis of the merger remnant. On the other hand, if the jet produced by the accretion onto the black hole maintains its energy for much longer than it takes the jet head to reach the edge of the wind, the core of the relativistic jet would contain substantially more energy than the off-axis material, so that it is likely to dominate the afterglow flux even after expanding for a longer time. The detection of varying afterglow signatures would

be a test of the neutron star merger model; and the precise inference of the angular structure of the jet may help constrain the properties of the wind and the lifetime of the merger remnant.

The strength of the baryon loaded wind is also a key parameter. If the mass loss rate is increased to $\dot{M}_{\rm w} = 10^{-2} M_{\odot}/{\rm s}$ in the polar region and the luminosity is kept at $L_{\rm j} = 10^{50}{\rm erg/s}$, the wind would choke the jet, rendering the sGRB unsuccessful. The jet, in this environment can become successful if its power is increased, as governed by $\tilde{L}$ (Bromberg et al. 2011). In Figure 5.9, we show the effects of altering the mass loss rate and the luminosity of the wind but leaving $\tilde{L}$. unchanged. As expected, the evolution of the jet remains unchanged and the simulation outputs in these two cases look almost identical.

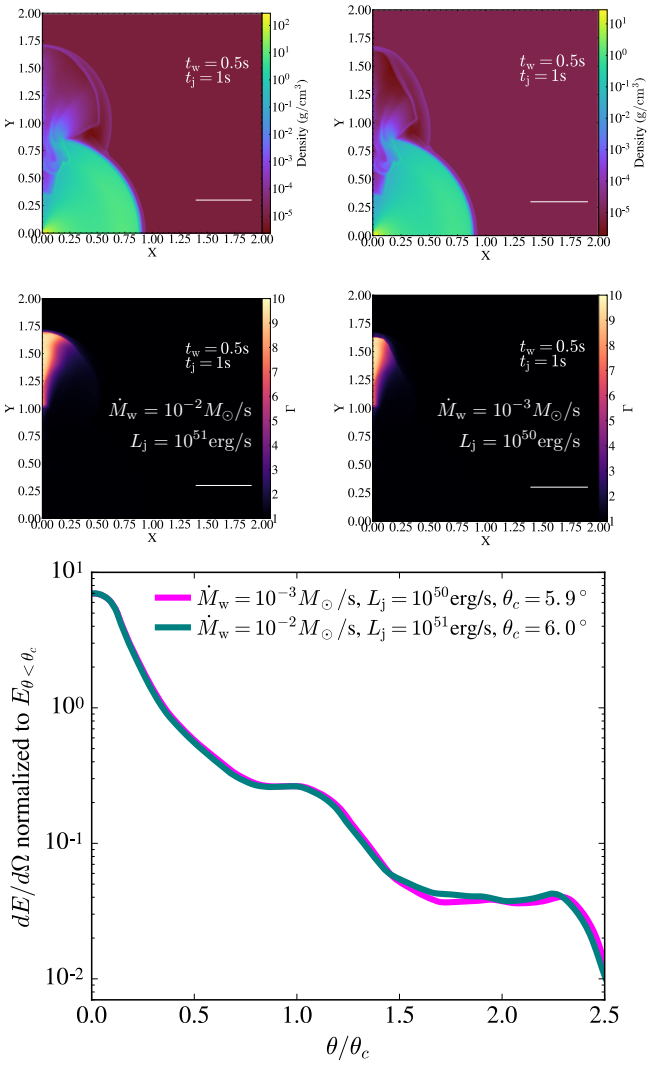

Figure 5.9: Top and middle panels: Density snapshots with Lorentz factor for simulations that have the same $\tilde{L}$. On the left, the wind has a mass loss rate in the equator of $\dot{M}_w = 10^{-2} M_\odot$/s and the jet has a luminosity of $L_j = 10^{51}$erg/s. On the right, the wind has a mass loss rate in the equator of $\dot{M}_w = 10^{-3} M_\odot$/s and the jet has a luminosity of $L_j = 10^{50}$erg/s. The density profile used here is the neutrino-driven wind. Shown is a 1.5×10^{10} cm scale bar. The jets are shown at $t = 2.5$s. Bottom Panel: Energy per unit angle of the jet after its propagation. The energy is normalized to the energy in the core.

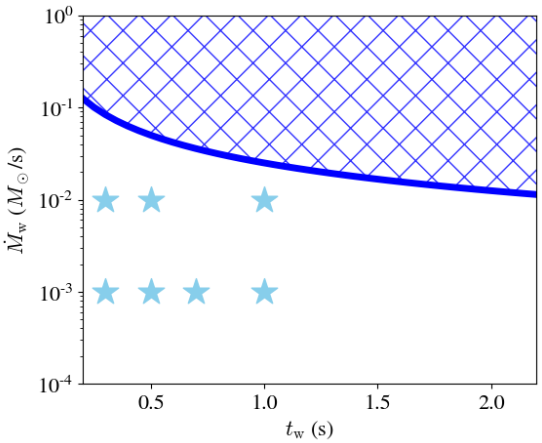

Figure 5.10: Distribution of mass loss rate and wind duration time. The blue stars represent the values for the simulations performed in this study. The blue line represents the combination of mass loss rate and t_w that give an ejecta mass of $M_{\rm ejecta} = 0.025 M_\odot$ (Kasen et al. 2017). Above this line, the parameter space is not permitted by observations of the blue kilonova.

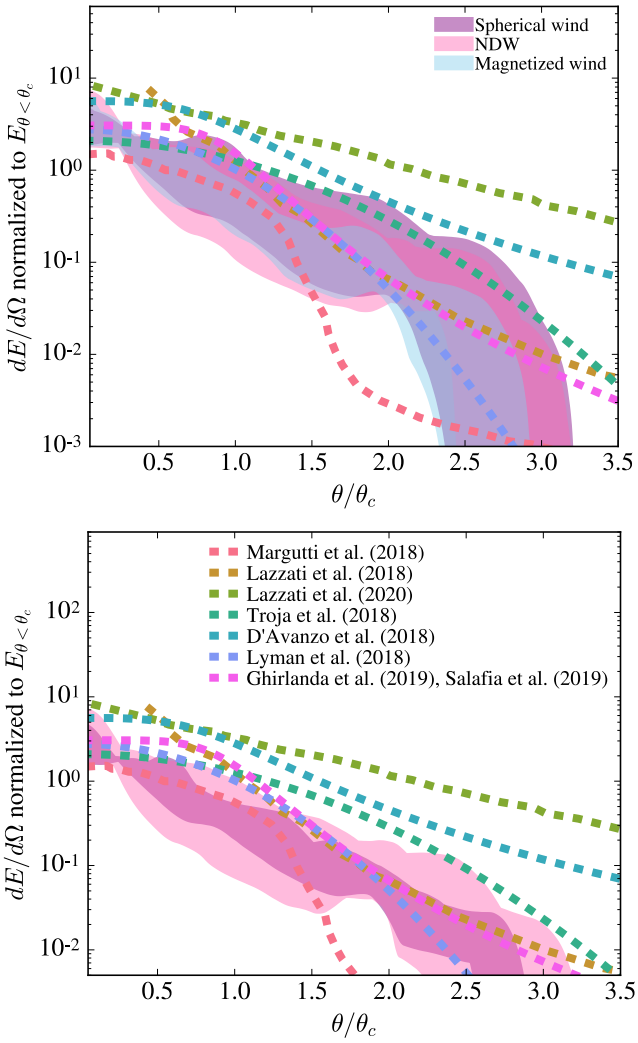

Figure 5.11: Comparison of different jet profiles used to model the emission of GW170817 with those obtained from our simulations. *Top* panel: Jet profiles for the various winds at a fixed jet luminosity of 10^{50}erg/s but varying $t_{\rm w}/t_{\rm j} = 0.3,\ 0.5,\ 1,\ 2$. The dotted lines show the jet profiles inferred for GW170817 and taken from Lazzati et al. (2018); Margutti et al. (2018); Lyman et al. (2018); D'Avanzo et al. (2018); Troja et al. (2018); Ghirlanda et al. (2019); Salafia et al. (2019); Lazzati et al. (2020). *Bottom* panel: Jet profiles resulting from the interaction of a jet with a NDW and a spherical wind with $\dot{M}_{\rm w} = 10^{-2} M_\odot$/s in the polar region. The jet's luminosity is 10^{51}erg/s, and $t_{\rm w}/t_{\rm j} = 0.3,\ 0.5,\ 1,\ 2$ for the NDW, while $t_{\rm w}/t_{\rm j} = 0.5,\ 1,\ 2$ for the SW.

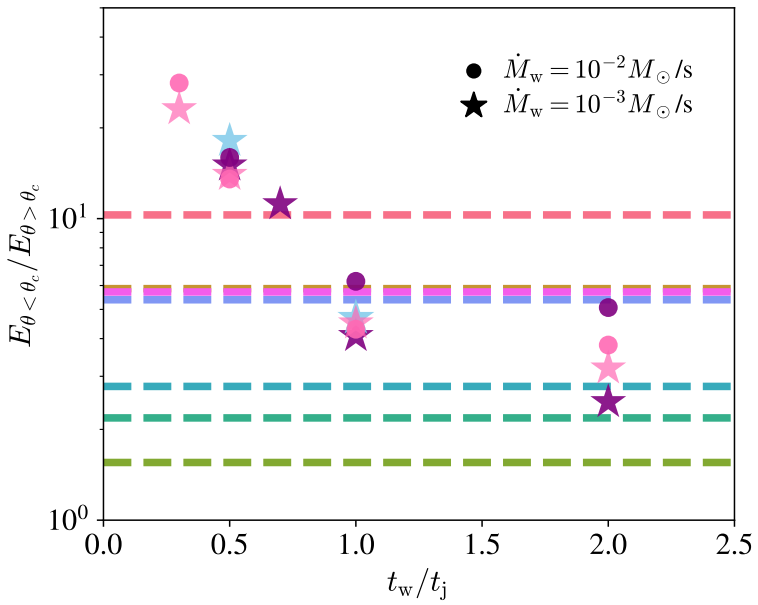

Figure 5.12: Comparison of the relativistic energy content in the jet's core, $E_{\theta<\theta_c}$, with that stored in the wings, $E_{\theta>\theta_c}$. This ratio is plotted as a function of $t_{\rm w}/t_{\rm j}$ for the three different wind profiles: NDW (pink); spherical wind (purple) and magnetized wind (blue). The stars represent simulations with $\dot{M}_{\rm w} = 10^{-3} M_\odot$/s in the polar region and $L_{\rm j} = 10^{50}$erg/s while the circles represent simulations with $\dot{M}_{\rm w} = 10^{-2} M_\odot$/s in the polar region and $L_{\rm j} = 10^{51}$erg/s. The constant lines represent the same energy ratio taken from GW170817 jet simulations (Lazzati et al. 2018; Margutti et al. 2018; Lyman et al. 2018; D'Avanzo et al. 2018; Troja et al. 2018; Ghirlanda et al. 2019; Salafia et al. 2019; Lazzati et al. 2020), where the color scheme for the various models is the same as in Figure 5.11.

5.4 Relevance to GW170817

Several groups (Lazzati et al. 2018; Margutti et al. 2018; Lyman et al. 2018; D'Avanzo et al. 2018; Troja et al. 2018; Ghirlanda et al. 2019; Salafia et al. 2019; Lazzati et al. 2020) have studied the origin of the afterglow emission of GW170817 and concluded that it can be explained by invoking a model where the sGRB was successful and the observer lies off axis to the jet. A common feature of all models is the need for significant amount of energy at larger angles, which as we have argued here can be a natural consequence of the interaction of the jet with the pre-collapse wind. In this section we endeavor to compare our simulation results to the jet models constructed for GW170817.

In Figure 5.10 we plot the range of wind parameters used in our study and compare them with the constraints derived by the presence of the blue kilonova. The blue line represents the limit marked by the total mass derived to produce the blue component of the kilonova (Kasen et al. 2017). We note that the total mass ejected by the wind in our simulations is below this value.

Various groups inferred different energy distributions for the jet. In Figure 5.11 we compare their best fit models for the jet profiles with those obtained from our simulations. The results from our simulations are in broad agreement with the energy distributions derived from afterglow observations. We thus conclude that the structure of an initially top-hat jet can be modified by its interaction with the pre-collapse wind and, after the jet emerges from this region, can have a structure that closely resembles the one deduced for GW170817. So in these models the γ-rays would be restricted to

a narrow beam, even though outflow with a more moderate Lorentz factor, which is relevant to the afterglow emission, is spread over a wider range of angles.

While the properties of the pre-collapse wind have an important effect on the appearance of a jet propagating through it (Figure 5.11), our calculations suggest that $t_{\rm w}/t_{\rm j}$ is the essential parameter that controls how much relativistic energy is distributed at large angles.

Figure 5.12 illustrates the effect of varying $t_{\rm w}/t_{\rm j}$ for jets propagating within the three different wind profiles we have considered in this study and the different mass loss rates. It shows how the ratio of the energy contained in the core of the jet to that residing outside it increases as $t_{\rm w}/t_{\rm j}$ augments. As argued above, we also see that changes in the mass loss rate have a less dramatic effect when compared to variations in $t_{\rm w}/t_{\rm j}$.

In the case of a successful break-through, the resultant jet structure could result in an afterglow signature similar to that observed in GW170817 if the time it took for the merger remnant to collapse is similar to the observed duration of the event. An upper limit for $t_{\rm w}$ can be derived by requiring a successful jet (Murguia-Berthier et al. 2017b). A successful jet can be produced if the central engine remains active for a time longer than the time it takes for the jet to break through the wind:

$$t_{\rm w} \lesssim t_{\rm j} \frac{\beta_{\rm h} - \beta_{\rm w}}{\beta_{\rm w}}, \tag{5.6}$$

where $\beta_{\rm w} = v_{\rm w}/c$, $\beta_{\rm h} = v_{\rm h}/c$ and the subscript h referring to the head of the jet. This condition is derived using the evolution of the working surface, where the velocity of

the head of the jet is given by Equation 5.3.

A lower limit for $t_{\rm w}$ can be found using Figure 5.12, which shows that in order for our models to explain the afterglow of GW170817, a long interaction with the wind is required. In particular, in order to be in agreement with the most recent afterglow models, we require $t_{\rm w}/t_{\rm j} \gtrsim 0.7$. At smaller $t_{\rm w}/t_{\rm j}$, the core of the jet carries the bulk of the energy and, as such, it would closely resemble a top-hat model which is inconsistent with current observations. Models that have more extended wings carrying a larger amount of energy thus require longer interaction times between the jet and the wind. Using $t_{\rm j} = 2 \pm 0.5$s (Goldstein et al. 2017), we derive the following stringent limit $t_{\rm w} \gtrsim 1.05$s.

The constraint given above can be combined with the successful sGRB requirement given by Equation 5.6 in order to derive a range of permitted values for $t_{\rm w}$. Making use of the broad range of values derived for GW170817, in Figure 5.13 we show the allowed (pink) region for $t_{\rm w}$ as a function $\dot{M}_{\rm w}$. The lower limit, which is independent of $\dot{M}_{\rm w}$, is derived from the requirement that $t_{\rm w}/t_{\rm j} \gtrsim 0.7$, as seen in Fig 5.12.The upper limit, on the other hand, is derived using equation 5.6 with the additional constraint that $\dot{M}_{\rm w} \gtrsim 10^{-3} M_{\odot}$/s as motivated by the range of realistic values seen in merger calculations (Siegel et al. 2014a; Fujibayashi et al. 2018; Nathanail et al. 2019; Perego et al. 2014a). A strict upper limit for the time of collapse can be obtained by taking into account the time delay between the GW and the γ-ray signal, which has been observed to be around ≈ 1.7s (Abbott et al. 2017c; Goldstein et al. 2017). The three constraints can then be combined to derive a range of permitted values for $t_{\rm w} \approx 1 - 1.7$s.

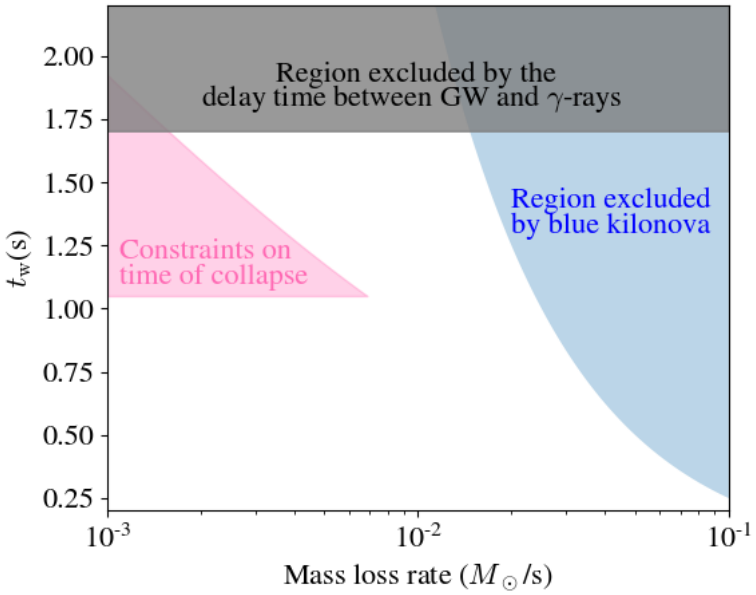

Figure 5.13: Constraints on $t_{\rm w}$ as a function of $\dot{M}_{\rm w}$. The upper limit is derived using Eq. 5.6. We use $t_{\rm j} = 2 \pm 0.5$s (Goldstein et al. 2017) and the following ranges obtained by Lazzati et al. (2020) for GW170817: $5 \times 10^{48} - 10^{50}$erg (jet energy) and $9 - 20^\circ$ (initial jet opening angle), which we use to obtain the isotropic luminosity. For consistency we use $10^2 < \Gamma < 10^3$, yet its exact value does not meaningfully alter the value of $\beta_{\rm h}$ provided that the flow is highly relativistic. The grey region is excluded by the delay time between the gravitational wave (GW) and the γ-ray signal (Abbott et al. 2017c; Goldstein et al. 2017). The blue region is the one excluded by observations, which is also plotted in Figure 5.10.

This finding gives further credence to the idea that in the case of GW170817, the collapse into a black hole was indeed delayed. Yet this argument comes from a completely different line of reasoning than those given in the literature:

- Granot et al. (2017) set a constraint of $t_{\rm w} \lesssim 0.9$ s based on the expected lifetime of a hyper-massive NS.

- Gottlieb et al. (2018b) find $t_{\rm w} < 1$s based on the time of the shock breakout compared to the observed delay between gravitational waves and the γ-rays.

- Nakar et al. (2018) perform simulations of a mildly relativistic cocoon using a time delay of $t_{\rm w} \approx 0.8 - 1$s which is able to reproduce the observed data.

- Gottlieb et al. (2018b) perform simulations of a cocoon shock breakout and they can reproduce the observed afterglow emission with $t_{\rm w} \approx 1$s.

- Metzger et al. (2018) set a constraint of $t_{\rm w} \approx 0.1 - 1$s based on the amount of blue ejecta expected from a magnetized wind.

- Xie et al. (2018) perform numerical simulations and show that a delay time of $t_{\rm w} \sim 1$s is able to reproduce the afterglow data

- Gill et al. (2019b) did a comprehensive analysis and estimated the collapse time to be $t_{\rm w} = 0.98^{+0.31}_{-0.26}$s. They combined several constraints including the delay time between the gravitational wave and electromagnetic signal, a comparison on the observational mass of the blue ejecta and constraints based on a successful jet.

- van Putten et al. (2019) obtain a limit of $t_{\rm w} \approx 0.67 \pm 0.3$s based on observations of extended emission.

- Lazzati et al. (2020) favour the delay time to be around $t_{\rm w} < 1.1$s by parameter space exploration of jet-wind interactions using an analytical formalism.

- Hamidani et al. (2020) analytically estimate a delay time of $t_{\rm w} < 1.3$s which they compared to detailed numerical calculations.

Our estimate for $t_{\rm w}$, which is based on the angular structure of a successful jet as inferred from afterglow observations, is roughly consistent with these various estimates.

Many binary neutron star mergers are thought to produce sGRBs when collapsing to black holes but some merger remnants may experience significant delays before collapsing. One expects various outcomes ranging from sGRBs with narrow beams from prompt collapse to structured jets with bright and weak sGRBs for longer collapse timescales. The properties of the afterglow signatures produced by successful and non-successful jets would provide a natural test to distinguish between these different progenitor avenues. The different jet structure can be used to obtain the different afterglow emission (De Colle et al. 2012b, 2018; Urrutia et al. 2020).

Chapter 6

Post merger phase: accretion disks

6.1 Chapter Abstract

The first binary neutron star merger has already been detected in gravitational waves. The signal was accompanied by an electromagnetic counterpart including a kilonova component powered by the decay of radioactive nuclei, as well as a short γ-ray burst. In order to understand the radioactively-powered signal, it is necessary to simulate the outflows and their nucleosynthesis from the post-merger disk. Simulating the disk and predicting the composition of the outflows requires general relativistic magnetohydrodynamical (GRMHD) simulations that include a realistic, finite-temperature equation of state (EOS) and self-consistently calculating the impact of neutrinos. In this work, we detail the implementation of a finite-temperature EOS and the treatment

of neutrinos in the GRMHD code HARM3D+NUC, based on HARM3D. We include formal tests of both the finite-temperature EOS and the neutrino leakage scheme. We further test the code by showing that, given conditions similar to those of published remnant disks following neutron star mergers, it reproduces both recombination of free nucleons to a neutron-rich composition and excitation of a thermal wind.

6.2 Introduction

On August 17, 2017, the LIGO/VIRGO collaboration detected the first gravitational wave signal arising from the merger of two neutron stars (Abbott et al. 2017c). This signal was accompanied by a counterpart observed all over the electromagnetic spectrum (Abbott et al. 2017d; Murguia-Berthier et al. 2017c; Coulter et al. 2017b; Shappee et al. 2017). This event, named GW170817, gave credence to the idea that at least a subset of neutron star mergers give rise to short γ-ray bursts (sGRBs; Eichler et al. 1989; Narayan et al. 1992; Lee & Ramirez-Ruiz 2007b; Nakar 2007).

In order to understand the electromagnetic emission, we need to study the properties of merger. After the two neutron stars merge, the fate of the remnant depends on the final mass of the resulting object. If the final mass is less than the mass allowed for an object with rigid rotation, then the remnant will be a stable neutron star. On the other hand, if the final mass is larger, then it can result in a hot hyper-massive neutron star (HMNS), supported by differential rotation, or it can promptly collapse to a black hole (Shibata & Taniguchi 2006; Baiotti et al. 2008; Ravi & Lasky 2014). In both cases, the compact object will be surrounded by an accretion disk (Eichler

et al. 1989; Baiotti et al. 2008). If the result is an HMNS, there will be transport of mass and angular momentum from the inner edge to the outer edge that will drive the HMNS to rigid rotation, where it can either remain stable, or undergo a delayed collapse to a black hole (BH; see Nakar 2019, for a recent review). It is widely believed that GW170817 resulted in a delayed collapse to a black hole (Margalit & Metzger 2017). In any case, the compact object is left surrounded by an accretion disk containing highly neutron-rich material (Lee & Ramirez-Ruiz 2007b).

The post-merger accretion disk will be entirely opaque to photons (Popham et al. 1999; Narayan et al. 2001; Lee et al. 2004, 2005b, 2009). As we go deeper in the disk, due to the high density and temperature, neutrinos (and anti-neutrinos) will be created via the charged β-process, electron-positron annihilation, and plasmon decay (Narayan et al. 2001; Di Matteo et al. 2002; Chen & Beloborodov 2007). In the region where the neutrinos are created, matter will be optically thin to neutrinos. In even deeper regions, matter will be optically thick to neutrinos. In the optically thin region, free neutrinos will carry energy away, and cool the disk, making it geometrically thinner (Chevalier 1989; Houck & Chevalier 1991).

Further out in the the disk, where neutrinos are no longer created in substantial numbers, free nucleons will recombine into α-particles. The photons will still be trapped in the disk, therefore the disk will be thicker and radiatively inefficient (Popham et al. 1999; Narayan et al. 2001; Lee et al. 2004, 2005b, 2009). An outflow arises due to instabilites in the accretion disk from its magnetic field (Balbus & Hawley 1998). The instabilities will transport angular momentum at significant rates, dissipating energy

and driving a high velocity outflow. In addition, the recombination of free nucleons into $\alpha-$particles is capable of unbinding part of the material from the disk (Lee et al. 2009; Fernández & Metzger 2013a).

Aside from material ejected from the disk, there are other outflows from the binary merger that will significantly contribute to the electromagnetic emission, including a dynamical ejecta (see, for example Rosswog et al. 1999; Fernández et al. 2015; Radice et al. 2016), and a neutrino-driven wind (Dessart et al. 2009; Fernández & Metzger 2013a; Perego et al. 2014b; Kasen et al. 2017; Fernández et al. 2017). As the different outflows expand and cool down, heavy elements are synthesised via the rapid neutron capture process (r-process) (Freiburghaus et al. 1999; Kulkarni 2005; Fernández & Metzger 2013b; Lippuner & Roberts 2015; Palenzuela et al. 2015; Radice et al. 2016; Roberts et al. 2017; Fernández et al. 2017; Lippuner et al. 2017; Radice et al. 2018; Zenati et al. 2019; Radice et al. 2020). After neutrons are exhausted, elements will radioactively decay and heat the surrounded material, which will thermally emit in the optical/IR bands (Li & Paczyński 1998b; Metzger et al. 2010a; Roberts et al. 2011b; Kasen et al. 2013b; Barnes & Kasen 2013; Tanaka & Hotokezaka 2013; Grossman et al. 2014; Kasen et al. 2015b; Barnes et al. 2016; Rosswog et al. 2017; Kasen & Barnes 2019; Siegel 2019); in particular, see Metzger (2019) and references within. This emission, called a *kilonova*, was detected for GW170817 (Drout et al. 2017; Kilpatrick et al. 2017; Soares-Santos et al. 2017; Tanvir et al. 2017; Smartt et al. 2017; Nicholl et al. 2017; Cowperthwaite et al. 2017; Villar et al. 2017; Kasen et al. 2017; Pian et al. 2017; Kasliwal et al. 2019). It is predicted that if the composition of the ejecta includes lanthanides,

the emission tends to be more red and peak at later times, whereas if there are no third peak elements, the emission tends to be bluer and peaks earlier (Barnes & Kasen 2013; Tanaka & Hotokezaka 2013). Understanding the nucleosynthesis, and the amount of mass ejected is therefore important when deciding the best strategy to observe and perform surveys for kilonovae. This paper will focus on the disk ejecta.

The key parameter in determining the rate of nucleosynthesis, and in particular whether third peak r-process elements (including the lanthanides) are created in the disk ejecta, is the electron fraction of the ejected material (Kasen et al. 2013b; Lippuner & Roberts 2015; Roberts et al. 2017; Lippuner et al. 2017; Kasen et al. 2017; Just et al. 2021). The problem is that the composition of these ejecta varies between different simulations with results ranging from compositions dominated by iron peak elements to ejecta dominated by lanthanides (e.g., Janiuk 2014; Fernández et al. 2015; Foucart et al. 2018; Janiuk 2019; Siegel & Metzger 2018; Miller et al. 2019b). One of the significant differences between the simulations is in the neutrino treatment. Neutrinos carry away energy and lepton number, altering the electron fraction and the final ejecta mass and they significantly alter the composition of the ejected material. Thus, simulations need to model the composition and thermodynamic state of the ejecta as realistically as possible to understand and model the kilonova emission.

In order to model the post-merger disk, we need to self-consistently include multiple relevant physical processes. Due to the compact nature of the BH, we need to consider general relativity (GR). Due to the importance of the magnetic stresses we need to include magneto-hydrodynamics (MHD). Additionally, to self-consistently

include the addition of neutrinos and recombination energy, we need both a realistic equation of state (EOS) and a way in which to consider the impact of neutrinos in the optically thick and thin regions.

There have been many previous efforts to simulate a black hole surrounded by an accretion disk in the context of a binary neutron star. A brief (and certainly incomplete) summary of the numerical efforts is below.

Numerical simulations initially added neutrino physics by adding pressure terms in the EOS and adding emission and heating/cooling terms from weak reactions in hydrodynamical simulations (Popham et al. 1999; Narayan et al. 2001; Di Matteo et al. 2002; Kohri & Mineshige 2002; Lee et al. 2004, 2005b; Metzger et al. 2008a; Zalamea & Beloborodov 2011). There have been general relativistic magnetohydrodynamical (GRMHD) simulations in 2d with analytical terms for the neutrino pressure with approximations by Di Matteo et al. (2002) that also include nuclear reactions using the GRMHD code HARM2D (Janiuk et al. 2013; Janiuk 2014, 2019). There have been efforts performing simulations of binary neutron stars, or a hyper-massive NS, with an accretion disk in 3d with GRMHD but without neutrinos (for example, Siegel et al. 2014b; Kiuchi et al. 2014, 2015b; Dionysopoulou et al. 2015; Ruiz et al. 2016; Ciolfi et al. 2017; Kiuchi et al. 2018; Ruiz et al. 2018). Also, groups simulated disks after the merger of binary NS including GR with some kind of neutrino transport but including no magnetic fields (Foucart et al. 2016; Fujibayashi et al. 2017; Nedora et al. 2021). Other groups performed hydrodynamical calculations with neutrino physics, including neutrino leakage schemes and a transport scheme but no magnetic fields (Ruffert et al.

1996; Rosswog & Liebendörfer 2003; Metzger & Fernández 2014; Perego et al. 2014b; Martin et al. 2015; Fernández et al. 2015; Just et al. 2015).

Foucart et al. (2015, 2018) performed general relativistic hydrodynamical (GRHD) simulations and compared different neutrino treatments, including neutrino transport and leakage schemes. Additionally, Siegel & Metzger (2018) and De & Siegel (2020) performed GRMHD simulations of a magnetized torus with a neutrino leakage scheme and the Helmholtz equation of state. **?** compared 3d simulations of magnetized and unmagnetized accretion disks with GRMHD including a neutrino leakage scheme. Li & Siegel (2021) performed an M1 scheme with neutrino conversions. There have also been GRMHD simulations that included a tabulated EOS with neutrino transport using Monte-Carlo methods (Miller et al. 2019a,b).

In this paper, we present simulations using HARM3D+NUC, based on HARM3D, considering the impact of neutrinos through a leakage scheme and a multi-component, finite-temperature EOS. HARM3D is a versatile GRMHD code that has been well tested and used in many astrophysical scenarios. It uses arbitrary coordinates, allowing for a more accurate conservation of angular momentum. Additionally, it has copious analysis tools developed over the years. The addition of a neutrino leakage scheme and tabulated EOS into HARM3D+NUC is a stepping stone that allows for further advances. The paper is structured as follows: in Section 7.3 we discuss how we implemented the realistic EOS and the leakage scheme. In Section 6.4 we describe the tests we performed to validate the implementation of the tabulated EOS including a torus in hydrostatic equilibrium. In Section 6.5 we describe the tests we performed to validate the leakage

scheme, and in Section 6.6 we use both the tabulated EOS and leakage scheme to better simulate a torus with a magnetic field.

6.3 Methods

In order to accurately simulate accretion disks, we need the ability to solve the general relativistic magnetohydrodynamics (GRMHD) equations with a realistic equation of state (EOS) and a way to account for the effect neutrinos and anti-neutrinos have on the material's energy and electron fraction. In this section, we explain how we added a tabulated EOS and neutrino leakage scheme to HARM3D, in a new code called HARM3D+NUC.

6.3.1 HARM3D+NUC

HARM3D (Gammie et al. 2003a; Noble et al. 2006a, 2009) solves the GRMHD equations in conservative form. HARM3D is a well tested code that can handle arbitrary coordinate systems, which allows for less numerical diffusion and better conservation of angular momentum when using coordinate systems that more closely conform to local symmetries of the problem (Zilhão & Noble 2014). Below we set $G = c = 1$. The GRMHD equations of motion include the baryon conservation equation,

$$\nabla_\mu \left(n_b u^\mu \right) = 0 \quad , \tag{6.1}$$

the energy-momentum conservation equations (with a heating/cooling source, neglecting momentum transfer)

$$\nabla_\mu T^\mu{}_\nu = \mathcal{Q} u_\nu \quad , \tag{6.2}$$

and Maxwell's equations

$$\nabla_\nu {}^*F^{\mu\nu} = 0 \quad , \tag{6.3}$$

$$\nabla_\nu F^{\mu\nu} = J^\mu \quad , \tag{6.4}$$

where u^μ is the 4-velocity of the fluid, $\mathcal{Q}$ is the energy change rate per volume in the comoving fluid frame (due to neutrino heating/cooling), n_b is the number density of baryons, $F^{\mu\nu}$ is the Faraday tensor times $1/\sqrt{4\pi}$, ${}^*F^{\mu\nu}$ is the dual of this tensor or the Maxwell tensor times $1/\sqrt{4\pi}$, and J^μ is the 4-current[8]. In practice, we don't use Eq. (6.4), since we work in the limit of ideal MHD. The change in the conservation of lepton number is

$$\nabla_\mu \left(n_e u^\mu\right) = \mathcal{R}/m_b \quad , \tag{6.5}$$

where n_e is the number density of electrons, $\mathcal{R} = -\mathcal{R}_{\nu_e} + \mathcal{R}_{\bar{\nu}_e}$ is the difference in the net rate of neutrino and anti-neutrino number per volume in the comoving fluid frame.

Note that the rest-mass density of the gas (mass per unit volume) is dominated by the baryon mass, $\rho \approx m_b n_b$, where m_b is the baryon mass. The baryon number conservation equation can then be replaced by the regular continuity equation:

$$0 = m_b \nabla_\mu \left(n_b u^\mu\right) = \nabla_\mu \left(m_b n_b u^\mu\right) = \nabla_\mu \left(\rho u^\mu\right) \quad . \tag{6.6}$$

[8] We follow Gammie et al. (2003a) in our definition of the electromagnetic field tensor and magnetic field variables.

Instead of using n_e and n_b, we may use the fluid density ρ and the electron fraction Y_e:

$$Y_e \equiv \frac{n_e}{n_b} = \frac{n_e}{\rho/m_b} = \frac{m_b n_e}{\rho} \tag{6.7}$$

or $Y_e\rho = m_b n_e$ and we can therefore multiply Eq. (6.5) by m_b to yield the electron fraction equation:

$$\nabla_\mu \left(\rho Y_e u^\mu\right) = \mathcal{R} \quad . \tag{6.8}$$

The total stress-energy tensor is the sum of the fluid part,

$$T^{\mu\nu}_{\rm fluid} = \rho h u^\mu u^\nu + P g^{\mu\nu}, \tag{6.9}$$

and the electromagnetic part

$$\begin{aligned} T^{\mu\nu}_{\rm EM} &= F^{\mu\lambda}F^{\nu}{}_{\lambda} - \frac{1}{4} g^{\mu\nu} F^{\lambda\kappa}F_{\lambda\kappa} & (6.10)\\ &= ||b||^2 u^\mu u^\nu + \frac{1}{2}||b||^2 g^{\mu\nu} - b^\mu b^\nu \quad , & (6.11) \end{aligned}$$

where we adopt the ideal MHD condition

$$u_\lambda F^{\lambda\kappa} = 0 \quad , \tag{6.12}$$

and where $g_{\mu\nu}$ is the metric, $h = (1 + \epsilon + P/\rho)$ is the specific enthalpy, P is the pressure, ϵ is the specific internal energy density, $b^\mu = {}^*F^{\nu\mu}u_\nu$ is the magnetic field 4-vector, and $||b||^2 \equiv b^\mu b_\mu$ is twice the magnetic pressure P_m.

Equations (6.2-6.6) can be expressed in flux conservative form

$$\partial_t \mathbf{U}(\mathbf{P}) = -\partial_i \mathbf{F}^i(\mathbf{P}) + \mathbf{S}(\mathbf{P}) \tag{6.13}$$

where $\mathbf{U}$ is a vector of "conserved" variables, $\mathbf{F}^i$ are the fluxes, $\mathbf{S}$ is a vector of source terms, and $\mathbf{P}$ is the vector of primitive variables. Explicitly, these are

$$\mathbf{P} = \left[\rho, \mathcal{B}^k, \tilde{u}^i, Y_e, T\right]^T \tag{6.14}$$

$$\mathbf{U}(\mathbf{P}) = \sqrt{-g}\left[\rho u^t, T^t{}_t + \rho u^t, T^t{}_j, B^k, \rho Y_e u^t\right]^T \tag{6.15}$$

$$\mathbf{F}^i(\mathbf{P}) = \sqrt{-g}\left[\rho u^i, T^i{}_t + \rho u^i, T^i{}_j, \left(b^i u^k - b^k u^i\right), \rho Y_e u^i\right]^T \tag{6.16}$$

$$\mathbf{S}(\mathbf{P}) = \sqrt{-g}\left[0, T^\kappa{}_\lambda \Gamma^\lambda{}_{t\kappa} + \mathcal{Q} u_t, T^\kappa{}_\lambda \Gamma^\lambda{}_{j\kappa} + \mathcal{Q} u_i, 0, \mathcal{R}\right]^T \quad , \tag{6.17}$$

where g is the determinant of the metric, $\Gamma^\lambda{}_{\mu\kappa}$, is the metric's affine connection, T is the temperature, and $B^i = \mathcal{B}^i/\alpha = {}^*F^{it}$ is the magnetic field.

The primitive velocity is the flow's 4-velocity projected into a frame moving orthogonal to the space-like hypersurface:

$$\tilde{u}^\mu = \left(\delta^\mu{}_\nu + n^\mu n_\nu\right) u^\nu \tag{6.18}$$

which only has spatial coefficients

$$\tilde{u}^i = u^i + \alpha\gamma g^{ti} \quad , \tag{6.19}$$

where $\alpha = 1/\sqrt{-g^{tt}}$ is the lapse function, $\beta^i = -g^{ti}/g^{tt}$ is the shift function, $\gamma = \alpha u^t$ is the Lorentz factor, and n^μ is the 4-velocity of the orthogonal frame: $n_\mu = [-\alpha, 0, 0, 0]$ and $n^\mu = [1/\alpha, -\beta^i/\alpha]^T$. Defining a fluid three-velocity $v^i = \tilde{u}^i/\gamma$, it can be shown that $\gamma = 1/\sqrt{1 - v^2}$, where $v^2 = v_i v^i$.

6.3.2 Implementation of a tabulated EOS in HARM3D+NUC

In the following section, we describe the implementation of a tabulated EOS in HARM3D+NUC.

The tables and routines for interpolating tabulated quantities are provided by[9] O'Connor & Ott (2010) and da Silva Schneider et al. (2017). The finite-temperature tables give thermodynamic variables, including, for example, the sound speed, and the chemical potentials of the nucleons, electrons/positrons and neutrinos/anti-neutrinos, as a function of the temperature (T), the electron fraction (Y_e), and the rest-mass density (ρ). The linear interpolation routines are provided by O'Connor & Ott (2010) and da Silva Schneider et al. (2017).

The tables consider an interpolation between a single nucleus approximation (SNA) in the high density regime and nuclear statistical equilibrium (NSE) of several nucleides in the low density regime. The SNA is composed of free nucleons, electrons, positrons, $\alpha-$particles, and photons. In the high density regime, nuclei are included using the liquid drop model. The regimes are smoothly interpolated. Using the tables, we have the advantage that the nuclear binding energy release due to recombination

[9]The link to the tabulated EOS is the following: *https://stellarcollapse.org/SROEOS*, and the link to the interpolation routines is: *https://bitbucket.org/zelmani/eosdrivercxx/src*

energy from the α-particles is included.

There are three main calls to the EOS in HARM3D+NUC:

- We call the EOS when setting the characteristic velocity in order to solve the Riemann problem (Gammie et al. 2003a). The wave velocities depend on the relativistic sound speed (Gammie et al. 2003a), which can be interpolated directly from the tables.

- We replaced the primitive variable $u = \rho\epsilon$ with the temperature as a reconstructed variable, which makes the interpolation of the pressure faster as all independent variables are known and can be used to perform the interpolation immediately.. This means that we call the EOS to obtain the primitive energy density u after we update ρ, T, and Y_e from the conservation equations.

- We call the EOS repeatedly when converting from conserved variables to primitive variables.

Our implementation of a tabulated EOS into the conserved to primitive variables routine in HARM3D+NUC follows Siegel et al. (2018).

Primary recovery: 3d routine

The primary recovery routine follows a 3-parameter root-finding method similar to ones implemented in Cerdá-Durán et al. (2008); Siegel et al. (2018). We call this routine the '3d' routine. For this routine, we reduce the GRMHD equations into three

equations that have three unknowns, allowing us to solve the following system:

$$\tilde{Q}^2 = \left(1 - \frac{1}{\gamma^2}\right)(\mathcal{B}^2 + W)^2 - \frac{(Q_\mu \mathcal{B}^\mu)^2(\mathcal{B}^2 + 2W)}{W^2} \tag{6.20}$$

$$Q_\mu n^\mu = -\frac{\mathcal{B}^2}{2}\left(2 - \frac{1}{\gamma^2}\right) + \frac{(Q_\mu \mathcal{B}^\mu)^2}{2W^2} - W + P(\rho, Y_e, T) \tag{6.21}$$

$$\epsilon = \epsilon(\rho, Y_e, T) \quad . \tag{6.22}$$

Using these equations, we perform Newton-Raphson iterations until we obtain sufficiently accurate values for the independent variables γ, T and W. Here $Q_\mu = -n_\nu T^\nu_\mu = \alpha T^t_\mu$, W is related to the specific enthalpy through $W = h\rho\gamma^2$,

$\tilde{Q}^\mu = j^\mu{}_\nu Q^\nu$, $j_{\mu\nu} = g_{\mu\nu} + n_\mu n_\nu$, and P is the pressure interpolated from tables.

Backup recovery 1: 2d routine

We also implemented backup routines that recover the conserved variables. One of them follows an optimized version of the "2d" method of Noble et al. (2006a). We call this routine the '2d' routine. In this routine, the independent variables are W and v^2, found using equations (6.20-6.21). The previous time step's set of primitive variables are used as initial guesses to the Newton-Raphson procedure. As was done in Siegel et al. (2018), we obtain the pressure and the temperature for each W and v^2. This is done by first constructing the specific enthalpy: $h = W/(\gamma^2\rho)$, which can also be constructed with quantities from the EOS tables: $h(\rho, T, Y_e)$. Then, with the density, the electron fraction and the specific enthalpy, we perform a Newton-Raphson method to obtain the temperature from the tables, solving the equation: $h = h(\rho, T, Y_e)$. Note

that this inversion is time expensive, which is why this routine is slower than the 3d routine.

Backup recovery 2: 2d 'safe-guess' routine

If there is non-convergence for this backup routine, we include an initial 'safe guess' as described in Cerdá-Durán et al. (2008). We call this routine the '2d safe guess' routine. In this scenario, we use the upper limits of the EOS table to obtain the maximum thermodynamical quantities:

$$\rho_{\rm max} = D, \tag{6.23}$$

$$T_{\rm max} = T_{\rm max,tables}, \tag{6.24}$$

$$P_{\rm max} = P(\rho_{\rm max}, Y_e, T_{\rm max}) \quad . \tag{6.25}$$

Were D is the density measured in the orthogonal frame:

$$D \equiv -\rho n_\mu u^\mu = \gamma\rho \quad . \tag{6.26}$$

Then we can estimate the initial 'safe guess' for the root-finding procedure:

$$\gamma_{\rm guess} = \gamma_{\rm max} = 50, \tag{6.27}$$

$$W_{\rm guess} = Q_\mu n^\mu + P_{\rm max} - \frac{\mathcal{B}^2}{2} \quad . \tag{6.28}$$

Backup recovery 3: 2d dog leg routine

If the 'safe guess' option does not converge, this routine includes a backup root-finding method: a trust-region, dog leg routine that is more robust than a Newton-Raphson (Press et al. 1992; Powell 1968). We call this routine the '2d dog leg' routine.

Backup recovery 4: 'Palenzuela' routine

If all else fails, we use the routine described in Palenzuela et al. (2015). This routine solves a one-dimensional equation using the Brent method. In this routine, called 'Palenzuela', the independent variable is a rescaled variable

$$x_{\rm pal} \equiv \frac{\rho h \gamma^2}{\rho \gamma} \ . \tag{6.29}$$

We use the auxiliary rescaled variables:

$$q_{\rm pal} \equiv \frac{-(Q_\mu n^\mu + D)}{D} \quad , \quad r_{\rm pal} \equiv \frac{\tilde{Q}^2}{D^2} \ , \tag{6.30}$$

$$s_{\rm pal} \equiv \frac{\mathcal{B}^2}{D} \quad , \quad t_{\rm pal} \equiv \frac{Q_\mu \mathcal{B}^\mu}{D^{3/2}} \ . \tag{6.31}$$

The independent variable should be bracketed between:

$$1 + q_{\rm pal} - s_{\rm pal} > x_{\rm pal} > 2 + 2q_{\rm pal} - s_{\rm pal} \ . \tag{6.32}$$

The method uses an initial guess for $x_{\rm pal}$ from the previous time step, and gets approximate quantities. Using them, it updates $x_{\rm pal}$ and iterates again until convergence is

reached. The method is the following (where approximate quantities will be denoted by a hat):

We obtain an approximate Lorentz factor $\hat{\gamma}^{-2}$:

$$\hat{\gamma}^{-2} = 1 - \frac{x_{\rm pal}^2 r_{\rm pal} + (2x_{\rm pal} + s_{\rm pal})t_{\rm pal}^2}{x_{\rm pal}^2 (x_{\rm pal} + s_{\rm pal})^2} \ . \tag{6.33}$$

With that, we can estimate:

$$\hat{\rho} = \frac{D}{\hat{\gamma}} \tag{6.34}$$

and an approximate specific energy:

$$\hat{\epsilon} = \hat{\gamma} - 1 + \frac{x_{\rm pal}}{\hat{\gamma}}(1 - \hat{\gamma}^2) + \hat{\gamma}\left(q_{\rm pal} - s_{\rm pal} + \frac{t_{\rm pal}^2}{2x_{\rm pal}^2} + \frac{s_{\rm pal}}{2\hat{\gamma}^2}\right) \ . \tag{6.35}$$

A call to the EOS will give the pressure $\hat{P}(\hat{\rho}, \hat{\epsilon}, Y_e)$, and with all those approximate quantities, we can solve for $x_{\rm pal}$ using the Brent method by solving:

$$0 = f(x_{\rm pal}) = x_{\rm pal} - \hat{\gamma}\left(1 + \hat{\epsilon} + \frac{\hat{P}}{\hat{\rho}}\right) \ . \tag{6.36}$$

We repeat the estimation of all the hat quantities until the solution for $x_{\rm pal}$ converges.

6.3.3 Neutrino leakage scheme

In the following section, we describe how we implemented a leakage scheme that takes into account the heating/cooling due to neutrinos, as well as how their emission and absorption affect the electron fraction. This leakage scheme is suited to describe

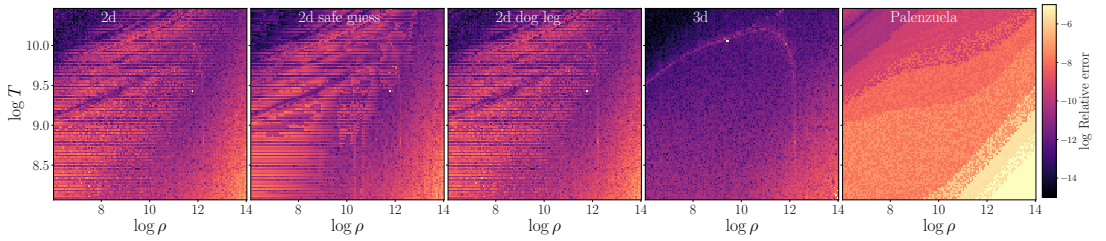

Figure 6.1: Relative error comparing primitive variables created from a grid of density and temperature after we performed the conversion from conserved variables to primitive variables. The primitive variables were created with $Y_e = 0.1$, the Lorentz factor $\gamma = 2$, $\log \frac{P_{\rm mag}}{P_{\rm gas}} = -5$, and a Minkowski metric. We perturbed them by 5% and then recovered them using our conserved to primitive routines. The error is calculated by summing over the relative error of each primitive variable compared to the original. We did this for 2^{14} points in the shown range. The 2d routines failed only once, the 3d routines failed 11 times, and the Palenzuela routine did not fail in this range. Density is in units of g/cm^3, and temperature is in units of Kelvin. Here we compare different routines, described in the text.

the contribution of neutrinos to the composition, and energy.

Rates

The scheme calculates the absorption/emission rate as well as the energy loss rates due to neutrinos. We use these rates in the source terms of Eq. (6.2) and Eq. (6.5). The scheme uses energy-averaged quantities.

Like Ruffert et al. (1996); Galeazzi et al. (2013); Siegel & Metzger (2018), we consider the following neutrino reactions, each with their own absorption/emission rate (which has units of cm^{-3}s^{-1}) and the energy loss rate rate due to neutrinos (with units of erg cm^{-3}s^{-1}):

- Charged β-process with $\mathcal{R}^{\beta}_{\nu_i}$ and $\mathcal{Q}^{\beta}_{\nu_i}$:

$$e^- + p \rightarrow n + \nu_e \tag{6.37}$$

$$e^+ + n \rightarrow p + \bar{\nu}_e \tag{6.38}$$

- Plasmon decay with $\mathcal{R}^{\gamma}_{\nu_i}$ and $\mathcal{Q}^{\gamma}_{\nu_i}$:

$$\gamma \rightarrow \nu_e + \bar{\nu}_e \tag{6.39}$$

$$\gamma \rightarrow \nu_x + \bar{\nu}_x \tag{6.40}$$

  where x is the muon and tauon, and in this case, γ corresponds to a photon.

- Electron-positron pair annihilation with $\mathcal{R}^{ee}_{\nu_i}$ and $\mathcal{Q}^{ee}_{\nu_i}$

$$e^- + e^+ \rightarrow \nu_e + \bar{\nu}_e \tag{6.41}$$

$$e^- + e^+ \rightarrow \nu_x + \bar{\nu}_x \ . \tag{6.42}$$

Using the above reactions, we calculate the total number emission in the optically thin regime from species i as (Ruffert et al. 1996):

$$\mathcal{R}_{\nu_i} = \mathcal{R}^{\beta}_{\nu_i} + \mathcal{R}^{\gamma}_{\nu_i} + \mathcal{R}^{ee}_{\nu_i} \tag{6.43}$$

and the total energy loss rate rate in the optically thin regime is:

$$\mathcal{Q}_{\nu_i} = \mathcal{Q}^{\beta}_{\nu_i} + \mathcal{Q}^{\gamma}_{\nu_i} + \mathcal{Q}^{ee}_{\nu_i} \quad , \tag{6.44}$$

where "i" denotes the different neutrino/anti-neutrino flavors: electron, or muon and

tauon.

The total emission/absorption rates and the energy loss rates are given by an interpolation between the diffusive optically thick regime and the transparent optically thin regime (Ruffert et al. 1996):

$$\mathcal{R}^{\rm eff}_{\nu_i} = \mathcal{R}_{\nu_i}\left(1 + \frac{t_{\rm diff}}{t_{\rm emission,\mathcal{R}}}\right)^{-1} \tag{6.45}$$

$$\mathcal{Q}^{\rm eff}_{\nu_i} = \mathcal{Q}_{\nu_i}\left(1 + \frac{t_{\rm diff}}{t_{\rm emission,\mathcal{Q}}}\right)^{-1} . . \tag{6.46}$$

Here the diffusion timescale is given by:

$$t_{\rm diff} = \frac{D_{\rm diff}\tau^2}{c\kappa_{\nu_i}} , \tag{6.47}$$

where $D_{\rm diff} = 6$ (Rosswog & Liebendörfer 2003; O'Connor & Ott 2010; Siegel & Metzger 2018) and τ is the optical depth, and κ_{ν_i} the energy averaged opacity (in units of $\rm cm^{-1}$) of ν_i. The absorption/emission and energy loss timescales are $t_{\rm emission,\mathcal{R}} = \mathcal{R}_{\nu_i}/n_{\nu_i}$, with n_{ν_i} being the neutrino number density (at chemical equilibrium), and $t_{\rm emission,\mathcal{Q}} = \mathcal{Q}_{\nu_i}/\varepsilon_{\nu_i}$, with ε_{ν_i} being the neutrino energy density. In the optically thick regime, the neutrino loss rate is less than the diffusion time, which results in $\mathcal{R}^{\rm eff}_{\nu_i} = n_{\nu_i}/t_{\rm diff}$ and $\mathcal{Q}^{\rm eff}_{\nu_i} = \varepsilon_{\nu_i}/t_{\rm diff}$, whereas in the optically thin regime, we recover the rates from equation (6.43) and (6.44). The rates for the muon and tauon neutrinos/anti-neutrinos estimated in Ruffert et al. (1996) take into account all four of those species. We also note that several quantities, including the chemical potentials, are obtained from EOS table interpolation.

Optical depth

The transition between the two regimes will be set by the optical depth τ_{ν_i}, which is also needed to obtain the diffusion timescale. In order to get the optical depth, we consider the following reactions as the source of neutrino opacity:

$$\nu_e + n \rightarrow p + e^- \tag{6.48}$$

$$\bar{\nu}_e + p \rightarrow n + e^+ \tag{6.49}$$

$$\nu_i + p \rightarrow \nu_i + p \tag{6.50}$$

$$\nu_i + n \rightarrow \nu_i + n. \tag{6.51}$$

The rates are obtained from Ruffert et al. (1996). Electron scattering is neglected.

To calculate the optical depth, we follow Neilsen et al. (2014); Siegel & Metzger (2018), where a local approach is used instead of a global calculation. For this scheme, we iterate over the different pathways that the neutrino should explore in order to obtain the smallest optical depth from the cell in question. We estimate the optical depth of each cell by summing over the optical depth needed to get to a neighboring cell (already computed in the previous iteration) and the minimum depth to each neighbor. We estimate the minimum resistance path by obtaining the minimum optical depth from

each cell to each of the neighboring cells, as:

$$\min\left(\tau_{\nu_i,\text{neighbor}} + \bar{\kappa}_{\nu_i}(g_{kj}dx^k dx^j)^{1/2}\right) \tag{6.52}$$

where $\tau_{\nu_i,\text{neighbor}}$ is the optical depth needed to get to the neighboring cell, $\bar{\kappa}_{\nu_i}$ is the average opacity between the cell and its neighbor, and $(g_{kj}dx^k dx^j)^{1/2}$ is the average distance to the neighboring cell.

One iteration of this equation is going to indicate the path of least resistance of the neutrino to one of its neighbors. The next iteration will show the path to the next neighbor, and so on. By doing several iterations of the minimum optical depth path, we can obtain the path of minimum resistance that the neutrino will follow, which will lead us to the final optical depth. We first need to do several iterations, corresponding to a few times the number of cells in the longest direction, in order to trace a path to the edge of the domain and calculate the final optical depth. In our implementation, the initial optical depth is calculated by doing $20N_{\max}$ iterations, where $N_{\max}$ is the maximum number of cells in each direction, independent of resolution. After the initial calculation, which has a fixed number of iterations, we impose a convergence criterion in order to minimize the number of iterations. In order to converge, we set conditions on the difference between iteration $k-1$ and k:

$$R_{\text{change},\tau}(k) \equiv \frac{|\sum \tau_{k-1} - \sum \tau_k|}{\sum \tau_{k-1}} < \epsilon_1 \tag{6.53}$$

or

$$\frac{|R_{\text{change},\tau}(k-1) - R_{\text{change},\tau}(k)|}{R_{\text{change},\tau}(k-1)} < \epsilon_2 \tag{6.54}$$

where $\sum \tau_k$ is the sum of all the optical depths in the grid at iteration k, and ϵ_1 and ϵ_2 are parameters that we choose to be $\epsilon_1 = 10^{-4}$ and $\epsilon_2 = 10^{-3}$, respectively. Only a few iterations are needed for convergence after the initial guess.

6.4 Validation tests for the tabulated EOS

In this section, we describe the tests performed to validate the implemented EOS tables.

6.4.1 Testing the conserved to primitive variables routine

In order to validate the routines that transform the conserved variables into primitive variables with tabulated EOS, we created primitive variables out of a grid of density and temperature values within the EOS table. The magnetic field was set randomly to be either aligned or anti-aligned with the velocity vector. The magnitude of the magnetic field was set to be such that: $b^2/2 = \left(\frac{P_{\text{mag}}}{P_{\text{gas}}}\right) P_{\text{gas}}$, where $(P_{\text{mag}}/P_{\text{gas}})$ is set as a parameter, P_{mag} is the magnetic pressure, and P_{gas} is the gas pressure. We then obtained a set of conserved variables based on these primitives. The true primitives were then varied by randomly adding or subtracting a 5% perturbation to each primitive. This test is based on Siegel et al. (2018).

We then used these primitives as initial guesses for the various routines that transform the conserved variables to primitive variables and compared the resultant

solution to the original.

We show the error we obtained for all primitive variables in Figure 6.1. It can be seen that the recovery error is low. Additionally, the figure shows that the 3d method is less robust, but more accurate, which is the reason it is set as the primary routine. The different 2d methods, and the 'Palenenzuela' routine are more robust, but less accurate (and slower) than the 3d method, so they serve better as backup routines.

6.4.2 Torus in hydrostatic equilibrium

To test the EOS implementation, we simulated a non-magnetized torus that is in hydrostatic equilibrium with no leakage scheme, following Fishbone & Moncrief (1976).

Figure 6.2 shows the 3d hydrodynamical evolution of a torus constructed to be in hydrostatic equilibrium with a tabulated EOS without neutrino cooling. There are perturbations particularly near the BH due to accretion onto the BH, but the density is low in those regions. As can be seen from the figure, the torus remains in hydrostatic equilibrium throughout the simulation.

Initial conditions inside the torus

The specific enthalpy inside the torus is implemented via Equation (3.6) of Fishbone & Moncrief (1976), but adding $\ln h_{\rm min}$ to the integration constant (see Section 6.4.2). By construction, the torus is in hydrostatic equilibrium with the ambient atmosphere. We also set the torus to be isentropic, and have uniform electron fraction. Given a specific entropy $s_{\rm disk}$, a specific enthalpy given by Fishbone & Moncrief (1976),

and an electron fraction $Y_{e,\text{disk}}$), the temperature and density of the disk are found by solving the following equations:

$$s_{\text{disk}} = s(\rho, T, Y_e) \tag{6.55}$$

$$h = h(\rho, T, Y_e) \tag{6.56}$$

where s is the specific entropy.

Atmosphere

In the classical torus, the boundaries of the torus are defined where $h = 1$. In the tabulated EOS, though, negative internal energy densities are allowed since the internal energy per nucleon is measured relative to the free neutron rest mass energy. In this case, the minimum specific enthalpy is not restricted to 1, but rather it can be $1 > h_{\text{min}} > 0$, where h_{min} is the specific enthalpy from the table given the atmospheric density, and the disk's electron fraction and specific entropy. Thus, we set the torus boundary to be where $h = h_{\text{min}}$. For the background atmosphere, we set the minimum atmospheric density ρ_{atm} as a parameter. Then we find the minimum specific enthalpy by doing a table inversion and finding $h_{\text{min}} = h(\rho_{\text{atm}}, s_{\text{disk}}, Y_{e,\text{disk}})$. We also find the atmospheric temperature by doing a table inversion $T_{\text{atm}} = T(\rho_{\text{atm}}, s_{\text{disk}}, Y_{e,\text{disk}})$.

The density in the background is set to:

$$\max\left(\rho_{\text{atm}}, \frac{\rho_0}{r^2}\right) \tag{6.57}$$

Where we set ρ_0 as a parameter as well. The background atmosphere temperature is set to:

$$\max\left(T_{\rm atm}, \frac{T_0}{r}\right) , \tag{6.58}$$

where T_0 is a parameter. The power-law dependence is set to provide the background atmosphere with more pressure support so that it does not rapidly accrete onto the BH. This ultimately helps with robustness near the BH, as the low density and low temperature zones with high velocity are where the conserved to primitive routines tend to fail. We note that in the region where there is a power-law dependence, the specific enthalpy is not a constant, whereas once the background atmosphere is set to be constant, everything is thermodynamically consistent because it was constructed with the tabulated EOS tables.We set the electron fraction of the atmosphere to a constant value found by assuming β-equilibrium (where the neutrino chemical potential is zero) at $T_{\rm atm}$ and $\rho_{\rm atm}$.

The units are normalized so that the maximum density in the torus is set to $\rho_{\rm max} = 1$ in code units, which in this case corresponds to $\rho_{\rm max} = 5.4 \times 10^8 {\rm g/cm^3}$ in cgs units. In the simulation we performed, the torus has a constant electron fraction of $Y_e = 0.1$ and a specific entropy of $10 {\rm k_B}$/baryon, where $\rm K_B$ is Boltzmann's constant. The background atmosphere is characterized by $\rho_{\rm atm} = 6000 {\rm g/cm^3}$, $\rho_0 = 3 \times 10^5 {\rm g/cm^3}$, $T_0 = 0.4 {\rm MeV}$. We used the SLy4 table with NSE from da Silva Schneider et al. (2017), and with that table the minimum specific enthalpy for our parameters is set to $h_{\rm min} = 0.9974$ (in code units), and $T_{\rm atm} = 0.0053 {\rm MeV}$. The electron fraction in the atmosphere, given by β-equilibrium, is set to $Y_{e,{\rm atm}} = 0.45$. The boundary conditions are outflow in the

outer radial boundary, reflective in the angular coordinate θ, and periodic in the angular coordinate ϕ. The metric is Kerr-Schild in spherical coordinates for a non-spinning BH.

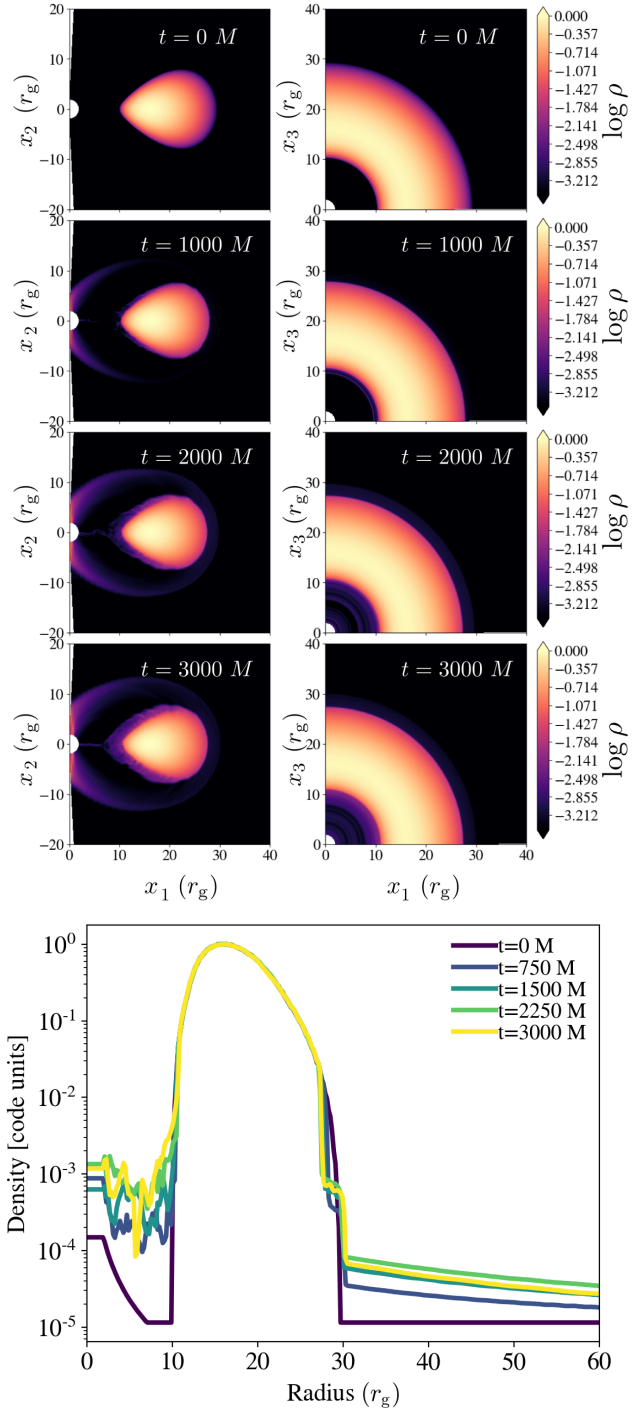

Figure 6.2: *Top* panel: Evolution of a torus in hydrostatic equilibrium with a tabulated EOS and no neutrino leakage scheme.. We show the meridional (Left) and equatorial (Right) cut. The initial conditions are set as described in section 6.4.2. Here x_1, x_2, x_3 correspond to the coordinates x, z, y respectively. *Bottom* panel: Density as a function of radius for different times in the equator.

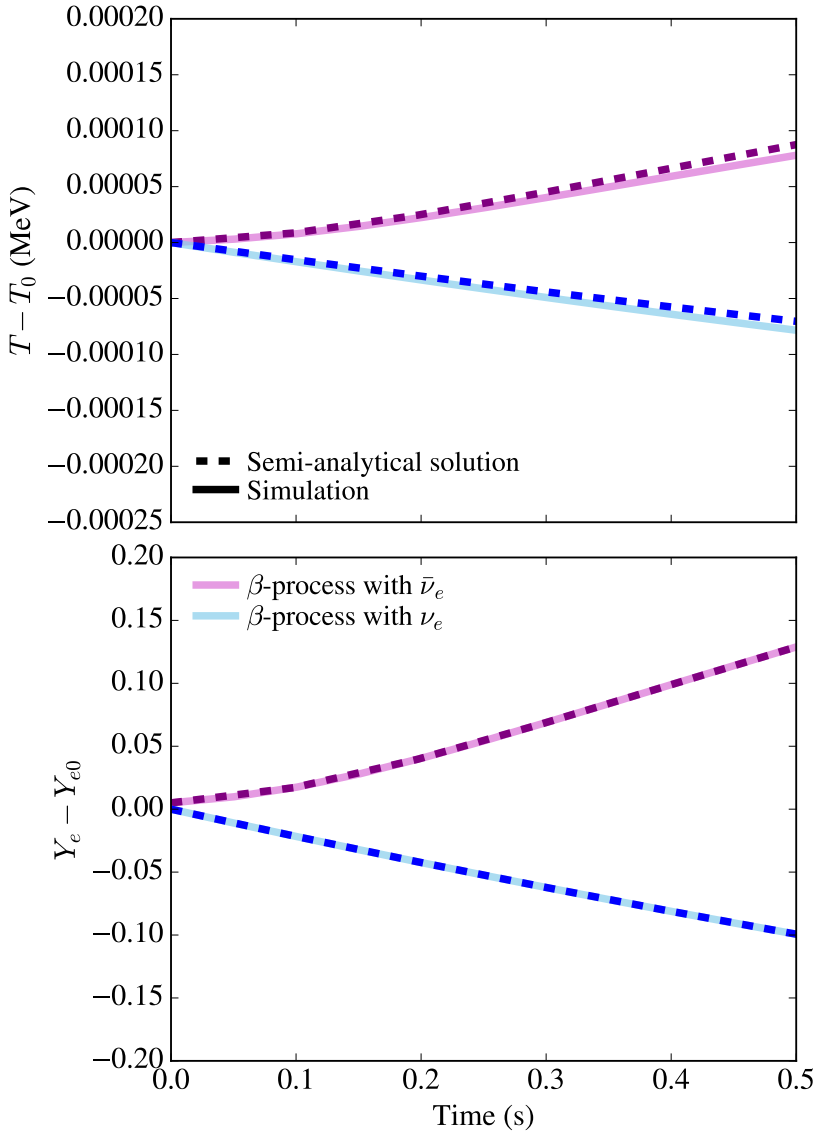

Figure 6.3: Comparison of the semi-analytical solution (dotted line) with the simulation (solid line) for the evolution of the temperature and electron fraction of an isotropic, optically thin gas with constant density.

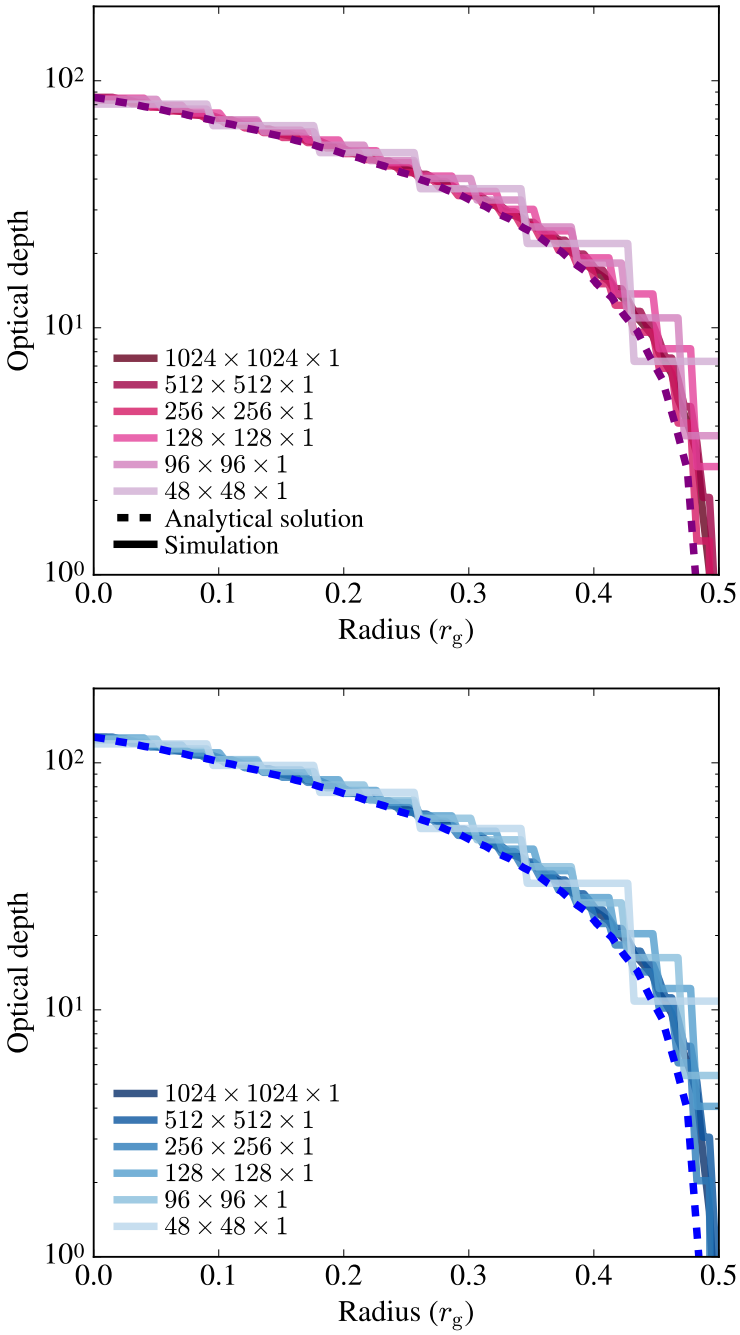

Figure 6.4: Comparison of the analytical solution (dotted line) of the optical depth with simulations (solid line) for different resolutions. The labels indicate the number of cells in each direction. The *Top* panel is the anti-neutrino optical depth, and the *Bottom* panel is the neutrino optical depth.

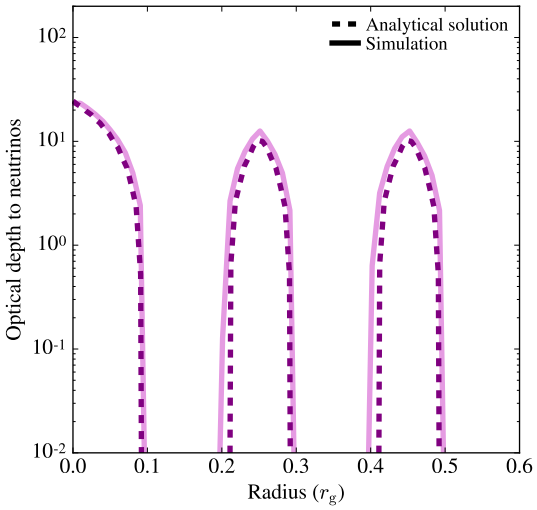

Figure 6.5: Comparison of the analytical solution (dotted line) of the optical depth to neutrinos with simulations (solid line).

6.5 Validation tests for the leakage scheme

In this subsection, we describe how we tested the leakage scheme in the optically thin regime and for finite optical depth.

6.5.1 Testing the optically thin regime

Following Miller et al. (2019a), we tested the leakage scheme in an optically thin regime by considering an isotropic gas of constant density and temperature such that the gas is optically thin to neutrinos. We tested both reactions in the charged $\beta-$process separately where we included only either the neutrinos or the anti-neutrinos.

In this case, the GRMHD equations reduce to:

$$\partial_t T^t{}_t = \mathcal{Q}. \ , \tag{6.59}$$

$$\partial_t Y_e = \mathcal{R}/\rho \ , \tag{6.60}$$

where $\mathcal{R}$ and $\mathcal{Q}$ are the emission/absorption and energy loss rates due to neutrinos or anti-neutrinos of the reactions in $\beta-$process separately. The rates need to be calculated semi-analytically, since they depend on interpolated quantities, such as the degeneracy parameters. We can then solve the equations semi-analytically with a set of initial conditions and compare to simulations. We chose the initial density and temperature such that the medium is optically thin to neutrinos and anti-neutrinos.

For the initial conditions, we used an initial density of 617714g/cm^3 and temperature of 1MeV, chosen so that the medium is optically thin to neutrinos and anti-

neutrinos. We used $Y_{e,0} = 0.5$, $Y_{e,0} = 0.005$ for the electron neutrino and anti-neutrino tests respectively. We used $2 \times 2 \times 1$ number of cells in each direction using a Cartesian grid with Minkowski metric.

In Figure 6.3 we show the comparison between the semi-analytical solution and the simulation for the β-process both for neutrinos and anti-neutrinos. We compare the change in the electron fraction due to the absorption/emission rate, and the change in temperature due to the heating/cooling rate. As can be seen from the figure, HARM3D+NUC is able to recreate the semi-analytical solution.

6.5.2 Testing the optically thick regime

Constant density circular disk

In order to test the optical depth calculation, we simulated a circular disk with uniform density and temperature embedded in an optically thin medium of constant density and temperature. The advantage of this scenario is that we can calculate the opacity inside the circle and then calculate the optical depth analytically. This way we can compare to the simulation. The simulations were performed in 2d, and the domain is $2r_{\rm g}$, where $r_{\rm g} = GM/c^2$ is the gravitational radius. We used a Minkowski metric with spherical coordinates. There are outflow conditions on the radial boundaries. The optical depth in the outer radial boundary was set to zero so that the neutrinos and anti-neutrinos could escape the domain. We simulated an optically thick circular disk that has a constant density of $9.8 \times 10^{13}{\rm g/cm}^3$, an electron fraction of 0.1 and a temperature of 8MeV embedded in an optically thin medium, with a density of $6 \times 10^7{\rm g/cm}^3$, an

electron fraction of 0.5 and a temperature of 0.01MeV. Figure 6.4 shows the optical depth for both the electron neutrino and anti-neutrino for different resolutions. As can be seen from the figure, the initial guess for the optical depth is accurate and the convergence to the solution does not change with resolution. At smaller optical depths, the optical depth is slightly overestimated at lower resolutions, but as the optical depth increases, the solution doesn't depend noticeably on resolution.

Stripes

We can also test the optical depth algorithm by simulating stripes of high density material with low density material in between. In this scenario, it is expected that a neutrino created in the region with high optical depth material will travel to the region with low optical depth and stream freely from the surface. For the simulation, we used $4096 \times 96 \times 1$ cells. The simulations were performed in 2d, and the domain is $1r_{\rm g}$ large in radial extent, where $r_{\rm g} = GM/c^2$ is the gravitational radius. We used a Minkowski metric with spherical coordinates and outflow conditions at the radial boundaries. The optical depth at the outer radial boundary was set to zero so that the neutrinos and anti-neutrinos could escape the domain. We simulated three stripes of material with high optical depth: $\rho = 9.8 \times 10^{13}{\rm g/cm^3}$, $Y_e = 0.1$, $T = 8{\rm MeV}$. In between the stripes, the optically thin gas was initialized to $\rho = 6 \times 10^{7}{\rm g/cm^3}$, $Y_e = 0.5$, and $T = 0.01{\rm MeV}$. The high opacity stripes start at $r = 0r_{\rm g}$, and have a width of $r = 0.1r_{\rm g}$. The next stripes are located in $r = 0.2r_{\rm g}$ and $r = 0.4r_{\rm g}$.

We show the results from this setup in Figure 6.5, where we compare the results

from the simulation with the analytical estimate (length units are in $r_{\rm g}$):

$$\tau_{\rm analytical} = \begin{cases} \int_0^{0.2} \kappa dr & r \leq 0.2 \\ \int_{0.2}^{0.25} \kappa dr & 0.2 \leq r \leq 0.25 \\ \int_{0.25}^{0.35} \kappa dr & 0.25 \leq r \leq 0.35 \\ \int_{0.4}^{0.45} \kappa dr & 0.4 \leq r \leq 0.45 \\ \int_{0.45}^{0.55} \kappa dr & 0.45 \leq r \leq 0.55 \end{cases} \tag{6.61}$$

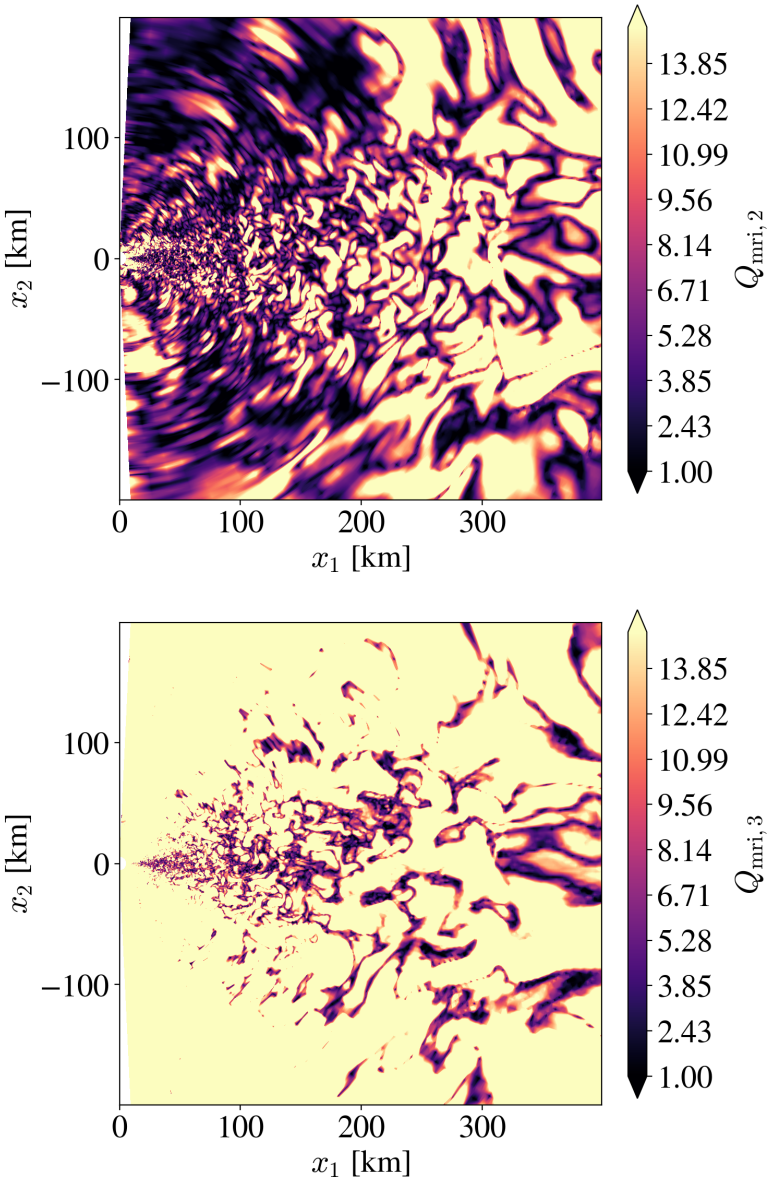

Figure 6.6: Shown is a meridional cut of the MRI quality factors $Q_{\mathrm{mri},2}$ and $Q_{\mathrm{mri},3}$ at 114ms, where the subscripts for $Q_{\mathrm{mri},2}$, $Q_{\mathrm{mri},3}$ correspond to the coordinates θ, ϕ respectively.

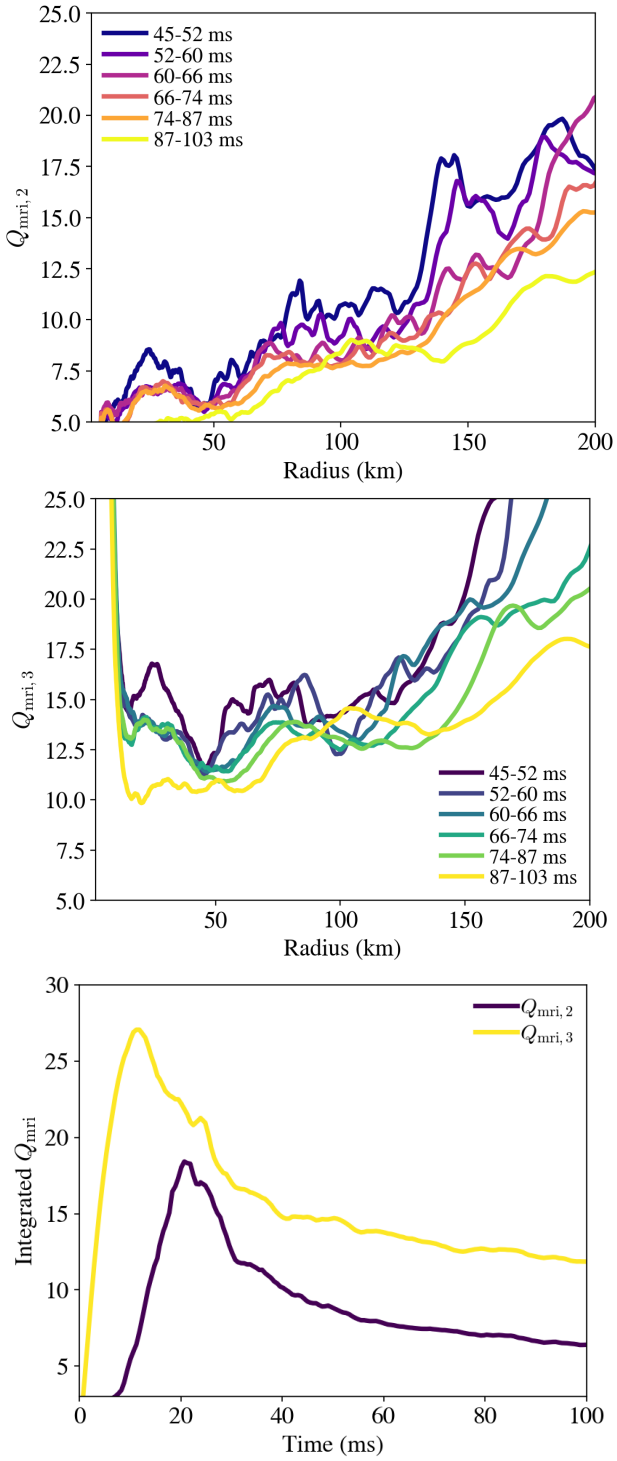

Figure 6.7: *Top* and *Middle* panel: Shell-integrated mass-weighted quality factors as a function of radius, averaged over different epochs of time. *Bottom* panel: Mass-weighted quality factors integrated over angles and radii that are less than 150km: $\int_{0\mathrm{km}}^{150\mathrm{km}} \int\int Q_{\mathrm{mri}} \rho \sqrt{-g} dr d\phi d\theta / \int_{0\mathrm{km}}^{150\mathrm{km}} \int\int \sqrt{-g} \rho dr d\phi d\theta$.

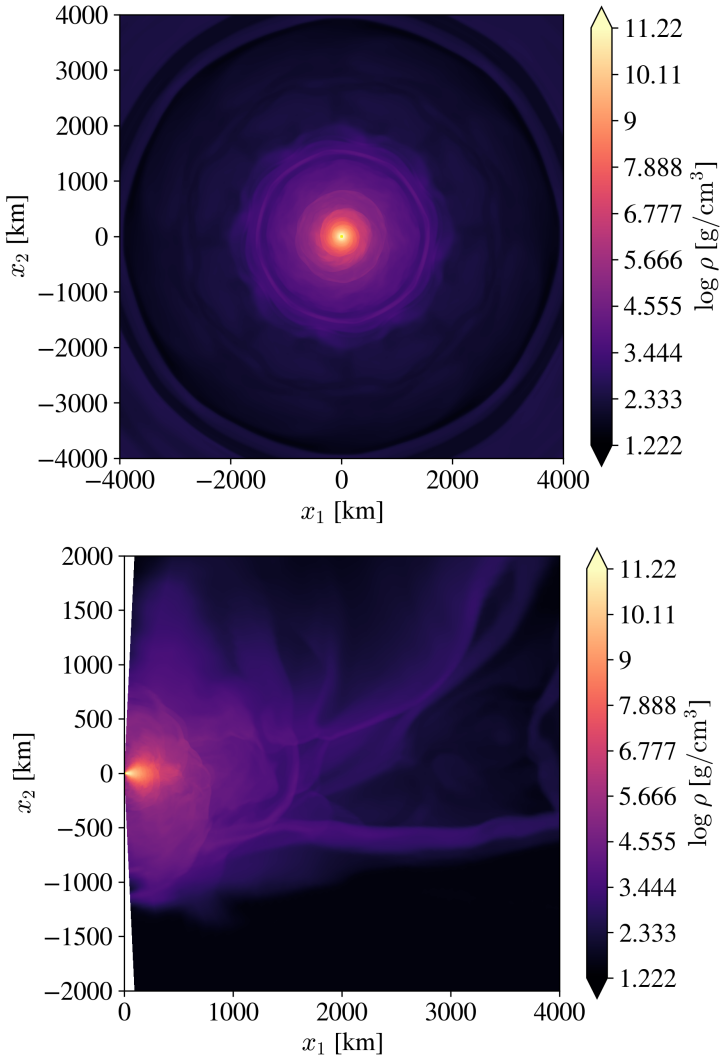

Figure 6.8: Density of a magnetized torus including the impact of neutrinos at 114ms. Shown is an equatorial cut (*top* panel) and a meridional cut (*bottom* panel).

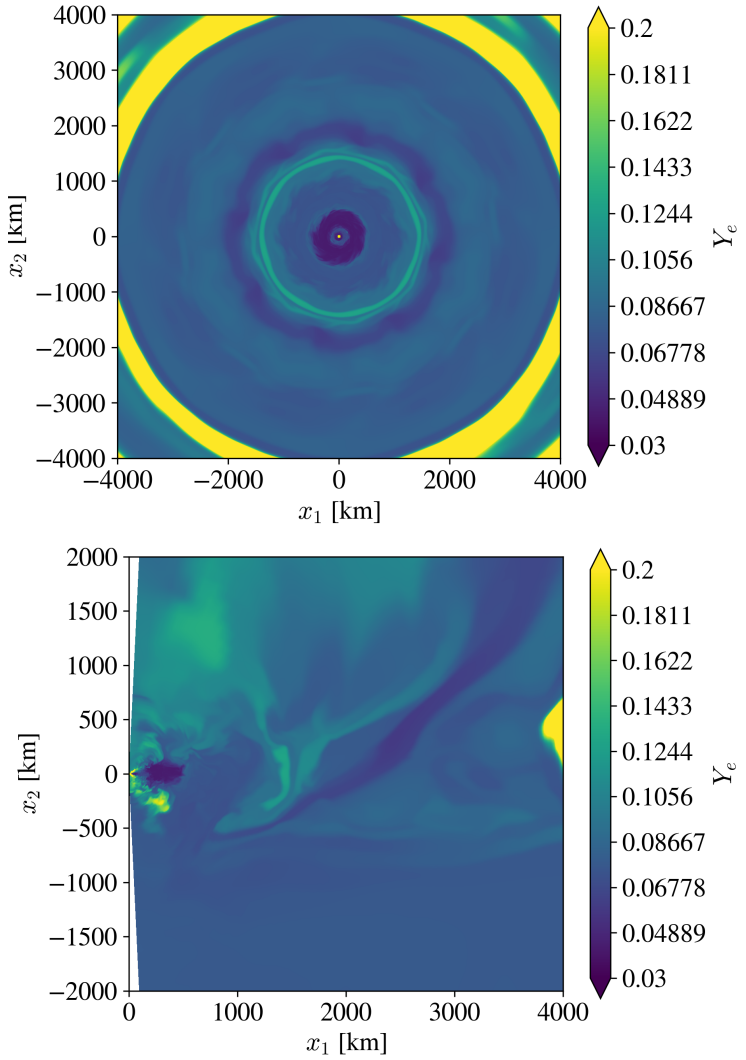

Figure 6.9: Electron fraction of a magnetized torus including the impact of neutrinos at 114ms. Shown is an equatorial cut (*top* panel) and a meridional cut (*bottom* panel).

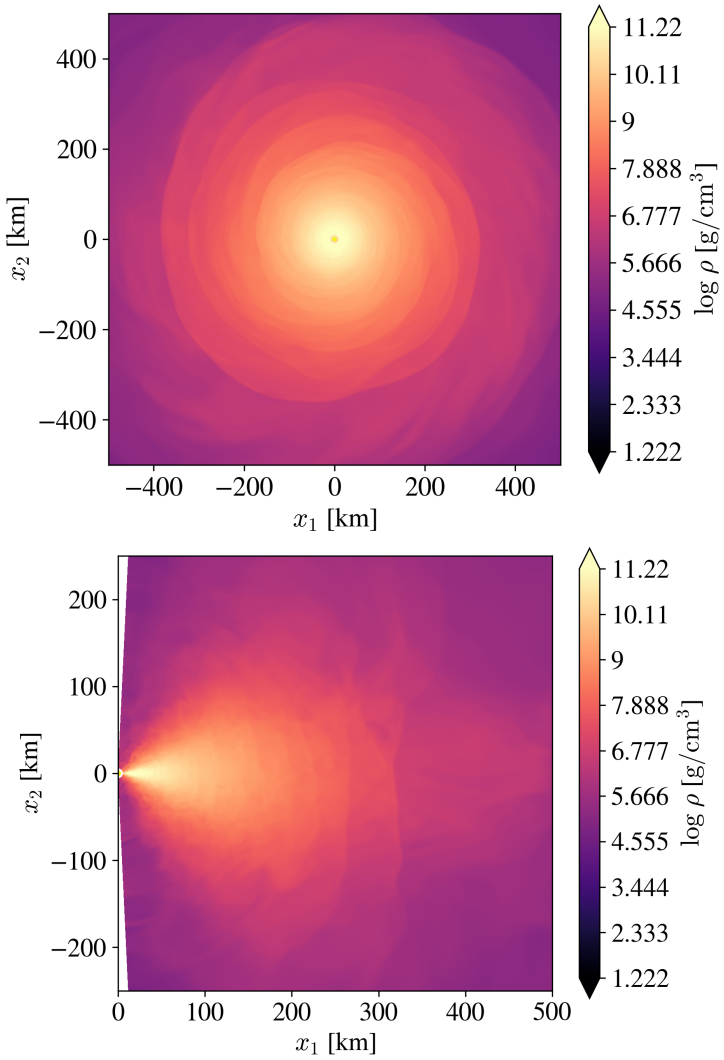

Figure 6.10: Zoomed in version of the density of a magnetized torus including the impact of neutrinos at 114ms. Shown is an equatorial cut (*top* panel) and a meridional cut (*bottom* panel).

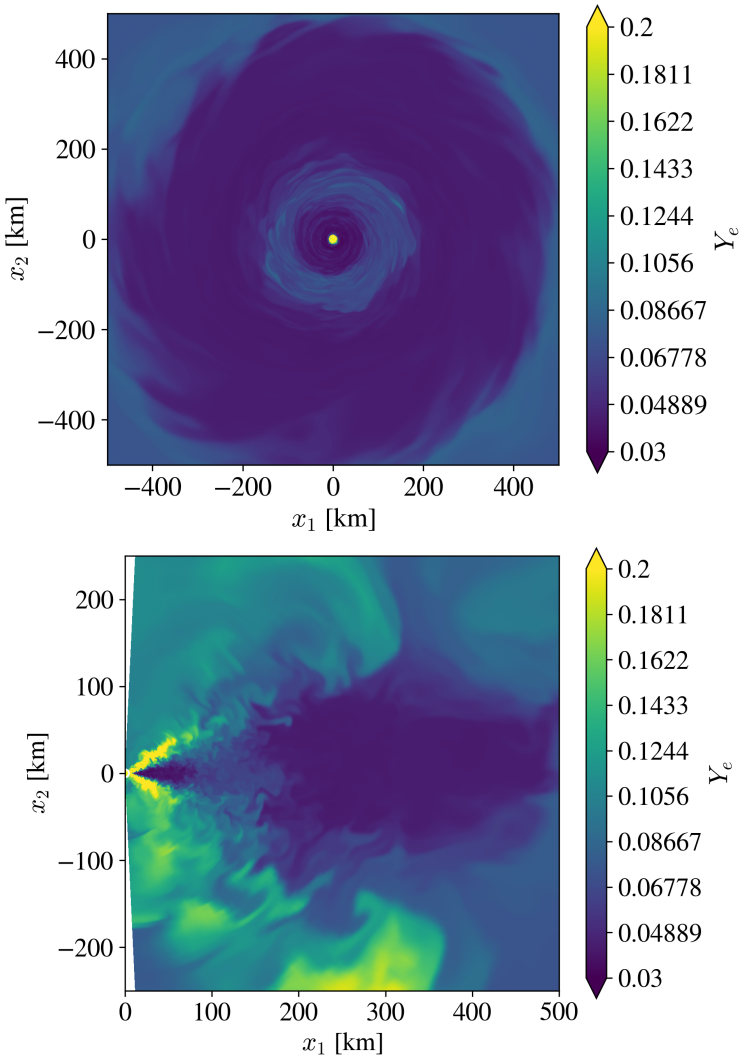

Figure 6.11: Zoomed in version of the electron fraction of a magnetized torus including the impact of neutrinos at 114ms. Shown is an equatorial cut (*top* panel) and a meridional cut (*bottom* panel).

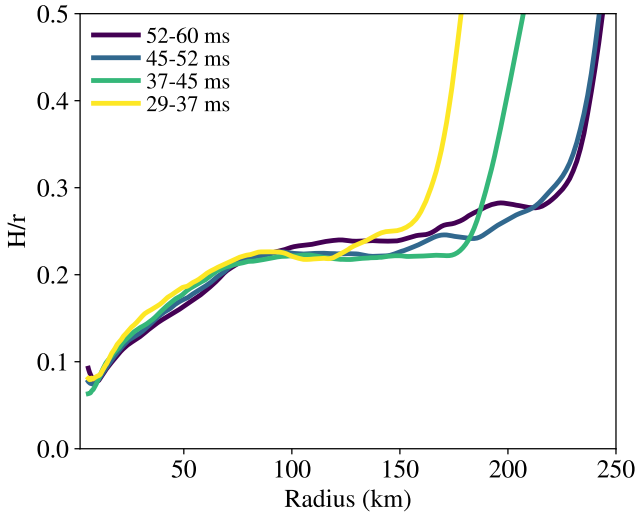

Figure 6.12: Shown is the geometrical thickness (H/r) of the disk, as a function of radius. The thickness is averaged between the indicated time in the legend.

6.6 Magnetized disk

In this section, we apply our new code HARM3D+NUC to a magnetized torus in 3d that approximates a post-merger disk. We use both the tabulated EOS and the leakage scheme in this test.

6.6.1 Initial conditions

The initial conditions inside the torus follow a similar setup to that of section 6.4.2, but with the addition of a poloidal magnetic field. In order to start with a magnetic field devoid of magnetic monopoles, we first set the vector potential to a prescribed distribution and calculate its curl using a finite difference operator compatible with our constrained transport method (see Zilhão & Noble 2014, for further details). Our poloidal magnetic field distribution results from a vector potential with only one

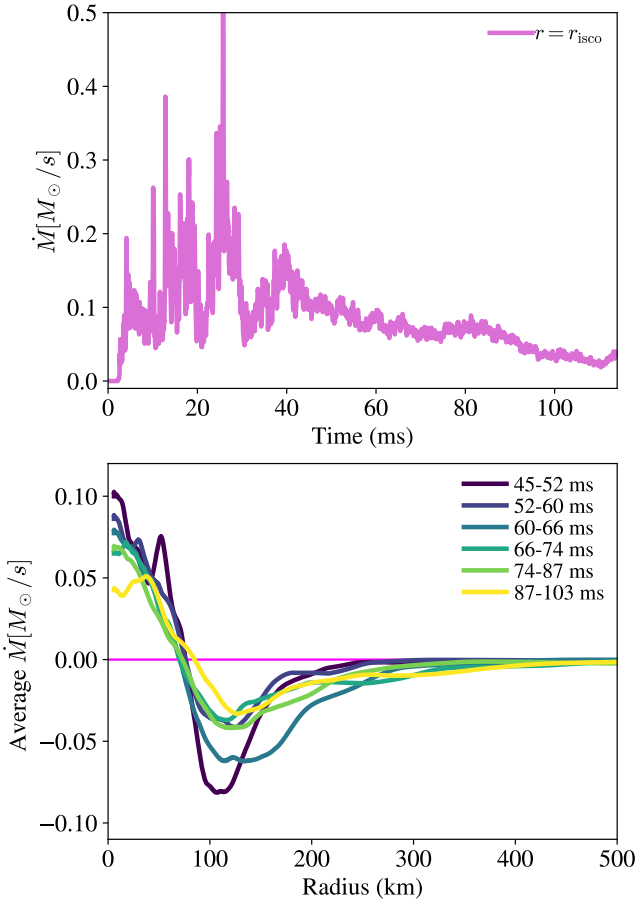

Figure 6.13: *Top* panel: Mass accretion rate onto the innermost stable circular orbit (ISCO) of the BH as a function of time. *Bottom* panel: Average mass accretion rate as a function of radius. We averaged the mass accretion rate between the times indicated in the legend.

non-zero component:

$$A_\phi = \max\left(\overline{\rho}/\rho_{\rm max} - \rho_{0,\rm mag}\ , 0\right) \tag{6.62}$$

where $\overline{\rho}$ is the average density at that position, and $\rho_{\rm max} = 1.66 \times 10^{11}{\rm g/cm^3}$ is the maximum density of the torus. We set $\rho_{0,\rm mag} = 0.2$ in code units, which corresponds to $\rho_{0,\rm mag} = 3.33 \times 10^{10}{\rm g/cm^3}$. Then we build the magnetic field with the vector potential and normalize its magnitude such that the ratio of the integrated gas pressure

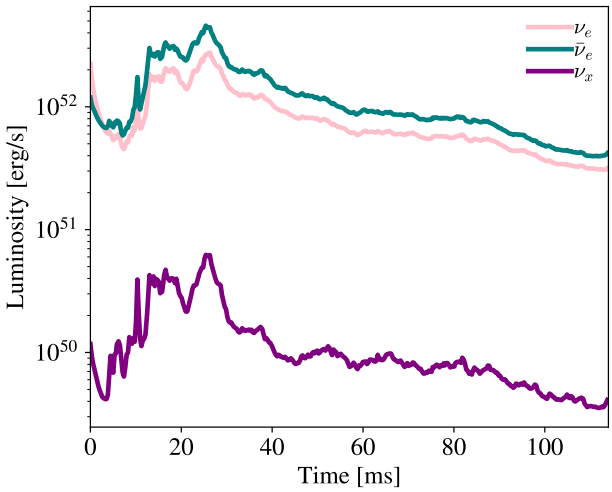

Figure 6.14: Luminosity due to the different neutrino species as a function of time.

to integrated magnetic pressure is 100. Inside the disk, the matter is set to be neutron rich, $Y_e = 0.1$. The treatment of the atmosphere is the same as in section 6.4.2, except the density scales as $r^{-3/2}$. In the atmosphere, the electron fraction is set to its value in β-equilibrium, where the chemical potential of the neutrinos is set to zero. We show the parameters used in Table 6.1.

The simulations were performed in 3d on a grid designed to focus more cells about the equator and towards the black hole horizon. We use the same grid as defined in Noble et al. (2010) but with different parameters. The azimuthal grid spacing is uniform. The logarithmic radial grid is such that $\Delta r/r$ is fixed and the $i^{\rm th}$ cell center is located at:

$$r_i = r_{\rm min} \exp\left[(i + 1/2) \log_{10}\left(r_{\rm max}/r_{\rm min}\right)/N_r\right] , \tag{6.63}$$

with $r_{\rm min} = 1.303 r_{\rm g}$, $r_{\rm max} = 2000 r_{\rm g}$, and $i \in [0, N_r - 1]$. The θ grid uses a high-order

Parameter	Value
Disk radius of maximum pressure	$9r_{\rm g}$
Disk inner radius	$4r_{\rm g}$
Mass of disk	$0.03M_{\odot}$
Y_e in the disk	0.1
Specific entropy in the disk	7 $k_{\rm b}$/baryon
β	100
BH spin	0.9375
BH mass	$3M_{\odot}$
Specific enthalpy at boundary	0.9977 [code units]
Temperature at radius of maximum pressure	4.4 MeV

Table 6.1: Parameters used in the simulation.

polynomial function to provide a nearly uniform grid spacing spacing near the equator:

$$\theta_j = \frac{\pi}{2}\left[1 + (1-\xi)\left(2x_j^{(2)} - 1\right) + \left(\xi - \frac{2\theta_c}{\pi}\right)\left(2x_j^{(2)} - 1\right)^n\right] , \tag{6.64}$$

where ξ is a parameter controlling the severity of the focusing, n is the order of polynomial used in the transformation, θ_c is the opening angle of the polar regions we excise, $x_j^{(2)} \equiv (j+1/2)/N_\theta$, and $j \in [0, N_\theta - 1]$. In our run, we used $\theta_c = \pi 10^{-14}$, $\xi = 0.65$, and $n = 7$. The number of cells per dimension used was $N_r \times N_\theta \times N_\phi = 1024 \times 160 \times 256$.

6.6.2 Scaling tests

We performed scaling tests for this run for 3 different number of processors: 5120, 2560 and 1280 processors. For this setup, the number of time steps in the code per second per processor were: 0.000723, 0.000781, 0.000868 respectively. The difference between 5120 and 1280 processors is around 17%. If we don't include the neutrino leakage scheme but include only a tabulated EOS, for 2560 processors, the number of

steps per second per processor is 0.001328, which makes the leakage 58% slower than only considering the tabulated EOS.

6.6.3 Magnetic turbulence

In order to confirm that we are adequately resolving magnetic turbulence, we display in Figure 6.6 the number of grid cells per wavelength of the fastest growing mode of the magneto-rotational instability (MRI), defined as (Noble et al. 2010; Hawley et al. 2011; Sorathia et al. 2012; Hawley et al. 2013):

$$Q_{\rm mri,x} = \frac{\lambda_{x,\rm mri}}{\Delta_x} \tag{6.65}$$

where $x = \theta, \phi$, Δ_x is the cell size, and the wavelength of the fastest MRI growing mode is:

$$\lambda_{x,\rm mri} = \frac{2\pi}{\Omega} \frac{|b^x|}{\sqrt{\rho h + b^2}} \ . \tag{6.66}$$

As can be seen in Fig 6.7, our grid satisfies the criterion of Sano et al. (2004) everywhere except for later times within $r < 50$km. While our results fail to meet criteria for asymptotic MRI convergence set forth in Hawley et al. (2011), our disk does satisfy $Q_{\rm mri,3} > 10$ everywhere, and $Q_{\rm mri,2} > 6$ for $r \gtrsim 50$km for most of the run. This is because we used the same random perturbations across all MPI processes in the initial conditions. This means that with our resolution the azimuthal direction is periodic in $\pi/8$, and the azimuthal modes with $m < 8$ are not able to grow.

6.6.4 Impact of neutrinos and EOS

Magnetic stresses will transport angular momentum in the disk, heating the gas, which will produce a high velocity outflow (Fernández & Metzger 2013a; Siegel & Metzger 2018). This outflow will be affected by the addition of neutrinos formed through weak reactions. In the midplane, neutrinos will carry significant amounts of energy, which will cool and make the disk geometrically thinner. Another outflow is also expected to occur in the outer regions of the disk due to the release in nuclear binding energy when there is recombination of free nucleons into $\alpha-$particles, which produces enthalpy and unbinds material (Lee et al. 2009; Fernández & Metzger 2013a). In this subsection we show the impact of both the emission of neutrinos and the recombination of free nucleons.

In Figures 6.8 and 6.11 we display the outflows that results from our simulations of a neutrino-cooled magnetized disk at 114 ms. In Figures 6.9 and 6.10 we plot the electron fraction and the density, respectively, at $t = 114$ms. Neutrino cooling is expected to happen in diffusion timescales, which is on the order of milliseconds, much shorter than our evolution timescale. The inner regions of the disk are very neutron rich, confirming the self-regulating phase found in Siegel & Metzger (2017, 2018). In this phase, there is a balance between the neutrino cooling and the heating driven by MHD that self-regulates the electron degeneracy parameter, and the final state is a neutron rich disk (Siegel & Metzger 2017, 2018). We note that, although this new code does not include neutrino absorption in the ejecta, the absorption should modify the electron fraction in the outflow (Just et al. 2021).

In the *top* panel of Figure 6.13 we show the mass accretion rate through the innermost stable circular orbit (ISCO) as a function of time, and show the accretion rate as a function of radius in the *bottom* panel. The outflow can be clearly seen as a negative mass accretion rate at larger radii, as well as a settling of the mass accretion rate as time passes.

In Figure 6.12, we plot the geometrical thickness of the disk, or H/r. We estimated this thickness using the scale height H following Noble et al. (2012):

$$H = \frac{\langle \rho \sqrt{g_{\theta\theta}} \, |\theta - \pi/2| \rangle}{\langle \rho \rangle} \tag{6.67}$$

where $\langle X \rangle$ is the average of the quantity X over a spherical shell:

$$\langle X \rangle = \frac{\int X \sqrt{-g} d\theta d\phi}{\int \sqrt{-g} d\theta d\phi} \ . \tag{6.68}$$

In the deepest regions of the disk, the heating due to MHD turbulence helps create neutrinos/anti-neutrinos, which escape, remove energy, and geometrically thin the disk. Recombination of free nucleons into α-particles releases binding energy, effectively increasing the enthalpy and unbinds material. The effect of recombination is less severe than the geometrically thinning due to neutrino/anti-neutrino losses. This transition can be seen at around 150km.

We may obtain the amount of energy radiated by each species of neutrino and

anti-neutrino as was done in Siegel & Metzger (2018):

$$L_{\nu_i} = \int \alpha\gamma \mathcal{Q}^{\rm eff}_{\nu_i} \sqrt{-g} d^3x \ . \tag{6.69}$$

In Figure 6.14, we show the luminosity for each species. It can be seen that the electron neutrino (and anti-neutrino) dominate the emission over all of the other species of neutrino. The luminosity roughly follows the mass accretion rate as seen in Figure 6.13, as heating from the magnetic stresses ignite the creation of neutrinos/anti-neutrinos. This suggests the radiative efficiency of neutrino/anti-neutrinos emission remains relatively steady.

Our initial conditions are similar (although not identical) to the initial conditions in Siegel & Metzger (2018). They performed 3d simulations of a post-merger accretion disk with a relatively higher specific entropy and lower spin than this simulation. They used Cartesian coordinates, a Helmholtz EOS for relatively low densities, and a neutrino leakage scheme. They evolved the disk for longer times (380 ms). Even though we use a different EOS (Sly4), the disk thickness is qualitatively similar. At the inner regions of the disk, neutrino cooling dominates, whereas at outer regions (at radius higher than around 100km), recombination is responsible for making the disk geometrically thicker. The neutrino/anti-neutrino luminosities are comparable, Siegel & Metzger (2018) has a higher luminosity, but that could be attributed to the difference in the initial disk specific entropy.

As the outflow expands, it will cool, and heavy elements will be created via the $r-$process. We will explore this nucleosynthesis in a future paper.

6.7 Summary

GRMHD simulations of post-merger accretion disks have advanced over the last few years with better treatment of neutrinos and a more realistic EOS. In this paper we present the addition of a neutrino leakage scheme and a tabulated EOS into the computationally efficient, versatile GRMHD code HARM3D. This new addition to HARM3D, called HARM3D+NUC, has the potential to be used in a range of simulations where neutrinos are present. In the paper, we use the new code HARM3D+NUC to simulate an accretion disk resembling the post-merger phase of a binary neutron star, though other applications include collapsars (e.g., Siegel et al. 2019; Miller et al. 2020).

The paper shows how we implemented the tabulated EOS in the conserved variable to primitive variable routines, and the different methods we implemented and tested for performing this inversion. We show that using the 3d primary recovery method is the most accurate and efficient, but least robust, choice which is why we also employ several 2d and 1d backup routines. The leakage scheme is implemented by adding the neutrino/anti-neutrino heating/cooling and emission/absorption terms as source terms in the equations of motion. We describe in detail an approach to obtain the optical depth locally and how we can use a convergence criterion to get the optical depth after a few iterations once the initial guess is made.

We show several tests for our new code. The tabulated EOS is tested by determining the relative error between original primitive variables and the recovered primitive variables. We also test the EOS by performing a simulation of a torus in hydrostatic equilibrium, showing that it stays in hydrostatic equilibrium throughout

the entire simulation. We test the neutrino leakage scheme in the optically thin regime by investigating the $\beta-$process in a constant density gas. We test the optical depth algorithm in a constant density circular disk and a stripes setup.

With our new machinery, we simulate a magnetized high-density torus, which serves as an approximation to the accretion flow after the merger of two neutron stars. Magnetic stresses transport angular momentum from the disk, driving a high velocity outflow. The outflow is affected by both the addition of neutrinos and the nuclear binding energy released from the recombination of nucleons to $\alpha-$particles, which acts to geometrically thicken the disk. Neutrinos will alter the electron fraction of the ejecta especially in the inner regions of the disk, whereas the recombination of nucleons is more prominent in the outer regions of the disk. This highlights the importance of modeling the accretion disk including neutrinos and an EOS that considers this extra unbinding of material due to recombination.

We plan to use the new code to do long-term evolutions of binary neutron star mergers starting from before the neutron stars merge to the evolution of the outflow. Heavy elements should be created via the $r-$process in this outflow as it expands and cools. We plan to use different codes and methods to treat the initial data, pre-merger/merger, and post-merger phases. The initial data for the neutron stars will be constructed using a modified version of LORENE (Gourgoulhon et al. 2016) we have developed. Binaries will be evolved until they merge and eventually form a black hole surrounded by an accretion disk using two GRMHD codes: IllinoisGRMHD (Etienne et al. 2015), and Spritz (Cipolletta et al. 2020). After the remnant has collapsed to

a BH and the numerical metric has stabilized, we will interpolate the MHD primitives and numerical metric into the grid of HARM3D+NUC (López Armengol et al. in prep). After doing the appropriate tensorial transformations from the Cartesian base to the coordinate base of HARM3D+NUC, we will continue the post-merger evolution with HARM3D+NUC.

Chapter 7

Formation of black holes: disappearing stars

7.1 Chapter Abstract

The collapse of a massive star with low angular momentum content is commonly argued to result in the formation of a black hole without an accompanying bright transient. Our goal in this Letter is to understand the flow in and around a newly-formed black hole, involving accretion and rotation, via general relativistic hydrodynamics simulations aimed at studying the conditions under which infalling material can accrete without forming a centrifugally supported structure and, as a result, generate no effective feedback. If the feedback from the black hole is, on the other hand, significant, the collapse would be halted and we suggest that the event is likely to be followed by a bright transient. We find that feedback is only efficient if the specific angular mo-

mentum of the infalling material at the innermost stable circular orbit exceeds that of geodesic circular flow at that radius by at least $\approx 20\%$. We use the results of our simulations to constrain the maximal stellar rotation rates of the disappearing massive progenitors PHL293B-LBV and N6946-BH1, and to provide an estimate of the overall rate of disappearing massive stars. We find that about a few percent of single O-type stars with measured rotational velocities are expected to spin below the critical value before collapse and are thus predicted to vanish without a trace.

7.2 Introduction

Recent evidence for the disappearance of massive stars (Gerke et al. 2015; Adams et al. 2017; Allan et al. 2020) emphasizes the importance of studying the formation of black holes (BHs) and the conditions under which their formation might trigger a bright transient event (Fryer 1999; Woosley & Heger 2006; Lovegrove & Woosley 2013; Smartt 2015; Kochanek 2015; Sukhbold et al. 2016).

It is widely believed that the lack of a bright transient is due to the collapse of a slowly rotating star (Fryer 1999; Smartt 2015). In this scenario, it is commonly assumed that the central engine involves a newly-formed BH accreting material from the collapsing star. The properties of the inflowing material depend on the internal structure of the pre-collapse star and, in particular, its angular momentum (Perna et al. 2014; Lee & Ramirez-Ruiz 2006; Zalamea & Beloborodov 2009). The angular momentum content of the stellar progenitor is a key ingredient as even a small amount of rotation can break spherical symmetry and could produce a centrifugally-supported accretion disk,

which will evolve via internal magneto-hydrodynamic (MHD) stresses (Balbus & Hawley 1991). It has been noted that even in the absence of rotation, convective motions in the outer parts of highly evolved stars could also produce accretion disks (Gilkis & Soker 2014, 2016; Quataert et al. 2019).

Spherical accretion onto BHs is relatively inefficient at producing feedback because the material is compressed but not shocked and thus cannot effectively convert gravitational to thermal energy (Bondi 1952; Blondin & Raymer 2012). This changes dramatically when the infalling material has a critical amount of specific angular momentum (Fryxell & Taam 1988; MacLeod & Ramirez-Ruiz 2015a). When this is the case and if material is injected at large radii, a standard accretion disk will form. Disk material will then gradually spiral inwards as internal MHD stress transports its angular momentum outwards.

Accretion disks naturally produce MHD winds, which carry both bulk kinetic energy and ordered Poynting flux (Tchekhovskoy et al. 2011; McKinney et al. 2012). The energy released by this accretion disk feedback is expected to be significantly larger than the binding energy of the star (Kohri et al. 2005; Yuan & Narayan 2014), which implies that the motion of the inflowing stellar gas can be effectively reversed. If the inflow is halted, we can then set constraints on the final mass and spin of the newly-formed BH (Batta & Ramirez-Ruiz 2019). Our understanding of the fate of the collapsing star thus depends on our ability to determine the critical specific angular momentum below which material is able to accrete without generating feedback.

General relativity plays a crucial role and sets the specific angular momentum

at the innermost stable circular orbit. The flow pattern changes dramatically if the specific angular momentum of the inflowing material is near this critical value, as gas will not only be compressed but will be able to dissipate its motion perpendicular to the plane of symmetry and form a disk that is only marginally supported by rotation (Beloborodov & Illarionov 2001; Lee & Ramirez-Ruiz 2006; Zalamea & Beloborodov 2009). As the specific angular momentum increases, the rotational support becomes progressively more dominant until a standard Keplerian disk is formed. In this Letter we perform the first multidimensional general relativistic simulations of uniformly rotating, low angular momentum non-magnetized flows (Section 7.3), in order to derive the properties of the flow near this critical transition (Section 7.4) and establish when feedback becomes relevant (Section 7.5). We then make use of these results to obtain an upper limit on the angular momentum that would allow the observed massive stellar progenitors to vanish without a trace (Section 7.6).

7.3 Numerical setup and Initial Conditions

We performed two-dimensional numerical simulations of low angular momentum, flows using the Eulerian code HARM (Gammie et al. 2003b; Noble et al. 2006b), which solves the equations of general relativistic MHD (GRMHD). Our setup consists of a quasi-radial inflow of non-magnetized gas onto an accreting BH. The infalling gas has specific angular momentum near the critical value, defined as that assigned to the innermost stable circular orbit (ISCO) of a BH. The numerical setup is similar to the one described in Suková & Janiuk (2015), Suková et al. (2017), Janiuk et al. (2018) and

Palit et al. (2019).

The boundary conditions in the angular direction are set to be periodic while the outer inner boundary is set to be out-flowing and the outer radial boundary is set to the inflow condition. This boundary is placed at large enough radii such that it will not impact the central region over the duration of the simulation ($\approx 300 r_{\rm g}/c$) (Suková et al. 2017).

The units of the code are in the geometric system in which lengths are expressed in terms of the gravitational radius

$$r_{\rm g} = \frac{G M_{\rm bh}}{c^2}, \tag{7.1}$$

where $M_{\rm bh}$ is the mass of the BH. For converting to cgs units, we used the same convention as that described in Janiuk (2019). In this convention, if $M_{\rm bh} = 1 M_{\odot}$, the time unit is 5×10^{-6}s and $r_{\rm g} = 1.48$km. In our particular case, we choose $M_{\rm bh} = 20 M_{\odot}$, which corresponds to a time unit of 9.9×10^{-5}s, and a length unit of 29.5km. For our simulations, the enclosed mass in the computational domain, defined as $2\pi \int_0^{\pi} \int_{R_{\rm in}}^{R_{\rm domain}} \rho \sqrt{-g} dr d\theta$, is chosen to be $0.2 M_{\odot}$ (where g is the determinant of the metric, $R_{\rm in}$ is the inner radius, and $R_{\rm domain}$ is the domain size), which in turn corresponds to a mass accretion rate of $0.1 M_{\odot}$/s.

The domain covers $R_{\rm domain} = 200 r_{\rm g}$ around the BH for simulations with a non-spinning BH, and $R_{\rm domain} = 100 r_{\rm g}$ for simulations with spin. The resolution is 800×800 cells in the x_1 and x_2 directions, where x_1 and x_2 are the coordinates in spherical Kerr-Schild form for a non-spinning BH, and 400×400 for a BH with spin. The initial

radial component of the velocity (u^r) of the material is determined by the relativistic version of the Bernoulli equation (Shapiro & Teukolsky 1986). In this formalism, the critical point ($r_{\rm s}$, where subscript s stands for the sonic point), where the flow becomes supersonic, is set as a free parameter. In this case, the critical point lies outside the domain at $r_{\rm s} = 1000 r_{\rm g}$, resembling a collapsing $34 M_\odot$ star from models of Woosley & Heger (2006). This implies that matter is always supersonic within our computational domain. The fluid is considered a polytrope with a pressure $P = K\rho^\gamma$, where ρ is the density, $\gamma = 4/3$ is the adiabatic index, and K is the specific entropy, in this case taken to be that of a relativistic fluid with inefficient cooling. In what follows we describe how we generate the initial conditions.

Once the critical point is determined, the velocity at this critical point is (Shapiro & Teukolsky 1986):

$$[u^r_{\rm s}]^2 = \frac{G M_{\rm bh}}{2 r_{\rm s}}, \tag{7.2}$$

where r is the radial coordinate and u^r is the radial component of the four-velocity. The radial velocity can be obtained by numerically solving the relativistic Bernoulli equation:

$$\left(1 + \frac{\gamma}{\gamma - 1}\frac{P}{\rho}\right)^2 \left(1 - \frac{2GM_{\rm bh}}{r} + [u^r]^2\right) = \text{constant}, \tag{7.3}$$

and the density is set by the mass accretion rate $\dot{M}$:

$$\rho = \frac{\dot{M}}{4\pi r^2 u^r}. \tag{7.4}$$

The specific entropy value, K, depends on the radial velocity and is taken to

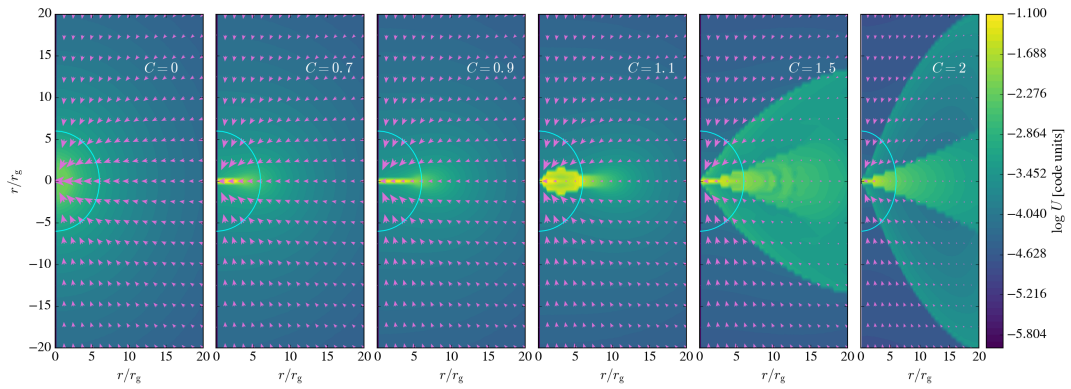

Figure 7.1: Contour plot of internal energy density (in code units) at $t = 300 r_{\rm g}/c$ for simulations of initially non-spinning BHs ($a_0 = 0$) with varying C. The arrows represent the velocity vectors of the flow, and the cyan circle shows the location of the ISCO.

be (Suková & Janiuk 2015; Suková et al. 2017; Palit et al. 2019):

$$K = \left(u^r 4\pi r^2 \frac{c_{\rm s}^{\frac{2}{\gamma-1}}}{\gamma^{\frac{1}{\gamma-1}} \dot{M}} \right)^{\gamma-1}, \tag{7.5}$$

where $c_{\rm s}^2 = \frac{\gamma P}{\rho}$ is the local sound speed.

In order to derive the angular velocity at each radius, we use the specific energy and angular momentum at the ISCO (Suková & Janiuk 2015; Suková et al. 2017; Palit et al. 2019):

$$\epsilon_{\rm isco} = -u_{t,{\rm isco}} = \frac{1 - 2/r_{\rm isco} + a/r_{\rm isco}^{3/2}}{\sqrt{1 - 3/r_{\rm isco} + 2a/r_{\rm isco}^{3/2}}} \tag{7.6}$$

and

$$l_{\rm isco} = u_{\phi,{\rm isco}} = \frac{r_{\rm isco}^{1/2} - 2a/r_{\rm isco} + a^2/r_{\rm isco}^{3/2}}{\sqrt{1 - 3/r_{\rm isco} + 2a/r_{\rm isco}^{3/2}}}, \tag{7.7}$$

where the radius of the ISCO $r_{\rm isco}$ in units of $r_{\rm g}$ if a function of the dimensionless BH spin a. The angular velocity in Boyer-Lindquist coordinates for a Kerr metric can then

be constructed as

$$u^{\phi} = g^{\phi\nu} u_{\nu}, \tag{7.8}$$

where ν is an index used for Einstein summation notation, ν belongs to $\{t, r, \theta, \phi\}$. For geodesic circular motion at the ISCO, the angular velocity is thus

$$u^{\phi}_{\rm isco} = -g^{\phi t}\epsilon_{\rm isco} + g^{\phi\phi} l_{\rm isco}, \tag{7.9}$$

where the components of the Kerr BH metric are $g^{t\phi} = -2ar/(\Sigma\Delta)$ and $g^{\phi\phi} = (\Delta - a^2 \sin^2\theta)/(\Sigma\Delta \sin^2\theta)$, with $\Sigma = r^2 + a^2\cos^2\theta$, $\Delta = r^2 - 2r + a^2$, and θ is the angular coordinate.

In our simulations, we include a factor $C\sin^2\theta$ in the initial angular velocity profile such that

$$u^{\phi} = C\sin^2\theta(-g^{t\phi}\epsilon_{\rm isco} + g^{\phi\phi} l_{\rm isco}). \tag{7.10}$$

The factor $\sin^2\theta$ ensures that the angular momentum vanishes smoothly in the polar regions (Suková et al. 2017), and C is a parameter that we vary. Note that $C = 0$ corresponds to Bondi spherical accretion.

The initial angular momentum per unit mass is then given by $l = u_{\phi} = g_{\phi\nu}u^{\nu}$. In the case of $a = 0$, it reduces to

$$l = C l_{\rm isco}\sin^2\theta. \tag{7.11}$$

In what follows we study the outcome of our simulations as we systematically

vary C from the classical $C = 0$ (spherical Bondi) to $C = 2$. This allows us to study the formation of accretion disks in low angular momentum flows along with exploring the dissipation of energy in the flow and ensuing feedback.

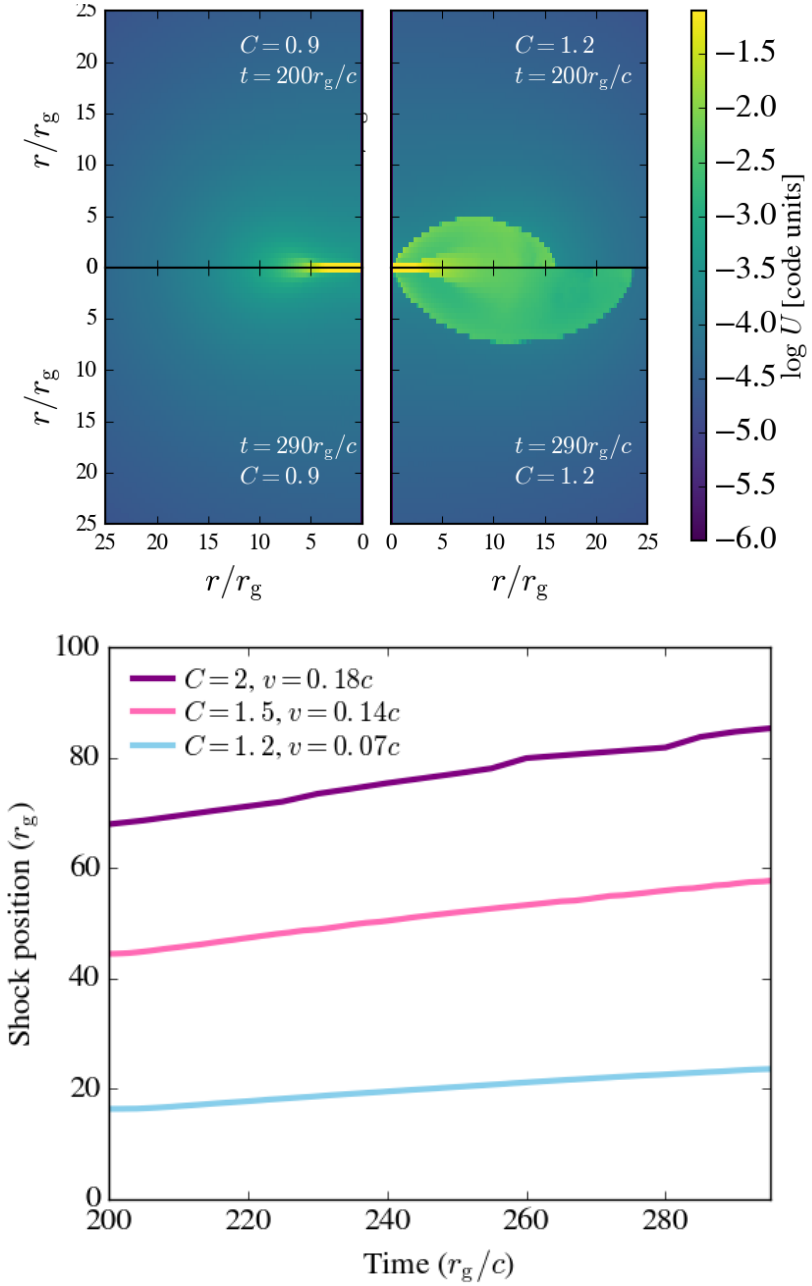

Figure 7.2: *Top* panel: The evolution of the internal energy density for two different simulations with $C = 0.9$ and $C = 1.2$ plotted at two different times for BHs with initial spin $a_0 = 0$. The resolution is the same as in Figure 7.1. *Bottom* panel: The location of the shock discontinuity in the equatorial plane as a function of time. Plotted here are the shock locations for $C = 2$ (purple line), $C = 1.5$ (pink line), and $C = 1.2$ (blue line). Shown in the legend are the average shock front expansion velocities measured at the equator for the different values of C.

7.4 Low angular momentum flows

As the star collapses, material will flow towards the newly formed BH and its angular momentum content will determine the final fate of the accreting object. If there is even a small amount of angular momentum, there will be dissipation of energy at the equator as material is shocked rather than solely compressed (Beloborodov & Illarionov 2001; Lee & Ramirez-Ruiz 2006; Zalamea & Beloborodov 2009).

If the specific angular momentum is below critical, the energy dissipation will be small and the heated gas will be promptly advected onto the BH. This is shown in Figure 7.1, where we plot contours of internal energy density and velocity vectors from simulations with varying C. The internal energy density in our simulations is related to the pressure as $U = \frac{P}{\gamma-1}$. As the specific angular momentum increases, material will be marginally bound and shocked near the equator before being accreted. When the angular momentum is near the critical one, a shock discontinuity forms that steadily dissipates energy, which leads to a significant pressure build up. This is most evidently seen in the simulations at around $C = 1.1$. This pressure build up slows down the incoming material and produces an angular momentum redistribution shock. It is noteworthy to point out that this shock is only transonic for the case of $C = 2$. It is useful to compare the energy density in cases with higher angular momentum to the case $C = 0$, where we expect inefficient feedback.

As more material accumulates near the ISCO, the pressure supported structure grows and expands for $C \gtrsim 1.2$, ultimately halting the flow. The *top* panel of Figure 7.2 compares the time evolution of the energy dissipation for simulations with $C = 0.9$

and $C = 1.2$. In the case of $C = 0.9$, where the specific angular momentum is below the critical one, the dissipated energy is advected with the flow before being accreted by the BH. When $C = 1.2$, a rotationally supported structure forms, which creates an expanding high-pressure region or hot bubble. The energy accumulation in this region continues until the end of the simulations, leading to the steady increase of the bubble's size. This steady accumulation of energy could, in principle, halt the collapse of the infalling star and cause the envelope to be disrupted. The *bottom* panel of Figure 7.2 shows the position of the shock in the equatorial plane as a function of time, as well as the velocity of the shock. The shock moves outward with a velocity that is roughly constant in time and is larger than the escape velocity at the outer edge of the computational domain (which is $0.07c$). The material inside the shock will gain internal specific energy similar to the shock's kinetic energy, which is larger than the specific binding energy at the edge of the computational domain. This means that the expanding shock will be able to halt the collapse and effectively unbind the material at the edge of the computational domain. However, this should be treated with caution, because it ignores the pressure from external material, which may act as a lid. In order to reach firm conclusions about the fate of the collapsing star, we need to track the long-term evolution of the shock as it evolves through the entire stellar interior.

We note that in our simulations, we don't include the effects of a changing metric, which are explored by Janiuk et al. (2018). Not surprisingly, the authors found that the BH accretes matter more rapidly for a changing metric, which can potentially alter the critical value of C. However, this effect is only relevant in our simulations at

times that are much larger than those currently explored. This is becaus throughout our simulation, the BH only accretes a fraction $\lesssim 0.01$ of its own mass, and thus the effects of both the self-gravity of the gas residing in the box and the corresponding change in the metric can be safely ignored. The critical angular momentum can also be altered by the inclusion of magnetic fields in the pre-collapse progenitor as well as the inclusion of radiation feedback. In the former case there can be additional outflows driven by the magnetic field stresses that can inject extra energy into the infalling material (McKinney et al. 2012; Janiuk 2019; Batta & Ramirez-Ruiz 2019). In the latter case, we expect that photons will be entirely advected onto the BH by the very optically thick accretion flow that is many orders of magnitude above the Eddington mass accretion limit in our simulation. The material is also expected to be optically thick to neutrinos, but if hypercritical accretion produces a neutrino-driven outflow, it could further help unbind the star (Kohri et al. 2005).

7.5 Energy Dissipation and Feedback

As shown in Section 7.4, the dissipation of energy in the infalling gas from a collapsing star with $C \gtrsim 1.2$ can steadily accumulate near the equatorial plane. In this case, the energy dissipation rate exceeds the advection rate as the size of the dissipation region increases and, as a result, a hot pressure region or bubble is produced. This bubble, surrounded by a clear discontinuity in both density and velocity, grows as material continues to be accreted. The corresponding pressure build up halts the motion of the infalling material in the equatorial plane while increasing the rate of

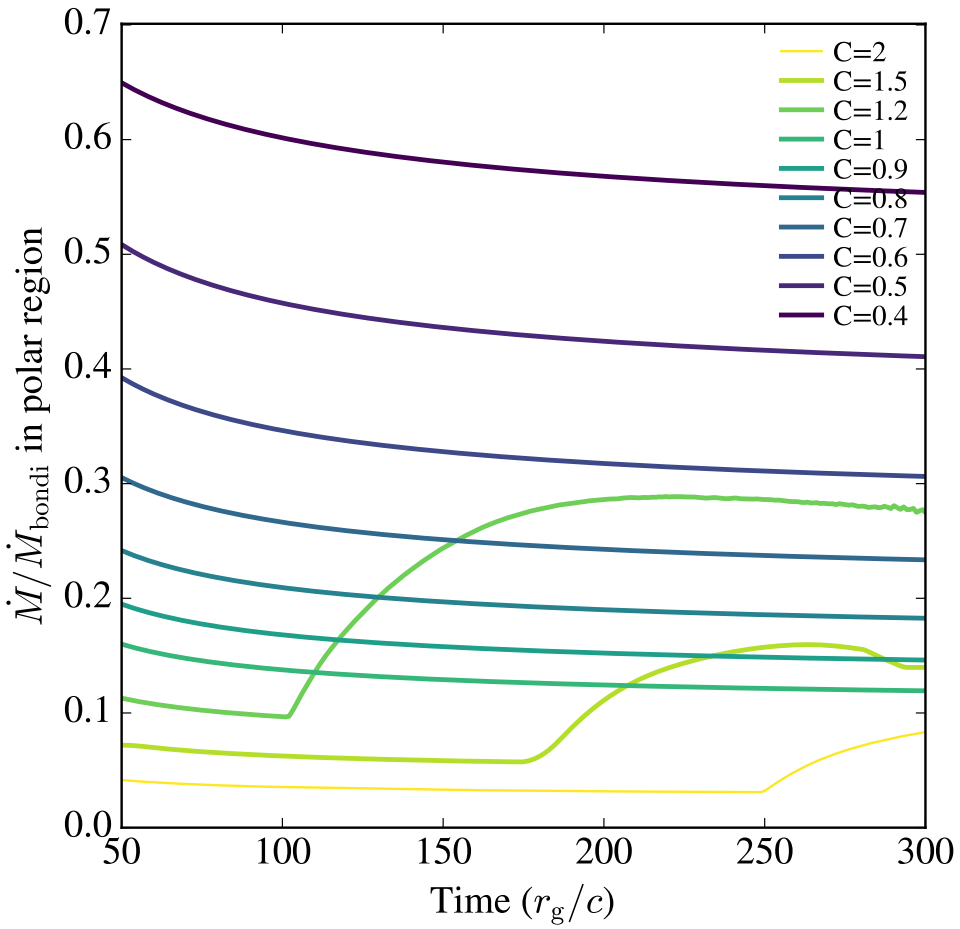

Figure 7.3: Mass accretion rates (in units of $\dot{M}_{\rm bondi}$) in the polar region for simulations with varying C and initially non-spinning BHs. The values for both $\dot{M}$ and $\dot{M_{\rm bondi}}$ are averaged at the ISCO over one quadrant of the simulation. The polar region is defined here by $0^\circ \leq \theta < 60^\circ$, with $\theta = 90$ corresponding to the equatorial plane.

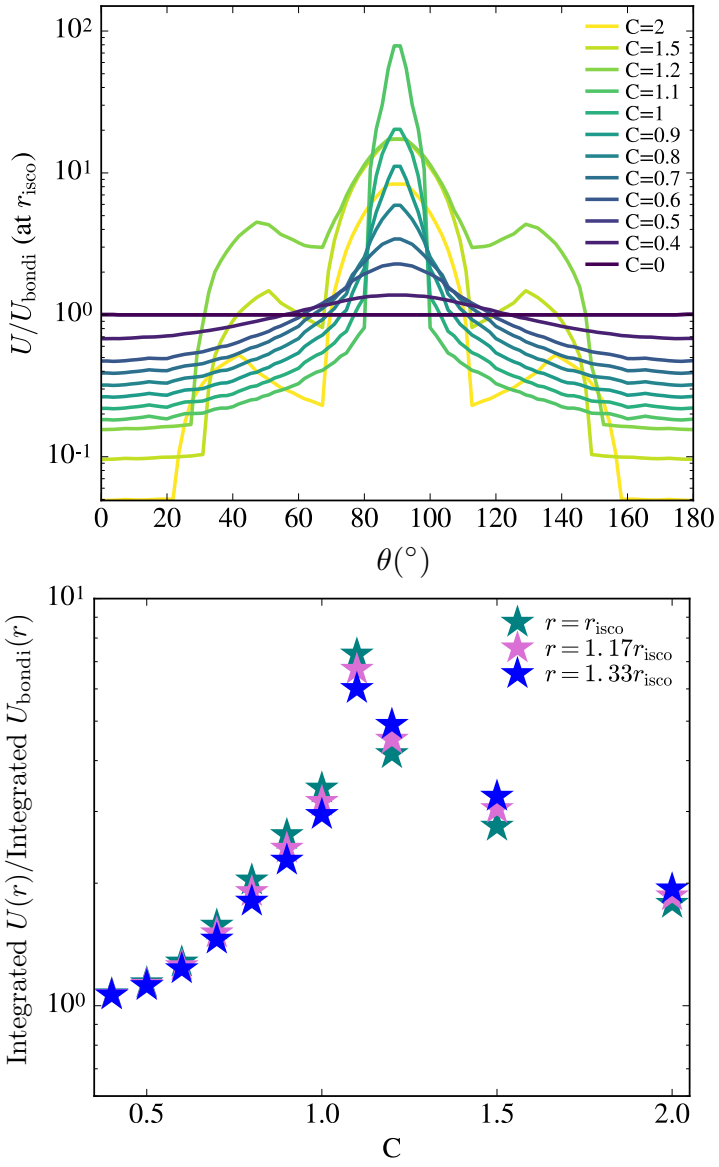

Figure 7.4: The dissipation of energy in low angular momentum flows. Top panel: Internal energy density at the ISCO as a function of θ for initially non-spinning BHs. Here $\theta = 90^\circ$ corresponds to the equator. The normalization factor ($U_{\rm bondi}$) corresponds to $C = 0$ case, which is spherically symmetric accretion and is solely driven by the compression of the flow. Bottom panel: Integrated internal energy out to a given radial scale as a function of C. The integrated internal energy is calculated as $U(r) = 2\pi \int_0^\pi \int_{2r_{\rm g}}^r \sqrt{-g(r')} U(r') dr' d\theta$, where g is the determinant of the metric and we use $r = [1, 1.17, 1.33] r_{\rm isco}$. All the analyses make use of the snapshot at $t = 300 r_{\rm g}/c$ for all simulations.

accretion in the polar direction, as material at high latitudes is deflected towards the BH (Figure 7.1). This can be seen in Figure 7.3, which shows the accretion rate in the polar direction as a function of time for all simulations with initial $a = 0$ and varying C.

The amount of energy dissipated by accretion is commonly thought to be primarily determined by $\dot{M}$. Yet, since BHs do not have a hard surface, the feedback efficiency cannot be given solely by $\dot{M}$ as in the case of neutron stars or white dwarfs. Nor can BHs build up enough pressure to slow down the infalling gas. Therefore, spherical accretion onto BHs advects any dissipated energy, without appreciable feedback. This situation changes dramatically when the inflow has a non-negligible amount of angular momentum and material is able to form a rotationally supported structure. In these cases, the energy dissipation rate is drastically altered. This can be seen in Figure 7.4, where we plot in the top panel the internal energy density profile (normalized to Bondi) around the ISCO as a function of θ. In this figure, $\theta = 90^\circ$ corresponds to the equator and $\theta = 0^\circ$ (180°) to the polar direction.

Even though there is internal energy and mass accumulation when $C \lesssim 1.2$, feedback will be inefficient because the flow is supersonic and the internal energy will be advected. The dissipation rate increases dramatically with C as can be seen in the bottom panel of Figure 7.4. Plotted in this panel is the integrated energy density out to a given radial coordinate normalized to the classical Bondi case ($C = 0$). The total dissipated energy increases as material with low angular momentum is shocked in the equatorial plane before being advected onto the BH. A noticeable transition

occurs at $C \approx 1.2$, as material begins to form a rotationally supported structure. The now differentially rotating flow requires MHD stress in order to dissipate energy and transport angular momentum, thereby enabling the inward accretion of gas. At this stage, the energy dissipation rate decreases as material becomes rotationally supported and shock dissipation is replaced by shear viscosity. In the absence of magnetic fields, shear viscosity in our simulation is driven by numerical dissipation, which also acts over many orbital timescales. We thus caution the reader that the exact value of C from our hydrodynamical simulations might be altered when internal MHD stresses are self-consistently included, as a magnetized outflow can form that can further help halt the stellar collapse (McKinney et al. 2012; Janiuk 2019; Batta & Ramirez-Ruiz 2019). In our current simulations, it is around $C \approx 1.2$ that we see the formation of the hot bubble, which continues to grow as the dissipated energy effectively accumulates near the ISCO (Figure 7.2). As the angular momentum continues to increase, a disk forms, which halts the advection of material and acts as a feedback term to slow the growth of energy dissipation near the ISCO. We thus conclude that for flows with $C \gtrsim 1.2$, we expect feedback to likely halt the collapse of the infalling star. Because the binding energy of failed SN progenitors steeply declines with increasing radius, it is suggested that any additional accumulation of energy will ultimately result in the disruption of the entire collapsing progenitor (Quataert et al. 2019; Batta & Ramirez-Ruiz 2019). As the expanding envelope cools and radiation diffuses from it (e.g., Schrøder et al. 2020), a transient is expected to accompany the formation of the BH (Fryer 1999; Woosley & Heger 2006; Lovegrove & Woosley 2013; Smartt 2015; Kochanek 2015; Sukhbold et al.

2016; Quataert et al. 2019).

In addition to the initially non-spinning $a_0 = 0$ BH models, we also ran simulations with $a_0 = 0.05$ and $a_0 = 0.1$ and confirm that the feedback transition also occurs near $C \approx 1.2$ and that the energy dissipation profiles are similar to those plotted in Figure 7.4. This is consistent with Janiuk et al. (2018), where the authors use a dynamical metric to explore how the accretion onto a BH influences the spin and final mass of the BH. They conclude that different initial spins lead to rather similar qualitative results, as we have found here.

7.6 Discussion

Having determined the critical specific angular momentum at which accretion onto a BH can generate feedback, we turn our attention to the conditions required for a stellar progenitor to collapse without producing a bright transient under the assumption that significant feedback will unavoidably generate a discernible signal. In what follows, for simplicity, we assume that the star is uniformly rotating.

The corresponding critical angular velocity of the stellar progenitor is quantitatively estimated using the framework established by Batta & Ramirez-Ruiz (2019), in which the formation and evolution of a BH is followed throughout the stellar collapse. For feedback not to be effective, the stellar progenitor needs to satisfy the following condition at all radii:

$$l(r) \leq l_{\rm fb}(r) = C_{\rm fb} l_{\rm isco}(r). \tag{7.12}$$

Here $C_{\rm fb}$ is the critical normalization factor taken to be $C_{\rm fb} = 1.2$ and $l_{\rm isco}(r)$ is the spe-

cific angular momentum at the ISCO (Bardeen et al. 1972), which evolves as collapsing material is accreted by the BH.

While rotating at such limiting angular velocity, only the star's outermost material has enough specific angular momentum $\Omega_{\rm lim} R_*^2$ to balance the critical condition $C_{\rm fb}\ l_{\rm isco}(R_*)$. At the same time, the rest of the material satisfies condition 7.12. In the ensuing subsections we express $\Omega_{\rm lim}$ in terms of the star's breakup angular velocity, $\Omega_{\rm break} = \left(GM_*/R_*^3\right)^{1/2}$, where M_* and R_* are the stellar mass and radius, respectively.

7.6.1 On the disappearing stellar progenitors of N6946-BH1 and PHL293B-LBV

Let us now turn our attention to the properties of N6946-BH1 and PHL293B-LBV, two stars that have been argued to disappear without an accompanying bright transient (Gerke et al. 2015; Adams et al. 2017; Allan et al. 2020). While other explanations might be viable, a collapse to a BH without feedback is a possible explanation for the sudden disappearance of the star.

We use the stellar evolution code MESA (Paxton et al. 2011, 2013) version 8845 in order to constrain the structure and observational properties of these stars. We use the default MESA parameters for massive stars. For simplicity, our models are non-rotating, and their evolution is halted when carbon burning ends. We ran the models using a Dutch hot wind scheme (Glebbeek et al. 2009) with a scaling factor of 0.8. In this wind scheme, the mass loss rate prescription changes depending on the evolutionary stage of the star. For the rest of the paper, we take $Z_\odot = 0.02$.

N6946-BH1 is a disappearing star found by Gerke et al. (2015) and Adams

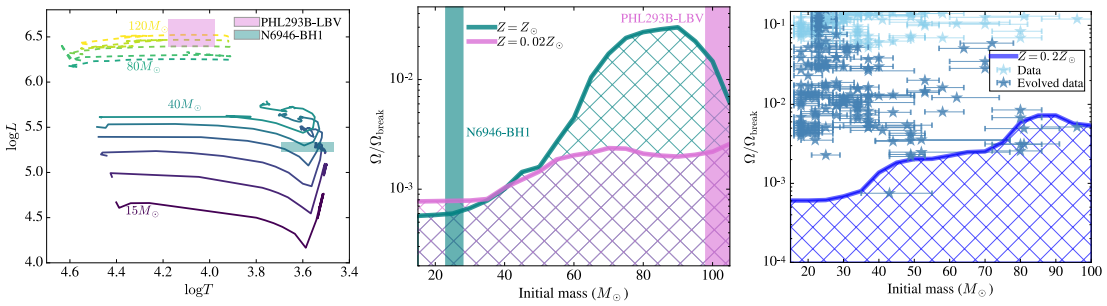

Figure 7.5: Left Panel: Hertzsprung-Russell diagram of the MESA models used in our analysis (Paxton et al. 2011, 2013). The solid lines are models with $Z = Z_\odot$. The solid lines are stellar models that start at $M_{\rm ZAMS} = 15M_\odot$ and are plotted every $5M_\odot$ until $40M_\odot$. In teal we show the luminosity and temperature constraints for N6946-BH1 (Gerke et al. 2015; Adams et al. 2017). The dotted lines represent models with $Z = 0.02Z_\odot$. Models start at $M_{\rm ZAMS} = 80M_\odot$ and are plotted every $10M_\odot$ until $120M_\odot$. Models with $Z = 0.02Z_\odot$ were used to constrain PHL293B-LBV (Allan et al. 2020), whose luminosity and temperature constraints are shown in orchid. Middle Panel: Maximum angular velocity at which a star can disappear without an accompanying bright transient as a function of the initial mass of the progenitor. Here $\Omega_{\rm break}$ is the breakup velocity. The different lines are the constraints derived at different metallicities, which have been selected to match those of N6946-BH1 and PHL293B-LBV. Also plotted are the mass estimates we derive from our MESA models. Models in this specific mass range spend a fraction of their last 10^4 years of evolution within the corresponding uncertainty region in the HR diagram (Left Panel). Right Panel: Angular velocity as a function of the initial mass of the stellar progenitor. Plotted are the rotational velocities of single O-type stars at $Z = 0.2Z_\odot$ taken from Ramírez-Agudelo et al. (2013), with masses derived by Weidner & Vink (2010). We evolve the rotational velocities of MESA models of these O-type stars by applying Equation 7.13 and assuming rigid body rotation until carbon burning ends (see text for details about this assumption). These pre-collapse rotational velocities, labelled as *evolved data*, are compared with the range of angular velocities for these stars to collapse without an accompanying bright transient (hatched region).

et al. (2017) using the *Large Binocular Telescope*. The star is found to be embedded in a highly dusty environment in the galaxy NGC 6946. This red supergiant star was observed to increase its optical magnitude by around 5 magnitudes after a weak optical outburst in 2009. One possibility for this disappearing star is a collapse to a BH where the angular momentum was low enough that feedback from the BH was unable to unbind

the collapsing progenitor.

Information on the progenitor was deduced using archival data from the *Hubble Space Telescope*, which was taken around two years before the weak outburst. Using dust and stellar evolution models, Gerke et al. (2015) and Adams et al. (2017) deduced a luminosity of $\log L/L_{\odot} = 5.29^{+0.04}_{-0.06}$ and a temperature of $T = 3260^{+1670}_{-320}K$ for the pre-collapse progenitor. Their solar metallicity models constrained the progenitor mass to be $20 - 30M_{\odot}$.

PHL293B-LBV (Allan et al. 2020) is another disappearing star. This luminous blue variable (LBV) was found in the galaxy PHL293B. Allan et al. (2020) used ESO/VLT's ESPRESSO and X-shooter to obtain spectra of this galaxy in 2019. These spectra lacked an LBV signature, which was clearly present from 2011 to 2019. One of many viable possibilities is that when the eruptive period ended, the LBV collapsed into a BH. Using radiative transfer models, Allan et al. (2020) derived a luminosity between $\log L/L_{\odot} = 6.3 - 6.7$ and a temperature between $T = 9,500 - 15,000K$ for the pre-collapse star.

We compare the temperature and luminosity constraints of N6946-BH1 and PHL293B-LBV with our stellar models in order to constrain both their masses and internal structures. The left panel of figure 7.5 shows the locations of N6946-BH1 and PHL293B-LBV on the Hertzsprung-Russell diagram together with the MESA stellar evolutionary models. The solid lines correspond to models with $Z = Z_{\odot}$, which are relevant to N6946-BH1 (Gerke et al. 2015; Adams et al. 2017), while the dotted lines correspond to models with $Z = 0.02Z_{\odot}$, appropriate for PHL293B-LBV (Allan et al.

2020). Using these models we constrain the initial masses of N6946-BH1 and PHL293B-LBV to be $23 - 28 M_{\odot}$ and $98 - 130 M_{\odot}$, respectively. These constraints are consistent with those quoted in the literature. We caution the reader that given the mass range deduced for PHL293B-LBV, the final outcome could be a pair instability supernova (Woosley 2017). Nonetheless, the lack of a transient event for PHL293B-LBV suggests that this was not the case, as argued by Allan et al. (2020).

We use these models to also constrain the internal density structure of the progenitor, which in turn sets the moment of inertia and allows us to place a limit on the maximum angular velocity needed for the star to collapse without forming a disk. These limits for N6946-BH1 and PHL293B-LBV are plotted in the middle panel of Figure 7.5. Within the hatched region, the angular velocity of the pre-collapse progenitor is below the critical one in which feedback becomes efficient. The regions extends to higher fractions of the break-up velocity for high-mass solar-metallicity stars because these stars self-strip due to rapid wind-driven mass loss, leaving behind compact, low moment of inertia Wolf-Rayet stars. We thus suggest that progenitors within this region will collapse without producing a bright transient.

7.6.2 Is it common for stars to vanish without a trace?

In the preceding sections we have endeavoured to outline the rotational constraints needed for stellar progenitors to vanish without a trace. We caution that even in the absence of rotation, the outer layers might be still ejected by, for example, the loss of rest mass energy via neutrinos (e.g., Lovegrove & Woosley 2013) and could still produce a faint transient signal (e.g. MacLeod et al. 2017b).

Herein we assume that stellar spin is an essential parameter and turn to the problem of assembling the pre-collapse rotational constraints derived in this Letter into a general scheme involving the evolution of massive stars. In the right panel of figure 7.5 we plot the observationally derived rotation rates of single O-type ($Z = 0.2Z_{\odot}$) stars taken from Ramírez-Agudelo et al. (2013) with initial stellar masses derived by Weidner & Vink (2010).

We produce MESA models to match the age and stellar mass of these stars, using $Z = 0.2Z_{\odot}$ and assuming rigid body rotation. Applying the observationally derived rotation rates, we then make use of the following standard relation (Villata 1992):

$$\frac{1}{\Omega}\frac{d\Omega}{dt} = -\frac{1}{I_*}\frac{dI_*}{dt} + \frac{2}{3}\frac{R_*^2}{I_*}\frac{dM_*}{dt}. \tag{7.13}$$

Where where M_* and R_* are the stellar mass and radius, respectively, $I_* = \frac{8\pi}{3}\int_0^{R_*}\rho(r)r^4dr$ is the moment of intertia of the star, and Ω is the angular velocity. The evolution of the rotational velocity is then computed until the end of the star's life, which in our models corresponds to the end of carbon burning. In the right panel of Figure 7.5 we plot the final rotational velocity derived for each observed system with the corresponding symbols labelled as *Evolved data*.

Throughout this paper, we assumed rigid-body rotation, i.e., very efficient angular momentum transport within the star. It is evident that the mechanisms responsible for transporting angular momentum inside massive stars are currently not well understood (Kissin & Thompson 2015; Fuller & Ma 2019). Even in the simplest case of uniform rotation, we find that stellar winds can extract a significant amount of

angular momentum from the star and in a small fraction of cases produce rotation rates close to those required for stars to vanish without a trace (right panel of Figure 7.5). More specifically, we find that ≈5% of the stars we evolved (from a total of 163) have $(\Omega/\Omega_{\rm break})$ below the critical value (hatched region in the right panel of Figure 7.5). In these cases we expect the collapse to proceed without the formation of an accretion disk, allowing the progenitor to vanish in our model.

Although the evolution of O-type stars may be be commonly associated with supernovae, some of them might be expected to disappear. If single O-type stars with $(\Omega/\Omega_{\rm break})$ below the critical value are expected to vanish, we then conclude that these objects are at least tens of times rarer than standard supernova events. This of course has been derived under the assumption that a standard supernova event is the natural outcome for the vast majority of O-type stars with $(\Omega/\Omega_{\rm break})$ above the critical value. Obviously, the above calculation is limited and should be taken as an order of magnitude estimate at present. For example, using the same Dutch hot wind scheme in MESA but with a scaling factor of 1.0 (instead of the standard 0.8) we find that ≈7% of the stars we evolved have $(\Omega/\Omega_{\rm break})$ below the critical (mass-dependent) value.

This simple estimate for the rate of disappearing massive stars should improve as more objects have their rotational rates measured and massive stellar evolution modelling improves. Having said this, it is important to note that this few percent estimate is roughly consistent with the one derived by Gerke et al. (2015), where they argued that the current rate of vanishing stars is $\gtrsim 7\%$ the rate of core collapse supernova. This estimate can also be altered for red supergiants, as convective motions in their outer

layers might produce accretion disks and thus effective feedback even in the absence of net rotation (Quataert et al. 2019).

Most massive stars are born in binaries, and binary interactions can significantly impact stellar structure and stellar rotation through mass transfer and tides (Sana et al. 2012). Accounting for the impact of binary evolution would further change the expected fraction of vanishing stars.

Many core collapses of massive stars are expected to produce supernovae when forming neutron stars in spherical explosions (Ugliano et al. 2012; Sukhbold et al. 2016) but some are expected to have insufficient neutrino deposition (Woosley 1993; Fryer et al. 2009; Lazzati et al. 2012; Lovegrove & Woosley 2013) and will form a BH in the center of the star.

The modeling of stellar collapse leading to BH formation is a formidable challenge to computational techniques. It is, also, a formidable challenge for observers, in their quest for finding stars that disappear. If we were to venture on a general classification scheme for failed supernovae, on the hypothesis that the central object involves a BH formed in a core collapse explosion, we expect the specific angular momentum of the infalling stellar material to be a critical parameter. When $l(r) \lesssim l_{\rm fb}(r)$ we predict the star will vanish without a trace. On the other hand, when $l(r) \gtrsim l_{\rm fb}(r)$ the collapse may instead be followed by a bright transient, whose properties will likely depend on the mass and spin of the BH, the rate at which gas is supplied, the spin orientation relative to our line of sight, and the structure of the envelope through which any outflows will be re-processed.

Chapter 8

Conclusion

This thesis has focused on all aspects of binary neutron stars as they merge. We use numerical simulations to understand what happens before and after the merger. With simulations, we can constrain elusive observational parameters of the binary system. By developing better simulations, we are better able to model and understand the mergers.

With the observation of GW170817 in gravitational waves and in electromagnetic light all over the spectrum, as described in Chapter 4, we now have evidence that binary neutron star merger result in a $\gamma-$ray burst. We also have evidence that binary neutron star mergers are responsible for creating at least a fraction of the heavy $r-$process elements in the Universe. Therefore, we need to continue studying binary neutron star mergers and what further lessons they have to teach us.

LIGO's fourth observing run is coming online next year, and with new telescopes such as the Vera Rubin observatory, this promises more exciting observations of

binary neutron stars and their electromagnetic counterparts in the future. The need for theoretical models that couple with observations is clear. With better codes and better modeling, we will be poised to tackle the challenges to come, leading us towards an even deeper understanding of the relevant physics governing the most extreme conditions in the Universe.

Bibliography

Abbott, B. P., Abbott, R., Abbott, T. D., et al. 2016a, Phys. Rev. Lett., 116, 241102, doi: 10.1103/PhysRevLett.116.241102

—. 2016b, Physical Review X, 6, 041015, doi: 10.1103/PhysRevX.6.041015

—. 2017a, Phys. Rev. Lett., 118, 221101, doi: 10.1103/PhysRevLett.118.221101

—. 2017b, ApJ, 851, L35, doi: 10.3847/2041-8213/aa9f0c

—. 2016c, ApJ, 832, L21, doi: 10.3847/2041-8205/832/2/L21

—. 2016d, Physical Review Letters, 116, 061102, doi: 10.1103/PhysRevLett.116.061102

—. 2017c, Physical Review Letters, 119, 161101, doi: 10.1103/PhysRevLett.119.161101

—. 2017d, ApJ, 848, L12, doi: 10.3847/2041-8213/aa91c9

Adams, S. M., Kochanek, C. S., Gerke, J. R., Stanek, K. Z., & Dai, X. 2017, Monthly Notices of the Royal Astronomical Society, 468, 4968, doi: 10.1093/mnras/stx816

Alexander, K. D., Berger, E., Fong, W., et al. 2017, ApJ, 848, L21, doi: 10.3847/2041-8213/aa905d

Allan, A., Groh, J., Mehner, A., et al. 2020, The disappearance of a massive star in the

low metallicity galaxy PHL 293B. https://arxiv.org/abs/2003.02242

Aloy, M. A., Janka, H.-T., & Müller, E. 2005, A&A, 436, 273, doi: 10.1051/0004-6361:20041865

Aloy, M. A., & Rezzolla, L. 2006, ApJ, 640, L115, doi: 10.1086/503608

Antoniadis, J., Freire, P. C. C., Wex, N., et al. 2013, Science, 340, 448, doi: 10.1126/science.1233232

Armitage, P. J., & Livio, M. 2000, ApJ, 532, 540, doi: 10.1086/308548

Baiotti, L., Giacomazzo, B., & Rezzolla, L. 2008, Phys. Rev. D, 78, 084033, doi: 10.1103/PhysRevD.78.084033

Balbus, S. A., & Hawley, J. F. 1991, ApJ, 376, 214, doi: 10.1086/170270

—. 1998, Reviews of Modern Physics, 70, 1, doi: 10.1103/RevModPhys.70.1

Bardeen, J. M., Press, W. H., & Teukolsky, S. A. 1972, ApJ, 178, 347, doi: 10.1086/151796

Barnes, J., & Kasen, D. 2013, ApJ, 775, 18, doi: 10.1088/0004-637X/775/1/18

Barnes, J., Kasen, D., Wu, M.-R., & Martínez-Pinedo, G. 2016, ApJ, 829, 110, doi: 10.3847/0004-637X/829/2/110

Batta, A., & Ramirez-Ruiz, E. 2019, arXiv e-prints, arXiv:1904.04835. https://arxiv.org/abs/1904.04835

Baumgarte, T. W., Shapiro, S. L., & Shibata, M. 2000, ApJ, 528, L29, doi: 10.1086/312425

Begelman, M. C., & Cioffi, D. F. 1989, ApJ, 345, L21, doi: 10.1086/185542

Behroozi, P. S., Ramirez-Ruiz, E., & Fryer, C. L. 2014, ApJ, 792, 123, doi: 10.1088/

0004-637X/792/2/123

Belczynski, K., Dominik, M., Bulik, T., et al. 2010, ApJ, 715, L138, doi: 10.1088/2041-8205/715/2/L138

Belczynski, K., Holz, D. E., Bulik, T., & O'Shaughnessy, R. 2016, Nature, 534, 512, doi: 10.1038/nature18322

Belczynski, K., Kalogera, V., & Bulik, T. 2002, ApJ, 572, 407, doi: 10.1086/340304

Belczynski, K., Taam, R. E., Kalogera, V., Rasio, F. A., & Bulik, T. 2007, ApJ, 662, 504, doi: 10.1086/513562

Beloborodov, A. M., & Illarionov, A. F. 2001, MNRAS, 323, 167, doi: 10.1046/j.1365-8711.2001.04133.x

Beniamini, P., Granot, J., & Gill, R. 2020, MNRAS, 493, 3521, doi: 10.1093/mnras/staa538

Berger, E. 2014, ARA&A, 52, 43, doi: 10.1146/annurev-astro-081913-035926

Blandford, R. D., & Begelman, M. C. 1999, MNRAS, 303, L1, doi: 10.1046/j.1365-8711.1999.02358.x

Blondin, J. M. 2013, ApJ, 767, 135, doi: 10.1088/0004-637X/767/2/135

Blondin, J. M., & Pope, T. C. 2009, ApJ, 700, 95, doi: 10.1088/0004-637X/700/1/95

Blondin, J. M., & Raymer, E. 2012, ApJ, 752, 30, doi: 10.1088/0004-637X/752/1/30

Bloom, J. S., Kulkarni, S. R., Harrison, F., et al. 1998, ApJ, 506, L105, doi: 10.1086/311655

Bondi, H. 1952, MNRAS, 112, 195, doi: 10.1093/mnras/112.2.195

Bondi, H., & Hoyle, F. 1944, MNRAS, 104, 273, doi: 10.1093/mnras/104.5.273

Bonnor, W. B. 1958, MNRAS, 118, 523, doi: 10.1093/mnras/118.5.523

Bromberg, O., Nakar, E., Piran, T., & Sari, R. 2011, ApJ, 740, 100, doi: 10.1088/0004-637X/740/2/100

Bromberg, O., & Tchekhovskoy, A. 2016, MNRAS, 456, 1739, doi: 10.1093/mnras/stv2591

Bromberg, O., Tchekhovskoy, A., Gottlieb, O., Nakar, E., & Piran, T. 2018, MNRAS, 475, 2971, doi: 10.1093/mnras/stx3316

Cerdá-Durán, P., Font, J. A., Antón, L., & Müller, E. 2008, A&A, 492, 937, doi: 10.1051/0004-6361:200810086

Champion, D. J., Lorimer, D. R., McLaughlin, M. A., et al. 2004, MNRAS, 350, L61, doi: 10.1111/j.1365-2966.2004.07862.x

Chen, W.-C., & Podsiadlowski, P. 2017, ApJ, 837, L19, doi: 10.3847/2041-8213/aa624a

Chen, W.-X., & Beloborodov, A. M. 2007, ApJ, 657, 383, doi: 10.1086/508923

Chen, Z., Frank, A., Blackman, E. G., Nordhaus, J., & Carroll-Nellenback, J. 2017, MNRAS, 468, 4465, doi: 10.1093/mnras/stx680

Chevalier, R. A. 1989, ApJ, 346, 847, doi: 10.1086/168066

Ciolfi, R. 2020, MNRAS, 495, L66, doi: 10.1093/mnrasl/slaa062

Ciolfi, R., Kastaun, W., Giacomazzo, B., et al. 2017, Phys. Rev. D, 95, 063016, doi: 10.1103/PhysRevD.95.063016

Ciolfi, R., Kastaun, W., Kalinani, J. V., & Giacomazzo, B. 2019, Phys. Rev. D, 100, 023005, doi: 10.1103/PhysRevD.100.023005

Cipolletta, F., Kalinani, J. V., Giacomazzo, B., & Ciolfi, R. 2020, Classical and Quantum Gravity, 37, 135010, doi: 10.1088/1361-6382/ab8be8

Coulter, D. A., Foley, R. J., Kilpatrick, C. D., et al. 2017a, Science, 358, 1556, doi: 10.1126/science.aap9811

—. 2017b, Science, 358, 1556, doi: 10.1126/science.aap9811

Cowperthwaite, P. S., Berger, E., Villar, V. A., et al. 2017, ApJ, 848, L17, doi: 10.3847/2041-8213/aa8fc7

da Silva Schneider, A., Roberts, L. F., & Ott, C. D. 2017, arXiv e-prints, arXiv:1707.01527. https://arxiv.org/abs/1707.01527

D'Avanzo, P., Salvaterra, R., Bernardini, M. G., et al. 2014, MNRAS, 442, 2342, doi: 10.1093/mnras/stu994

D'Avanzo, P., Campana, S., Salafia, O. S., et al. 2018, A&A, 613, L1, doi: 10.1051/0004-6361/201832664

De, S., & Siegel, D. 2020, arXiv e-prints, arXiv:2011.07176. https://arxiv.org/abs/2011.07176

De Colle, F., Granot, J., López-Cámara, D., & Ramirez-Ruiz, E. 2012a, ApJ, 746, 122, doi: 10.1088/0004-637X/746/2/122

De Colle, F., Lu, W., Kumar, P., Ramirez-Ruiz, E., & Smoot, G. 2018, MNRAS, 478, 4553, doi: 10.1093/mnras/sty1282

De Colle, F., Ramirez-Ruiz, E., Granot, J., & Lopez-Camara, D. 2012b, ApJ, 751, 57, doi: 10.1088/0004-637X/751/1/57

De Marco, O., & Izzard, R. G. 2017, PASA, 34, e001, doi: 10.1017/pasa.2016.52

Demorest, P. B., Pennucci, T., Ransom, S. M., Roberts, M. S. E., & Hessels, J. W. T. 2010, Nature, 467, 1081, doi: 10.1038/nature09466

Dessart, L., Ott, C. D., Burrows, A., Rosswog, S., & Livne, E. 2009, ApJ, 690, 1681, doi: 10.1088/0004-637X/690/2/1681

Dewi, J. D. M., & Tauris, T. M. 2000, A&A, 360, 1043

Di Matteo, T., Perna, R., & Narayan, R. 2002, ApJ, 579, 706, doi: 10.1086/342832

Dionysopoulou, K., Alic, D., & Rezzolla, L. 2015, Phys. Rev. D, 92, 084064, doi: 10.1103/PhysRevD.92.084064

Dominik, M., Belczynski, K., Fryer, C., et al. 2012, ApJ, 759, 52, doi: 10.1088/0004-637X/759/1/52

Drout, M. R., Piro, A. L., Shappee, B. J., et al. 2017, Science, 358, 1570, doi: 10.1126/science.aaq0049

Duez, M. D., Liu, Y. T., Shapiro, S. L., Shibata, M., & Stephens, B. C. 2006, Physical Review Letters, 96, 031101, doi: 10.1103/PhysRevLett.96.031101

Duffell, P. C., Quataert, E., Kasen, D., & Klion, H. 2018, ApJ, 866, 3, doi: 10.3847/1538-4357/aae084

Duffell, P. C., Quataert, E., & MacFadyen, A. I. 2015, ApJ, 813, 64, doi: 10.1088/0004-637X/813/1/64

Edgar, R. 2004, New A Rev., 48, 843, doi: 10.1016/j.newar.2004.06.001

Eichler, D., Livio, M., Piran, T., & Schramm, D. N. 1989, Nature, 340, 126, doi: 10.1038/340126a0

Etienne, Z. B., Paschalidis, V., Haas, R., Mösta, P., & Shapiro, S. L. 2015, Classical

and Quantum Gravity, 32, 175009, doi: 10.1088/0264-9381/32/17/175009

Faber, J. A., & Rasio, F. A. 2012, Living Reviews in Relativity, 15, 8, doi: 10.12942/lrr-2012-8

Fernández, R., Foucart, F., Kasen, D., et al. 2017, Classical and Quantum Gravity, 34, 154001, doi: 10.1088/1361-6382/aa7a77

Fernández, R., & Metzger, B. D. 2013a, MNRAS, 435, 502, doi: 10.1093/mnras/stt1312

—. 2013b, ApJ, 763, 108, doi: 10.1088/0004-637X/763/2/108

Fernández, R., Quataert, E., Schwab, J., Kasen, D., & Rosswog, S. 2015, MNRAS, 449, 390, doi: 10.1093/mnras/stv238

Fishbone, L. G., & Moncrief, V. 1976, ApJ, 207, 962, doi: 10.1086/154565

Fong, W., Berger, E., Margutti, R., & Zauderer, B. A. 2015, ApJ, 815, 102, doi: 10.1088/0004-637X/815/2/102

Fong, W., Metzger, B. D., Berger, E., & Özel, F. 2016a, ApJ, 831, 141, doi: 10.3847/0004-637X/831/2/141

Fong, W., Margutti, R., Chornock, R., et al. 2016b, ApJ, 833, 151, doi: 10.3847/1538-4357/833/2/151

Foucart, F., Duez, M. D., Kidder, L. E., et al. 2018, Phys. Rev. D, 98, 063007, doi: 10.1103/PhysRevD.98.063007

Foucart, F., O'Connor, E., Roberts, L., et al. 2016, Phys. Rev. D, 94, 123016, doi: 10.1103/PhysRevD.94.123016

—. 2015, Phys. Rev. D, 91, 124021, doi: 10.1103/PhysRevD.91.124021

Freiburghaus, C., Rosswog, S., & Thielemann, F.-K. 1999, ApJ, 525, L121, doi: 10.1086/312343

Fryer, C. L. 1999, ApJ, 522, 413, doi: 10.1086/307647

Fryer, C. L., Belczynski, K., Ramirez-Ruiz, E., et al. 2015, ApJ, 812, 24, doi: 10.1088/0004-637X/812/1/24

Fryer, C. L., Brown, P. J., Bufano, F., et al. 2009, ApJ, 707, 193, doi: 10.1088/0004-637X/707/1/193

Fryxell, B., Olson, K., Ricker, P., et al. 2000, ApJS, 131, 273, doi: 10.1086/317361

Fryxell, B. A., & Taam, R. E. 1988, ApJ, 335, 862, doi: 10.1086/166973

Fryxell, B. A., Taam, R. E., & McMillan, S. L. W. 1987, ApJ, 315, 536, doi: 10.1086/165157

Fujibayashi, S., Kiuchi, K., Nishimura, N., Sekiguchi, Y., & Shibata, M. 2018, ApJ, 860, 64, doi: 10.3847/1538-4357/aabafd

Fujibayashi, S., Sekiguchi, Y., Kiuchi, K., & Shibata, M. 2017, ApJ, 846, 114, doi: 10.3847/1538-4357/aa8039

Fuller, J., & Ma, L. 2019, ApJ, 881, L1, doi: 10.3847/2041-8213/ab339b

Galeazzi, F., Kastaun, W., Rezzolla, L., & Font, J. A. 2013, Phys. Rev. D, 88, 064009, doi: 10.1103/PhysRevD.88.064009

Gammie, C. F., McKinney, J. C., & Tóth, G. 2003a, ApJ, 589, 444, doi: 10.1086/374594

—. 2003b, ApJ, 589, 444, doi: 10.1086/374594

Gehrels, N., Ramirez-Ruiz, E., & Fox, D. B. 2009, ARA&A, 47, 567, doi: 10.1146/

annurev.astro.46.060407.145147

Geng, J.-J., Zhang, B., Kölligan, A., Kuiper, R., & Huang, Y.-F. 2019, ApJ, 877, L40, doi: 10.3847/2041-8213/ab224b

Gerke, J. R., Kochanek, C. S., & Stanek, K. Z. 2015, Monthly Notices of the Royal Astronomical Society, 450, 3289, doi: 10.1093/mnras/stv776

Ghirlanda, G., Salafia, O. S., Paragi, Z., et al. 2019, Science, 363, 968, doi: 10.1126/science.aau8815

Giacomazzo, B., Rezzolla, L., & Baiotti, L. 2011, Phys. Rev. D, 83, 044014, doi: 10.1103/PhysRevD.83.044014

Gilkis, A., & Soker, N. 2014, MNRAS, 439, 4011, doi: 10.1093/mnras/stu257

—. 2016, ApJ, 827, 40, doi: 10.3847/0004-637X/827/1/40

Gill, R., Granot, J., De Colle, F., & Urrutia, G. 2019a, ApJ, 883, 15, doi: 10.3847/1538-4357/ab3577

Gill, R., Nathanail, A., & Rezzolla, L. 2019b, ApJ, 876, 139, doi: 10.3847/1538-4357/ab16da

Glebbeek, E., Gaburov, E., de Mink, S. E., Pols, O. R., & Portegies Zwart, S. F. 2009, A&A, 497, 255, doi: 10.1051/0004-6361/200810425

Goldstein, A., Veres, P., Burns, E., et al. 2017, ApJ, 848, L14, doi: 10.3847/2041-8213/aa8f41

Gottlieb, O., Bromberg, O., Singh, C. B., & Nakar, E. 2020a, arXiv e-prints, arXiv:2007.11590. https://arxiv.org/abs/2007.11590

Gottlieb, O., Nakar, E., & Bromberg, O. 2020b, arXiv e-prints, arXiv:2006.02466.

https://arxiv.org/abs/2006.02466

Gottlieb, O., Nakar, E., & Piran, T. 2018a, MNRAS, 473, 576, doi: 10.1093/mnras/stx2357

Gottlieb, O., Nakar, E., Piran, T., & Hotokezaka, K. 2018b, MNRAS, 479, 588, doi: 10.1093/mnras/sty1462

Gourgoulhon, E., Grandclément, P., Marck, J.-A., Novak, J., & Taniguchi, K. 2016, LORENE: Spectral methods differential equations solver. http://ascl.net/1608.018

Granot, J., Gill, R., Guetta, D., & De Colle, F. 2018, MNRAS, 481, 1597, doi: 10.1093/mnras/sty2308

Granot, J., Guetta, D., & Gill, R. 2017, ApJ, 850, L24, doi: 10.3847/2041-8213/aa991d

Granot, J., Panaitescu, A., Kumar, P., & Woosley, S. E. 2002, ApJ, 570, L61, doi: 10.1086/340991

Grossman, D., Korobkin, O., Rosswog, S., & Piran, T. 2014, MNRAS, 439, 757, doi: 10.1093/mnras/stt2503

GROWTH. 2017, GRB Coordinates Network, 21815

Grupe, D., Burrows, D. N., Patel, S. K., et al. 2006, ApJ, 653, 462, doi: 10.1086/508739

Guetta, D., & Piran, T. 2006, A&A, 453, 823, doi: 10.1051/0004-6361:20054498

Haggard, D., Nynka, M., Ruan, J. J., et al. 2017, ApJ, 848, L25, doi: 10.3847/2041-8213/aa8ede

Hamidani, H., & Ioka, K. 2020, arXiv e-prints, arXiv:2007.10690. https://arxiv.org/

abs/2007.10690

Hamidani, H., Kiuchi, K., & Ioka, K. 2020, MNRAS, 491, 3192, doi: 10.1093/mnras/stz3231

Harpaz, A. 1984, MNRAS, 210, 633, doi: 10.1093/mnras/210.3.633

Hawley, J. F., Guan, X., & Krolik, J. H. 2011, ApJ, 738, 84, doi: 10.1088/0004-637X/738/1/84

Hawley, J. F., Richers, S. A., Guan, X., & Krolik, J. H. 2013, ApJ, 772, 102, doi: 10.1088/0004-637X/772/2/102

Hotokezaka, K., Kiuchi, K., Kyutoku, K., et al. 2013, Phys. Rev. D, 87, 024001, doi: 10.1103/PhysRevD.87.024001

Houck, J. C., & Chevalier, R. A. 1991, ApJ, 376, 234, doi: 10.1086/170272

Hoyle, F., & Lyttleton, R. A. 1939, Proceedings of the Cambridge Philosophical Society, 35, 405, doi: 10.1017/S0305004100021150

Hulse, R. A., & Taylor, J. H. 1975, ApJ, 195, L51, doi: 10.1086/181708

Hunt, R. 1971, MNRAS, 154, 141, doi: 10.1093/mnras/154.2.141

Iben, Jr., I., & Livio, M. 1993, PASP, 105, 1373, doi: 10.1086/133321

Ivanova, N., Justham, S., Chen, X., et al. 2013, A&A Rev., 21, 59, doi: 10.1007/s00159-013-0059-2

Janiuk, A. 2014, A&A, 568, A105, doi: 10.1051/0004-6361/201423822

—. 2019, ApJ, 882, 163, doi: 10.3847/1538-4357/ab3349

Janiuk, A., Mioduszewski, P., & Moscibrodzka, M. 2013, ApJ, 776, 105, doi: 10.1088/0004-637X/776/2/105

Janiuk, A., Sukova, P., & Palit, I. 2018, ApJ, 868, 68, doi: 10.3847/1538-4357/aae83f

Just, O., Goriely, S., Janka, H.-T., Nagataki, S., & Bauswein, A. 2021, arXiv e-prints, arXiv:2102.08387. https://arxiv.org/abs/2102.08387

Just, O., Obergaulinger, M., & Janka, H. T. 2015, MNRAS, 453, 3386, doi: 10.1093/mnras/stv1892

Just, O., Obergaulinger, M., Janka, H.-T., Bauswein, A., & Schwarz, N. 2016, ApJ, 816, L30, doi: 10.3847/2041-8205/816/2/L30

Kalogera, V., Belczynski, K., Kim, C., O'Shaughnessy, R., & Willems, B. 2007, Phys. Rep., 442, 75, doi: 10.1016/j.physrep.2007.02.008

Kaneko, Y., Ramirez-Ruiz, E., Granot, J., et al. 2007, ApJ, 654, 385, doi: 10.1086/508324

Kasen, D., Badnell, N. R., & Barnes, J. 2013a, ApJ, 774, 25, doi: 10.1088/0004-637X/774/1/25

—. 2013b, ApJ, 774, 25, doi: 10.1088/0004-637X/774/1/25

Kasen, D., & Barnes, J. 2019, ApJ, 876, 128, doi: 10.3847/1538-4357/ab06c2

Kasen, D., Fernández, R., & Metzger, B. D. 2015a, MNRAS, 450, 1777, doi: 10.1093/mnras/stv721

—. 2015b, MNRAS, 450, 1777, doi: 10.1093/mnras/stv721

Kasen, D., Metzger, B., Barnes, J., Quataert, E., & Ramirez-Ruiz, E. 2017, Nature, 551, 80, doi: 10.1038/nature24453

Kasliwal, M. M., Kasen, D., Lau, R. M., et al. 2019, MNRAS, L14, doi: 10.1093/mnrasl/slz007

Kathirgamaraju, A., Barniol Duran, R., & Giannios, D. 2018, MNRAS, 473, L121, doi: 10.1093/mnrasl/slx175

Kathirgamaraju, A., Tchekhovskoy, A., Giannios, D., & Barniol Duran, R. 2019, MNRAS, 484, L98, doi: 10.1093/mnrasl/slz012

Kilpatrick, C. D., Foley, R. J., Kasen, D., et al. 2017, Science, 358, 1583, doi: 10.1126/science.aaq0073

Kissin, Y., & Thompson, C. 2015, ApJ, 808, 35, doi: 10.1088/0004-637X/808/1/35

Kiuchi, K., Cerdá-Durán, P., Kyutoku, K., Sekiguchi, Y., & Shibata, M. 2015a, Phys. Rev. D, 92, 124034, doi: 10.1103/PhysRevD.92.124034

Kiuchi, K., Kyutoku, K., Sekiguchi, Y., & Shibata, M. 2018, Phys. Rev. D, 97, 124039, doi: 10.1103/PhysRevD.97.124039

Kiuchi, K., Kyutoku, K., Sekiguchi, Y., Shibata, M., & Wada, T. 2014, Phys. Rev. D, 90, 041502, doi: 10.1103/PhysRevD.90.041502

Kiuchi, K., Sekiguchi, Y., Kyutoku, K., et al. 2015b, Phys. Rev. D, 92, 064034, doi: 10.1103/PhysRevD.92.064034

Kluźniak, W., & Lee, W. H. 1998, ApJ, 494, L53, doi: 10.1086/311151

Kochanek, C. S. 2015, MNRAS, 446, 1213, doi: 10.1093/mnras/stu2056

Kohri, K., & Mineshige, S. 2002, ApJ, 577, 311, doi: 10.1086/342166

Kohri, K., Narayan, R., & Piran, T. 2005, ApJ, 629, 341, doi: 10.1086/431354

Kouveliotou, C., Meegan, C. A., Fishman, G. J., et al. 1993, ApJ, 413, L101, doi: 10.1086/186969

Kruckow, M. U., Tauris, T. M., Langer, N., et al. 2016, A&A, 596, A58, doi: 10.1051/

0004-6361/201629420

Kulkarni, S. R. 2005, arXiv e-prints, astro. https://arxiv.org/abs/astro-ph/0510256

Kumar, P., & Zhang, B. 2015, Phys. Rep., 561, 1, doi: 10.1016/j.physrep.2014.09.008

Lamb, G. P., & Kobayashi, S. 2018, MNRAS, 478, 733, doi: 10.1093/mnras/sty1108

Lamb, G. P., Mandel, I., & Resmi, L. 2018, MNRAS, 481, 2581, doi: 10.1093/mnras/sty2196

Lamb, G. P., Lyman, J. D., Levan, A. J., et al. 2019, ApJ, 870, L15, doi: 10.3847/2041-8213/aaf96b

Lawrence, S., Tervala, J. G., Bedaque, P. F., & Miller, M. C. 2015, ApJ, 808, 186, doi: 10.1088/0004-637X/808/2/186

Lazzati, D., Ciolfi, R., & Perna, R. 2020, ApJ, 898, 59, doi: 10.3847/1538-4357/ab9a44

Lazzati, D., Deich, A., Morsony, B. J., & Workman, J. C. 2017, MNRAS, 471, 1652, doi: 10.1093/mnras/stx1683

Lazzati, D., Morsony, B. J., Blackwell, C. H., & Begelman, M. C. 2012, ApJ, 750, 68, doi: 10.1088/0004-637X/750/1/68

Lazzati, D., & Perna, R. 2019, arXiv e-prints. https://arxiv.org/abs/1904.08425

Lazzati, D., Perna, R., Morsony, B. J., et al. 2018, Physical Review Letters, 120, 241103, doi: 10.1103/PhysRevLett.120.241103

Lee, W. H., & Ramirez-Ruiz, E. 2006, ApJ, 641, 961, doi: 10.1086/500533

—. 2007a, New Journal of Physics, 9, 17, doi: 10.1088/1367-2630/9/1/017

—. 2007b, New Journal of Physics, 9, 17, doi: 10.1088/1367-2630/9/1/017

Lee, W. H., Ramirez-Ruiz, E., & Granot, J. 2005a, ApJ, 630, L165, doi: 10.1086/496882

Lee, W. H., Ramirez-Ruiz, E., & López-Cámara, D. 2009, ApJ, 699, L93, doi: 10.1088/0004-637X/699/2/L93

Lee, W. H., Ramirez-Ruiz, E., & Page, D. 2004, ApJ, 608, L5, doi: 10.1086/422217

—. 2005b, ApJ, 632, 421, doi: 10.1086/432373

Leventis, K., van Eerten, H. J., Meliani, Z., & Wijers, R. A. M. J. 2012, MNRAS, 427, 1329, doi: 10.1111/j.1365-2966.2012.21994.x

Li, L.-X., & Paczyński, B. 1998a, ApJ, 507, L59, doi: 10.1086/311680

—. 1998b, ApJ, 507, L59, doi: 10.1086/311680

Li, X., & Siegel, D. M. 2021, arXiv e-prints, arXiv:2103.02616. https://arxiv.org/abs/2103.02616

Lippuner, J., Fernández, R., Roberts, L. F., et al. 2017, MNRAS, 472, 904, doi: 10.1093/mnras/stx1987

Lippuner, J., & Roberts, L. F. 2015, ApJ, 815, 82, doi: 10.1088/0004-637X/815/2/82

Livio, M., Soker, N., de Kool, M., & Savonije, G. J. 1986a, MNRAS, 218, 593, doi: 10.1093/mnras/218.4.593

—. 1986b, MNRAS, 222, 235, doi: 10.1093/mnras/222.2.235

López-Cámara, D., Morsony, B. J., Begelman, M. C., & Lazzati, D. 2013, ApJ, 767, 19, doi: 10.1088/0004-637X/767/1/19

Lovegrove, E., & Woosley, S. E. 2013, ApJ, 769, 109, doi: 10.1088/0004-637X/769/2/109

Lyman, J. D., Lamb, G. P., Levan, A. J., et al. 2018, Nature Astronomy, 2, 751, doi: 10.1038/s41550-018-0511-3

MacLeod, M., Antoni, A., Murguia-Berthier, A., Macias, P., & Ramirez-Ruiz, E. 2017a, ApJ, 838, 56, doi: 10.3847/1538-4357/aa6117

MacLeod, M., Macias, P., Ramirez-Ruiz, E., et al. 2017b, ApJ, 835, 282, doi: 10.3847/1538-4357/835/2/282

MacLeod, M., & Ramirez-Ruiz, E. 2015a, ApJ, 803, 41, doi: 10.1088/0004-637X/803/1/41

—. 2015b, ApJ, 798, L19, doi: 10.1088/2041-8205/798/1/L19

Margalit, B., & Metzger, B. D. 2017, ApJ, 850, L19, doi: 10.3847/2041-8213/aa991c

Margutti, R., Alexander, K. D., Xie, X., et al. 2018, ApJ, 856, L18, doi: 10.3847/2041-8213/aab2ad

Martin, D., Perego, A., Arcones, A., et al. 2015, ApJ, 813, 2, doi: 10.1088/0004-637X/813/1/2

Matsumoto, J., & Masada, Y. 2019, MNRAS, 490, 4271, doi: 10.1093/mnras/stz2821

McKinney, J. C., Tchekhovskoy, A., & Blandford, R. D. 2012, MNRAS, 423, 3083, doi: 10.1111/j.1365-2966.2012.21074.x

McKinney, J. C., Tchekhovskoy, A., Sadowski, A., & Narayan, R. 2014, MNRAS, 441, 3177, doi: 10.1093/mnras/stu762

Meliani, Z., & Keppens, R. 2010, A&A, 520, L3, doi: 10.1051/0004-6361/201015423

Metzger, B. D. 2017, Living Reviews in Relativity, 20, 3, doi: 10.1007/s41114-017-0006-z

—. 2019, Living Reviews in Relativity, 23, 1, doi: 10.1007/s41114-019-0024-0

Metzger, B. D., Arcones, A., Quataert, E., & Martínez-Pinedo, G. 2010a, MNRAS, 402, 2771, doi: 10.1111/j.1365-2966.2009.16107.x

Metzger, B. D., & Fernández, R. 2014, MNRAS, 441, 3444, doi: 10.1093/mnras/stu802

Metzger, B. D., Piro, A. L., & Quataert, E. 2008a, MNRAS, 390, 781, doi: 10.1111/j.1365-2966.2008.13789.x

Metzger, B. D., Quataert, E., & Thompson, T. A. 2008b, MNRAS, 385, 1455, doi: 10.1111/j.1365-2966.2008.12923.x

Metzger, B. D., Thompson, T. A., & Quataert, E. 2018, ApJ, 856, 101, doi: 10.3847/1538-4357/aab095

Metzger, B. D., & Zivancev, C. 2016, MNRAS, 461, 4435, doi: 10.1093/mnras/stw1800

Metzger, B. D., Martínez-Pinedo, G., Darbha, S., et al. 2010b, MNRAS, 406, 2650, doi: 10.1111/j.1365-2966.2010.16864.x

Miller, J. M., Ryan, B. R., & Dolence, J. C. 2019a, ApJS, 241, 30, doi: 10.3847/1538-4365/ab09fc

Miller, J. M., Sprouse, T. M., Fryer, C. L., et al. 2020, ApJ, 902, 66, doi: 10.3847/1538-4357/abb4e3

Miller, J. M., Ryan, B. R., Dolence, J. C., et al. 2019b, Phys. Rev. D, 100, 023008, doi: 10.1103/PhysRevD.100.023008

Mizuno, Y., Lyubarsky, Y., Nishikawa, K.-I., & Hardee, P. E. 2012, ApJ, 757, 16, doi: 10.1088/0004-637X/757/1/16

Mochkovitch, R., Hernanz, M., Isern, J., & Martin, X. 1993, Nature, 361, 236, doi: 10.

1038/361236a0

Mooley, K. P., Deller, A. T., Gottlieb, O., et al. 2018a, Nature, 561, 355, doi: 10.1038/s41586-018-0486-3

Mooley, K. P., Frail, D. A., Dobie, D., et al. 2018b, ApJ, 868, L11, doi: 10.3847/2041-8213/aaeda7

Moreno Méndez, E., López-Cámara, D., & De Colle, F. 2017, ArXiv e-prints. https://arxiv.org/abs/1702.03293

Mösta, P., Radice, D., Haas, R., Schnetter, E., & Bernuzzi, S. 2020, arXiv e-prints, arXiv:2003.06043. https://arxiv.org/abs/2003.06043

Mukherjee, D., Bodo, G., Mignone, A., Rossi, P., & Vaidya, B. 2020, arXiv e-prints, arXiv:2009.10475. https://arxiv.org/abs/2009.10475

Murguia-Berthier, A., Batta, A., Janiuk, A., et al. 2020, ApJ, 901, L24, doi: 10.3847/2041-8213/abb818

Murguia-Berthier, A., MacLeod, M., Ramirez-Ruiz, E., Antoni, A., & Macias, P. 2017a, ApJ, 845, 173, doi: 10.3847/1538-4357/aa8140

Murguia-Berthier, A., Montes, G., Ramirez-Ruiz, E., De Colle, F., & Lee, W. H. 2014, ApJ, 788, L8, doi: 10.1088/2041-8205/788/1/L8

Murguia-Berthier, A., Ramirez-Ruiz, E., De Colle, F., et al. 2021, ApJ, 908, 152, doi: 10.3847/1538-4357/abd08e

Murguia-Berthier, A., Ramirez-Ruiz, E., Montes, G., et al. 2017b, ApJ, 835, L34, doi: 10.3847/2041-8213/aa5b9e

Murguia-Berthier, A., Ramirez-Ruiz, E., Kilpatrick, C. D., et al. 2017c, ApJ, 848, L34,

doi: 10.3847/2041-8213/aa91b3

Nagakura, H., Hotokezaka, K., Sekiguchi, Y., Shibata, M., & Ioka, K. 2014, ApJ, 784, L28, doi: 10.1088/2041-8205/784/2/L28

Nakar, E. 2007, Phys. Rep., 442, 166, doi: 10.1016/j.physrep.2007.02.005

—. 2019, arXiv e-prints, arXiv:1912.05659. https://arxiv.org/abs/1912.05659

Nakar, E., Gottlieb, O., Piran, T., Kasliwal, M. M., & Hallinan, G. 2018, ApJ, 867, 18, doi: 10.3847/1538-4357/aae205

Nakar, E., & Piran, T. 2020, arXiv e-prints, arXiv:2005.01754. https://arxiv.org/abs/2005.01754

Narayan, R., Paczynski, B., & Piran, T. 1992, ApJ, 395, L83, doi: 10.1086/186493

Narayan, R., Piran, T., & Kumar, P. 2001, ApJ, 557, 949, doi: 10.1086/322267

Nathanail, A., Gill, R., Porth, O., Fromm, C. M., & Rezzolla, L. 2020a, MNRAS, 495, 3780, doi: 10.1093/mnras/staa1454

—. 2020b, arXiv e-prints, arXiv:2009.09714. https://arxiv.org/abs/2009.09714

Nathanail, A., Porth, O., & Rezzolla, L. 2019, ApJ, 870, L20, doi: 10.3847/2041-8213/aaf73a

Nedora, V., Bernuzzi, S., Radice, D., et al. 2020, arXiv e-prints, arXiv:2008.04333. https://arxiv.org/abs/2008.04333

—. 2021, ApJ, 906, 98, doi: 10.3847/1538-4357/abc9be

Neilsen, D., Liebling, S. L., Anderson, M., et al. 2014, Phys. Rev. D, 89, 104029, doi: 10.1103/PhysRevD.89.104029

Nelemans, G., Verbunt, F., Yungelson, L. R., & Portegies Zwart, S. F. 2000, A&A, 360,

1011

Nicholl, M., Berger, E., Kasen, D., et al. 2017, ApJ, 848, L18, doi: 10.3847/2041-8213/aa9029

Noble, S. C., Gammie, C. F., McKinney, J. C., & Del Zanna, L. 2006a, ApJ, 641, 626, doi: 10.1086/500349

—. 2006b, ApJ, 641, 626, doi: 10.1086/500349

Noble, S. C., Krolik, J. H., & Hawley, J. F. 2009, ApJ, 692, 411, doi: 10.1088/0004-637X/692/1/411

—. 2010, ApJ, 711, 959, doi: 10.1088/0004-637X/711/2/959

Noble, S. C., Mundim, B. C., Nakano, H., et al. 2012, ApJ, 755, 51, doi: 10.1088/0004-637X/755/1/51

Norris, J. P., & Bonnell, J. T. 2006, ApJ, 643, 266, doi: 10.1086/502796

O'Connor, E., & Ott, C. D. 2010, Classical and Quantum Gravity, 27, 114103, doi: 10.1088/0264-9381/27/11/114103

Ostriker, E. C. 1999, ApJ, 513, 252, doi: 10.1086/306858

Paciesas, W. S., Meegan, C. A., Pendleton, G. N., et al. 1999, ApJS, 122, 465, doi: 10.1086/313224

Paczynski, B. 1976, in IAU Symposium, Vol. 73, Structure and Evolution of Close Binary Systems, ed. P. Eggleton, S. Mitton, & J. Whelan, 75

Paczynski, B. 1986, ApJ, 308, L43, doi: 10.1086/184740

—. 1991, Acta Astron., 41, 257

Paczyński, B., & Wiita, P. J. 1980, A&A, 88, 23

Palenzuela, C., Lehner, L., Ponce, M., et al. 2013, Phys. Rev. Lett., 111, 061105, doi: 10.1103/PhysRevLett.111.061105

Palenzuela, C., Liebling, S. L., Neilsen, D., et al. 2015, Phys. Rev. D, 92, 044045, doi: 10.1103/PhysRevD.92.044045

Palit, I., Janiuk, A., & Sukova, P. 2019, MNRAS, 487, 755, doi: 10.1093/mnras/stz1296

Palmer, D. M., Barthelmy, S., Gehrels, N., et al. 2005, Nature, 434, 1107, doi: 10.1038/nature03525

Pan, Y. C., Kilpatrick, C. D., Simon, J. D., et al. 2017, ApJ, 848, L30, doi: 10.3847/2041-8213/aa9116

Papish, O., Soker, N., & Bukay, I. 2013, ArXiv e-prints. https://arxiv.org/abs/1309.3925

Paxton, B., Bildsten, L., Dotter, A., et al. 2011, ApJS, 192, 3, doi: 10.1088/0067-0049/192/1/3

Paxton, B., Cantiello, M., Arras, P., et al. 2013, ApJS, 208, 4, doi: 10.1088/0067-0049/208/1/4

Paxton, B., Marchant, P., Schwab, J., et al. 2015, ApJS, 220, 15, doi: 10.1088/0067-0049/220/1/15

Perego, A., Rosswog, S., Cabezón, R. M., et al. 2014a, MNRAS, 443, 3134, doi: 10.1093/mnras/stu1352

—. 2014b, MNRAS, 443, 3134, doi: 10.1093/mnras/stu1352

Perna, R., Duffell, P., Cantiello, M., & MacFadyen, A. I. 2014, ApJ, 781, 119, doi: 10.

1088/0004-637X/781/2/119

Pian, E., D'Avanzo, P., Benetti, S., et al. 2017, Nature, 551, 67, doi: 10.1038/nature24298

Piran, T. 2004, Reviews of Modern Physics, 76, 1143, doi: 10.1103/RevModPhys.76.1143

Piro, A. L., Giacomazzo, B., & Perna, R. 2017, ApJ, 844, L19, doi: 10.3847/2041-8213/aa7f2f

Popham, R., Woosley, S. E., & Fryer, C. 1999, ApJ, 518, 356, doi: 10.1086/307259

Postnov, K. A., & Yungelson, L. R. 2014, Living Reviews in Relativity, 17, 3, doi: 10.12942/lrr-2014-3

Powell, M. J. 1968, A Fortran subroutine for solving systems of nonlinear algebraic equations, Tech. rep., United Kingdom Atomic Energy Authority

Press, W. H., Teukolsky, S. A., Vetterling, W. T., & Flannery, B. P. 1992, Numerical Recipes in C, 2nd edn. (Cambridge, USA: Cambridge University Press)

Price, D. J., & Rosswog, S. 2006, Science, 312, 719, doi: 10.1126/science.1125201

Qian, Q., Fendt, C., & Vourellis, C. 2018, ApJ, 859, 28, doi: 10.3847/1538-4357/aabd36

Quataert, E., Lecoanet, D., & Coughlin, E. R. 2019, MNRAS, 485, L83, doi: 10.1093/mnrasl/slz031

Radice, D., Bernuzzi, S., & Perego, A. 2020, Annual Review of Nuclear and Particle Science, 70, 95, doi: 10.1146/annurev-nucl-013120-114541

Radice, D., Galeazzi, F., Lippuner, J., et al. 2016, MNRAS, 460, 3255, doi: 10.1093/

mnras/stw1227

Radice, D., Perego, A., Hotokezaka, K., et al. 2018, ApJ, 869, 130, doi: 10.3847/1538-4357/aaf054

Ramírez-Agudelo, O. H., Simón-Díaz, S., Sana, H., et al. 2013, A&A, 560, A29, doi: 10.1051/0004-6361/201321986

Ramirez-Ruiz, E., Andrews, J. J., & Schrøder, S. L. 2019, ApJ, 883, L6, doi: 10.3847/2041-8213/ab3f2c

Ramirez-Ruiz, E., Celotti, A., & Rees, M. J. 2002, MNRAS, 337, 1349, doi: 10.1046/j.1365-8711.2002.05995.x

Ramirez-Ruiz, E., Granot, J., Kouveliotou, C., et al. 2005, ApJ, 625, L91, doi: 10.1086/431237

Ravi, V., & Lasky, P. D. 2014, MNRAS, 441, 2433, doi: 10.1093/mnras/stu720

Rees, M. J., & Meszaros, P. 1992, MNRAS, 258, 41P, doi: 10.1093/mnras/258.1.41P

Rezzolla, L., Giacomazzo, B., Baiotti, L., et al. 2011, ApJ, 732, L6, doi: 10.1088/2041-8205/732/1/L6

Rezzolla, L., & Kumar, P. 2015, ApJ, 802, 95, doi: 10.1088/0004-637X/802/2/95

Rezzolla, L., & Takami, K. 2016, Phys. Rev. D, 93, 124051, doi: 10.1103/PhysRevD.93.124051

Roberts, L. F., Kasen, D., Lee, W. H., & Ramirez-Ruiz, E. 2011a, ApJ, 736, L21, doi: 10.1088/2041-8205/736/1/L21

—. 2011b, ApJ, 736, L21, doi: 10.1088/2041-8205/736/1/L21

Roberts, L. F., Lippuner, J., Duez, M. D., et al. 2017, MNRAS, 464, 3907, doi: 10.

1093/mnras/stw2622

Rossi, P., Mignone, A., Bodo, G., Massaglia, S., & Ferrari, A. 2008, A&A, 488, 795, doi: 10.1051/0004-6361:200809687

Rosswog, S. 2005, ApJ, 634, 1202, doi: 10.1086/497062

Rosswog, S., Feindt, U., Korobkin, O., et al. 2017, Classical and Quantum Gravity, 34, 104001, doi: 10.1088/1361-6382/aa68a9

Rosswog, S., & Liebendörfer, M. 2003, MNRAS, 342, 673, doi: 10.1046/j.1365-8711.2003.06579.x

Rosswog, S., Liebendörfer, M., Thielemann, F. K., et al. 1999, A&A, 341, 499. https://arxiv.org/abs/astro-ph/9811367

Rosswog, S., & Ramirez-Ruiz, E. 2002, MNRAS, 336, L7, doi: 10.1046/j.1365-8711.2002.05898.x

—. 2003, MNRAS, 343, L36, doi: 10.1046/j.1365-8711.2003.06889.x

Rosswog, S., Ramirez-Ruiz, E., & Davies, M. B. 2003, MNRAS, 345, 1077, doi: 10.1046/j.1365-2966.2003.07032.x

Ruffert, M. 1994a, ApJ, 427, 342, doi: 10.1086/174144

—. 1994b, A&AS, 106

—. 1995, A&AS, 113, 133

—. 1996, A&A, 311, 817

—. 1997, A&A, 317, 793

—. 1999, A&A, 346, 861

Ruffert, M., & Arnett, D. 1994, ApJ, 427, 351, doi: 10.1086/174145

Ruffert, M., Janka, H. T., & Schaefer, G. 1996, A&A, 311, 532. https://arxiv.org/abs/astro-ph/9509006

Ruiz, M., Lang, R. N., Paschalidis, V., & Shapiro, S. L. 2016, ApJ, 824, L6, doi: 10.3847/2041-8205/824/1/L6

Ruiz, M., Shapiro, S. L., & Tsokaros, A. 2018, Phys. Rev. D, 97, 021501, doi: 10.1103/PhysRevD.97.021501

Ruiz, M., Tsokaros, A., Paschalidis, V., & Shapiro, S. L. 2019, Phys. Rev. D, 99, 084032, doi: 10.1103/PhysRevD.99.084032

Ryan, G., van Eerten, H., Piro, L., & Troja, E. 2020, ApJ, 896, 166, doi: 10.3847/1538-4357/ab93cf

Salafia, O. S., Barbieri, C., Ascenzi, S., & Toffano, M. 2020, A&A, 636, A105, doi: 10.1051/0004-6361/201936335

Salafia, O. S., Ghirlanda, G., Ascenzi, S., & Ghisellini, G. 2019, A&A, 628, A18, doi: 10.1051/0004-6361/201935831

Sana, H., de Mink, S. E., de Koter, A., et al. 2012, Science, 337, 444, doi: 10.1126/science.1223344

Sano, T., Inutsuka, S.-i., Turner, N. J., & Stone, J. M. 2004, ApJ, 605, 321, doi: 10.1086/382184

Savchenko, V., Ferrigno, C., Kuulkers, E., et al. 2017, ApJ, 848, L15, doi: 10.3847/2041-8213/aa8f94

Sądowski, A., Narayan, R., Tchekhovskoy, A., et al. 2015, MNRAS, 447, 49, doi: 10.1093/mnras/stu2387

Schrøder, S. L., MacLeod, M., Loeb, A., Vigna-Gómez, A., & Mandel, I. 2020, ApJ, 892, 13, doi: 10.3847/1538-4357/ab7014

Sekiguchi, Y., Kiuchi, K., Kyutoku, K., Shibata, M., & Taniguchi, K. 2016, Phys. Rev. D, 93, 124046, doi: 10.1103/PhysRevD.93.124046

Shapiro, S. L. 2000, ApJ, 544, 397, doi: 10.1086/317209

Shapiro, S. L., & Teukolsky, S. A. 1986, Black Holes, White Dwarfs and Neutron Stars: The Physics of Compact Objects

Shappee, B. J., Simon, J. D., Drout, M. R., et al. 2017, Science, 358, 1574, doi: 10.1126/science.aaq0186

Shen, S., Cooke, R. J., Ramirez-Ruiz, E., et al. 2015, ApJ, 807, 115, doi: 10.1088/0004-637X/807/2/115

Shibata, M., Kiuchi, K., & Sekiguchi, Y.-i. 2017, Phys. Rev. D, 95, 083005, doi: 10.1103/PhysRevD.95.083005

Shibata, M., & Taniguchi, K. 2006, Phys. Rev. D, 73, 064027, doi: 10.1103/PhysRevD.73.064027

Shiber, S., Kashi, A., & Soker, N. 2017, MNRAS, 465, L54, doi: 10.1093/mnrasl/slw208

Shima, E., Matsuda, T., Takeda, H., & Sawada, K. 1985, MNRAS, 217, 367, doi: 10.1093/mnras/217.2.367

Siebert, M. R., Foley, R. J., Drout, M. R., et al. 2017, ApJ, 848, L26, doi: 10.3847/2041-8213/aa905e

Siegel, D. M. 2019, European Physical Journal A, 55, 203, doi: 10.1140/epja/

i2019-12888-9

Siegel, D. M., Barnes, J., & Metzger, B. D. 2019, Nature, 569, 241, doi: 10.1038/s41586-019-1136-0

Siegel, D. M., Ciolfi, R., Harte, A. I., & Rezzolla, L. 2013, Phys. Rev. D, 87, 121302, doi: 10.1103/PhysRevD.87.121302

Siegel, D. M., Ciolfi, R., & Rezzolla, L. 2014a, ApJ, 785, L6, doi: 10.1088/2041-8205/785/1/L6

—. 2014b, ApJ, 785, L6, doi: 10.1088/2041-8205/785/1/L6

Siegel, D. M., & Metzger, B. D. 2017, Phys. Rev. Lett., 119, 231102, doi: 10.1103/PhysRevLett.119.231102

—. 2018, ApJ, 858, 52, doi: 10.3847/1538-4357/aabaec

Siegel, D. M., Mösta, P., Desai, D., & Wu, S. 2018, ApJ, 859, 71, doi: 10.3847/1538-4357/aabcc5

Smartt, S. J. 2015, PASA, 32, e016, doi: 10.1017/pasa.2015.17

Smartt, S. J., Chen, T. W., Jerkstrand, A., et al. 2017, Nature, 551, 75, doi: 10.1038/nature24303

Soares-Santos, M., Holz, D. E., Annis, J., et al. 2017, ApJ, 848, L16, doi: 10.3847/2041-8213/aa9059

Soker, N. 2004, New A, 9, 399, doi: 10.1016/j.newast.2004.01.004

—. 2015, ApJ, 800, 114, doi: 10.1088/0004-637X/800/2/114

Soker, N., Livio, M., de Kool, M., & Savonije, G. J. 1986, MNRAS, 221, 445, doi: 10.1093/mnras/221.2.445

Sorathia, K. A., Reynolds, C. S., Stone, J. M., & Beckwith, K. 2012, ApJ, 749, 189, doi: 10.1088/0004-637X/749/2/189

Staff, J. E., De Marco, O., Macdonald, D., et al. 2016, MNRAS, 455, 3511, doi: 10.1093/mnras/stv2548

Sukhbold, T., Ertl, T., Woosley, S. E., Brown, J. M., & Janka, H. T. 2016, ApJ, 821, 38, doi: 10.3847/0004-637X/821/1/38

Suková, P., Charzyński, S., & Janiuk, A. 2017, MNRAS, 472, 4327, doi: 10.1093/mnras/stx2254

Suková, P., & Janiuk, A. 2015, MNRAS, 447, 1565, doi: 10.1093/mnras/stu2544

Taam, R. E., & Fryxell, B. A. 1989, ApJ, 339, 297, doi: 10.1086/167297

Taam, R. E., & Ricker, P. M. 2010, New A Rev., 54, 65, doi: 10.1016/j.newar.2010.09.027

Taam, R. E., & Sandquist, E. L. 2000, ARA&A, 38, 113, doi: 10.1146/annurev.astro.38.1.113

Tanaka, M., & Hotokezaka, K. 2013, ApJ, 775, 113, doi: 10.1088/0004-637X/775/2/113

Tanvir, N. R., Levan, A. J., González-Fernández, C., et al. 2017, ApJ, 848, L27, doi: 10.3847/2041-8213/aa90b6

Tchekhovskoy, A., & Bromberg, O. 2016, MNRAS, 461, L46, doi: 10.1093/mnrasl/slw064

Tchekhovskoy, A., Narayan, R., & McKinney, J. C. 2011, MNRAS, 418, L79, doi: 10.1111/j.1745-3933.2011.01147.x

Troja, E., Sakamoto, T., Cenko, S. B., et al. 2016, ApJ, 827, 102, doi: 10.3847/0004-637X/827/2/102

Troja, E., Piro, L., Ryan, G., et al. 2018, MNRAS, 478, L18, doi: 10.1093/mnrasl/sly061

Tsutsui, R., Yonetoku, D., Nakamura, T., Takahashi, K., & Morihara, Y. 2013, MNRAS, 431, 1398, doi: 10.1093/mnras/stt262

Ugliano, M., Janka, H., Arcones, A., & Marek, A. 2012, Astronomical Society of the Pacific Conference Series, Vol. 453, Explosion and Remnant Systematics of Neutrino-driven Supernovae for Spherically Symmetric Models, ed. R. Capuzzo-Dolcetta, M. Limongi, & A. Tornambè, 91

Urrutia, G., De Colle, F., Murguia-Berthier, A., & Ramirez-Ruiz, E. 2020, arXiv e-prints, arXiv:2011.06729. https://arxiv.org/abs/2011.06729

van Eerten, E. T. H., Ryan, G., Ricci, R., et al. 2018, arXiv e-prints. https://arxiv.org/abs/1808.06617

van Eerten, H. J., & MacFadyen, A. I. 2011, ApJ, 733, L37, doi: 10.1088/2041-8205/733/2/L37

van Putten, M. H. P. M., Della Valle, M., & Levinson, A. 2019, ApJ, 876, L2, doi: 10.3847/2041-8213/ab18a2

Villar, V. A., Guillochon, J., Berger, E., et al. 2017, ApJ, 851, L21, doi: 10.3847/2041-8213/aa9c84

Villata, M. 1992, MNRAS, 257, 450, doi: 10.1093/mnras/257.3.450

Voss, R., & Tauris, T. M. 2003, MNRAS, 342, 1169, doi: 10.1046/j.1365-8711.2003.

06616.x

Webbink, R. F. 1984, ApJ, 277, 355, doi: 10.1086/161701

Weidner, C., & Vink, J. S. 2010, A&A, 524, A98, doi: 10.1051/0004-6361/201014491

Woosley, S. E. 1993, ApJ, 405, 273, doi: 10.1086/172359

—. 2017, ApJ, 836, 244, doi: 10.3847/1538-4357/836/2/244

Woosley, S. E., & Bloom, J. S. 2006, ARA&A, 44, 507, doi: 10.1146/annurev.astro.43.072103.150558

Woosley, S. E., & Heger, A. 2006, ApJ, 637, 914, doi: 10.1086/498500

Wu, Y., & MacFadyen, A. 2018, ApJ, 869, 55, doi: 10.3847/1538-4357/aae9de

Xie, X., Zrake, J., & MacFadyen, A. 2018, ApJ, 863, 58, doi: 10.3847/1538-4357/aacf9c

Yuan, F., & Narayan, R. 2014, ARA&A, 52, 529, doi: 10.1146/annurev-astro-082812-141003

Zalamea, I., & Beloborodov, A. M. 2009, MNRAS, 398, 2005, doi: 10.1111/j.1365-2966.2009.15233.x

—. 2011, MNRAS, 410, 2302, doi: 10.1111/j.1365-2966.2010.17600.x

Zenati, Y., Perets, H. B., & Toonen, S. 2019, MNRAS, 486, 1805, doi: 10.1093/mnras/stz316

Zhang, B., & Mészáros, P. 2001, ApJ, 552, L35, doi: 10.1086/320255

Zilhão, M., & Noble, S. C. 2014, Classical and Quantum Gravity, 31, 065013, doi: 10.1088/0264-9381/31/6/065013